Tailoring the charge transport properties of small molecules and organic semiconductors

Dissertation

zur Erlangung des Grades

Doktor der Naturwissenschaften (Dr. rer. nat.)

am Fachbereich Physik, Mathematik und Informatik

der Johannes Gutenberg-Universität Mainz

von:

Deepthi Kamath Karnad

geboren in Mangalore (Indien)

Mainz, 2021

Deepthi Kamath Karnad

Tailoring the charge transport properties of small molecules and organic semiconductors

1. Berichterstatter: Prof. Dr. Paul W M Blom

2. Berichterstatter: Prof. Dr. Mathias Kläui

Datum der mündlichen Prüfung:

Max Planck Institute for Polymer Research

AK Blom
Ackermannweg 10
55128 Mainz

Acknowledgements

Firstly, I would like to express my deepest gratitude to my supervisor Prof. Dr. Paul Blom, who provided me with support and guidance and provided the opportunity to join his group. Thank you for your patience, understanding and encouragement to think beyond the boundaries. A special thanks to Dr. Gert-Jan Wetzelaer who has been a constant support through the time in EXTMOS and during my PhD. I would also like to acknowledge funding from the European Union Horizon 2020 Research and Innovation Programme under grant agreement No 646176.

A significant reason for my venturing into the field of organic electronics and technology is Prof. Dr. Marc Heyns (imec, Leuven) who provided the initial enthusiasm, encouragement, and excitement to enter this wonderful area and for which I will forever be grateful. A big thanks to Late Prof. V. Venkataraman (Indian Institute of Science, Bangalore) for his support and guidance, and for being a motivating figure for successfully transitioning from electronics engineering to physics, to enjoy the best of both worlds. I am thankful to Dr. Anne Karen Meyer (IFW - Dresden) for hosting me and training me, being my first entry into the German research environment.

Importantly, much of this work and training (PhD and beyond) would not have been possible if not for the encouraging mentorship and support provided in my initial days in Mainz by Dr. Thomas Lenz and Dr. Dong Zhao. I am very grateful to both of you for your support and friendship, which were crucial for my PhD work. A big thanks to Prof. Dr. Dago de Leeuw as well, who provided guidance, support and was a great sounding board for scientific discussions. I am grateful also to everyone else in the AK Blom: Ann-Kathrin Schönbein, Dr. Alexander Kunz, Dr. Irina Rörich, Dr. Quan Niu, Dr. Kai Philipps and Yeseul Park for all the help, support and company. It was great learning and working with all of you .

Special thanks to Ms. Verona Maus, Mrs. Michelle Beuchel, Mr. Frank Keller, Mr. Christian Bauer, Mr. Hans-Jürgen Guttmann who provided excellent administrative and technical support and provided an organized and efficient working environment. I am also grateful to Mrs. Petra Pausch for all the support, help and the fantastic barbeque party during the PhD and for always being available to answer all the organizational questions. A special thank you to Eleni Kapnisti for providing encouragement, support and being a wonderful German language teacher.

Many thanks are owed to God for His guidance and what strength and wisdom He has given me. Most importantly, thank you MDK and VDK for the unwavering faith, support, and love through the PhD. Finally, I'd like to thank my husband, GK for his love, support and encouragement and being there when I needed him. I am grateful for your company and look forward to the journey ahead.

Abstract

Organic electronics has emerged as a promising technology in the last decades offering opportunity to create a new form of electronics, which do not purely compete with inorganic electronics but complement it. Applications and products associated with it are primarily those that cannot be achieved with inorganic semiconductor technologies, due to material restrictions or costs associated with commercial production. While applications such as organic light-emitting diodes, organic solar cells and organic transistors have been commercialized, the charge transport in all of them are based on π-conjugated semiconducting molecular or polymeric materials that have charge carrier mobilities orders of magnitude lower than in inorganic semiconductors. While studies have been performed to improve the charge transport by using the concept of doping in equivalence to inorganic semiconductors, the success has been limited due to the high dependence on processing conditions.

Therefore, in the course of this work a selected system of investigations are undertaken to gather deeper insight into the phenomenon associated with processing of organic semiconductors and its effect on charge transport and device performance.

In the first part of this work the study of charge transport in the amorphous organic small molecules α-NPD (N,N-di(1-naphthyl)-N,N-diphenyl-(1,1-biphenyl)-4,4-diamine) and SpiroTAD (2,2,7,7-tetrakis(N,N-diphenylamino)-9,9-spirobifluorene)) is performed. Charge transport is investigated in solution-processed films and compared to charge transport in vacuum-deposited films of the same molecule. By optimizing the deposition conditions, such as solvent and concentration, equal charge-transport parameters for solution-processed and thermally-deposited films are demonstrated. The charge carrier transport characteristics are then modelled by drift-diffusion simulations. The dependence of the charge carrier mobility on temperature, carrier density and electric field was found to be the same for vacuum deposition and solution processing, demonstrating that solution processing can be a viable alternative to thermal evaporation in terms of charge transport.

In the second part, the charge transport in p-type doped films of α-NPD, doped with the high electron affinity dopant F6TCNNQ, is investigated. The results of the space-charge-limited current measurements for different doping concentrations reveal that only a small percentage of free charge carriers is generated with respect to the doping concentration, which is corroborated by impedance measurements. It is observed that at higher electric fields, more mobile charges are generated, which is interpreted as the dissociation of Coulombically

bound charge transfer states. Therefore, this demonstrates that while charge transfer may be efficient, free charge-carrier generation is severely limited by the Coulombic attraction of the countercharge on the dopant.

In the third part, the charge transport in solution-processed Spiro-OMeTAD layers is investigated and the doping efficiency of two p-type dopants, F4TCNQ and F6TCNNQ, at low to moderate doping concentration in a diode device configuration is analyzed. It is found that the addition of dopants drastically improves the conductivity of Spiro-OMeTAD. By numerical modelling of the current density-voltage characteristics, it is found that the doping efficiency at low electric fields is above 1%, which is considerably higher than the doping efficiency of evaporated Spiro-TAD:F6TCNNQ reference films. In addition, the doping efficiency is observed to increase with increasing electric fields, possibly originated from field-assisted ionization of the dopants.

Finally, difluorobenzothiadiazole-oligothiophene copolymer (PffBT4T-2DT) is solution processed into a well-ordered monolayer and is used to demonstrate an integrated circuit of hundreds of polymer monolayer field-effect transistors (PoM-FETs). Field-effect mobility of up to 3 $cm^2\ V^{-1}\ s^{-1}$ is achieved due to the pronounced organization of polymer chains, which greatly facilitate the charge carrier transport within the monolayer. Making use of the improved FET fabrication process, high molecular order and contact engineering, we are not only able to achieve high mobility but also large current modulation and high reproducibility of PffBT4T-2DT PoM-FETs. This reproducibility allows for combing the PoM-FETs into inverters to form unipolar gates, and the small parameter spread allows for the construction of ring oscillators from the individual inverters. In the next step, we successfully fabricate a state-of-the-art example of an organic integrated circuit by constructing a 15-bit code generator and thus demonstrating the potential of using bottom-up organic electronics.

Thereby, the results and findings from this work are able to provide a deeper insight and valuable answers into underlying physics and material processing effects on the charge transport characteristics in solution-processed organic semiconductors while demonstrating potential to integrate into commercial applications.

Zusammenfassung

Die organische Elektronik hat sich in den letzten Jahrzehnten zu einer vielversprechenden Technologie entwickelt, die die Möglichkeit bietet, eine neue Form der Elektronik zu schaffen, die nicht nur mit der anorganischen Elektronik konkurriert, sondern diese ergänzt. Die damit verbundenen Anwendungen und Produkte sind in erster Linie solche, die mit anorganischen Halbleitertechnologien aufgrund von Materialbeschränkungen oder der mit der kommerziellen Produktion verbundenen Kosten nicht erreicht werden können. Zwar wurden Anwendungen wie organische Leuchtdioden, organische Solarzellen und organische Transistoren auf den Markt gebracht, doch basiert der Ladungstransport in allen diesen Anwendungen auf π-konjugierten molekularen oder polymeren Halbleitermaterialien, deren Ladungsträgermobilität um Größenordnungen geringer ist als bei anorganischen Halbleitern. Es wurden zwar Studien durchgeführt, um die Mobilität durch das Konzept der Dotierung in Äquivalenz zu anorganischen Halbleitern zu verbessern, der Erfolg war jedoch aufgrund der starken Abhängigkeit von den Verarbeitungsbedingungen begrenzt. Daher wird im Rahmen dieser Arbeit ein ausgewähltes System von Untersuchungen durchgeführt, um einen tieferen Einblick in die mit der Verarbeitung organischer Halbleiter verbundenen Phänomene und deren Auswirkungen auf den Ladungstransport und die Leistung der Bauelemente zu gewinnen.

Im ersten Teil dieser Arbeit wird die Untersuchung des Ladungstransports in den amorphen organischen kleinen Molekülen α-NPD (N,N-Di(1-naphthyl)-N,N-diphenyl-(1,1-biphenyl)-4,4-diamin) und SpiroTAD (2,2,7,7-Tetrakis(N,N-diphenylamino)-9,9-spirobifluoren) durchgeführt. Der Ladungstransport wird in lösungsgefertigten Filmen untersucht und mit dem Ladungstransport in vakuumabgeschiedenen Filmen desselben Moleküls verglichen. Durch Optimierung der Abscheidungsbedingungen, wie Lösungsmittel und Konzentration, werden gleiche Ladungstransportparameter für in Lösung hergestellte und thermisch abgeschiedene Filme nachgewiesen. Die Ladungsträgertransporteigenschaften werden dann durch Drift-Diffusionssimulationen modelliert. Die Abhängigkeit der Ladungsträgermobilität von der Temperatur, der Ladungsträgerdichte und dem elektrischen Feld ist bei der Vakuumabscheidung und der Lösungsabscheidung gleich, was zeigt, dass die Lösungsabscheidung im Hinblick auf den Ladungstransport eine brauchbare Alternative zur thermischen Verdampfung sein kann. Im zweiten Teil wird der Ladungstransport in p-dotierten Schichten aus α-NPD untersucht, die mit dem hoch elektronenaffinen Dotierstoff F6TCNNQ dotiert sind. Die Ergebnisse der raumladungsbegrenzten Strommessungen für verschiedene Dotierungskonzentrationen zeigen, dass nur ein geringer Prozentsatz an freien

Ladungsträgern in Abhängigkeit von der Dotierungskonzentration erzeugt wird, was durch Impedanzmessungen bestätigt wird. Es wird beobachtet, dass bei höheren elektrischen Feldern mehr mobile Ladungen erzeugt werden, was als Dissoziation von coulombisch gebundenen Ladungstransferzuständen interpretiert wird. Dies zeigt, dass der Ladungstransfer zwar effizient sein kann, die Erzeugung freier Ladungsträger jedoch durch die coulombische Anziehung der Gegenladung auf den Dotierstoff stark eingeschränkt wird. Im dritten Teil wird der Ladungstransport in lösungsgefertigten Spiro-OMeTAD-Schichten untersucht und die Dotierungseffizienz der beiden p-Typ-Dotierstoffe F4TCNQ und F6TCNNQ bei niedriger bis mittlerer Dotierungskonzentration in einer Diodenkonfiguration analysiert. Es wird festgestellt, dass die Zugabe von Dotierstoffen die Leitfähigkeit von Spiro-OMeTAD drastisch verbessert. Durch numerische Modellierung der Stromdichte-Spannungs-Charakteristik wird festgestellt, dass die Dotiereffizienz bei niedrigen elektrischen Feldern über 1 % liegt, was wesentlich höher ist als die Dotiereffizienz von aufgedampften Spiro-TAD:F6TCNNQ-Referenzfilmen. Darüber hinaus wird beobachtet, dass die Dotierungseffizienz mit zunehmenden elektrischen Feldern steigt, was möglicherweise auf die feldunterstützte Ionisierung der Dotierstoffe zurückzuführen ist.

Zum Schluss wird das Difluorbenzothiadiazol-Oligothiophen-Copolymer (PffBT4T-2DT) in Lösung zu einer gut geordneten Monoschicht verarbeitet und zur Demonstration einer integrierten Schaltung mit Hunderten von Polymer-Monoschicht-Feldeffekttransistoren (PoM-FETs) verwendet. Aufgrund der ausgeprägten Organisation der Polymerketten, die den Ladungsträgertransport innerhalb der Monolage erheblich erleichtern, wird eine Feldeffektmobilität von bis zu 3 cm^2 V^{-1} s^{-1} erreicht. Durch den verbesserten FET-Herstellungsprozess, die hohe molekulare Ordnung und das Kontakt-Engineering sind wir in der Lage, nicht nur eine hohe Mobilität, sondern auch eine große Strommodulation und eine hohe Reproduzierbarkeit von PffBT4T-2DT PoM-FETs zu erreichen. Diese Reproduzierbarkeit ermöglicht es, die PoM-FETs zu Invertern zu kombinieren, um unipolare Gates zu bilden, und die geringe Parameterstreuung ermöglicht den Aufbau von Ringoszillatoren aus den einzelnen Invertern. Im nächsten Schritt gelingt es uns, ein modernes Beispiel für einen organischen integrierten Schaltkreis herzustellen, indem wir einen 15-Bit-Codegenerator konstruieren und damit das Potenzial der organischen Bottom-up-Elektronik demonstrieren.

Die Ergebnisse und Erkenntnisse aus dieser Arbeit können einen tieferen Einblick in die zugrundeliegende Physik und die Auswirkungen der Materialverarbeitung auf die Ladungscharakteristiken in lösungsprozessierten organischen Halbleitern geben und gleichzeitig das Potenzial zur Integration in kommerzielle Anwendungen aufzeigen.

Contents

Contents xi
List of Figures xv
List of Tables xix
Nomenclature xxi
Chapter 1 Introduction 1
References 5
Chapter 2 Theoretical fundamentals 7
2.1 Organic semiconductors 7
2.2 Linear combination of atomic orbitals 8
2.3 Organic light emitting diodes 12
2.4 Organic field-effect transistors 13
2.5 Charge-transport models for organic semiconductors 15
2.6 Device characteristics 21
2.7 Doping in organic semiconductors 22
2.8 Mechanisms of doping 22
2.8.1 Ion Pair formation 26
2.8.2 Charge transfer complex formation 27
2.9 Conclusion 28
References 29
Chapter 3 Experimental techniques 35
3.1 Materials and properties 35
3.2 Thin film processing 37
3.2.1 Thermal evaporation 38
3.2.2 Spin coating 38
3.2.3 Wire-bar (Mayer rod) coating 39

3.2.4 Drop-casting....40
3.2.5 Dip coating....41
3.3 Sample preparation....42
3.4 Device working principle....43
3.5 Device characterization....44
3.6 Atomic force microscopy....47
References....49
Chapter 4 Charge transport in undoped small molecules....51
4.1 Introduction....51
4.2 Sample fabrication and characterization....53
4.3 Results and Discussion....54
4.4 Conclusion....62
References....63
Chapter 5 Charge transport in organic semiconductor films of α-NPD doped with the high electron affinity dopant F6TCNNQ....65
5.1 Introduction....65
5.2 Sample fabrication and characterization....66
5.3 Results and Discussion....67
5.3.1 Current-Voltage characteristics of hole-only oevices of α-NPD doped with F6TCNNQ....67
5.3.2 Impedance spectroscopy on Schottky diodes of doped α-NPD layers....71
5.4 Conclusion....76
References....78
Chapter 6 Efficient doping of solution processed Spiro-OMeTAD....81
6.1 Introduction....81
6.2 Sample fabrication and characterization....83
6.3 Results and Discussion....85
6.4 Conclusion....93
References....94
Chapter 7 Conjugated polymer based integrated circuits....97
7.1 Introduction....97
7.2 Sample fabrication and characterization....100
7.3 Results and Discussion....101

7.4 Conclusion 109
References 111
Chapter 8 Conclusion and Outlook 113
8.1 Summary 113
8.2 Outlook 116
References 118
Appendix A 119
A.1 Calculation of depletion width: 119
A.2 UV-Vis Spectroscopy 121
A.3 FTIR spectra 124
A.4 Effect of barrier on numerical simulation of J-V Characteristics 127
Appendix B 129

List of Figures

Figure 2-1 Chemical structures of a) poly(p-phenylene vinylene) (PPV) b) α-NPD 7

Figure 2-2 a) sp^2 hybridization of carbon atoms. b) highest occupied molecular orbital (HOMO) and lowest unoccupied molecular orbital (LUMO) level formation due to hybridization c) Molecular bonding in benzene d) Energy levels in benzene by the Hückel Method with degenerate HOMO and LUMO states. 9

Figure 2-3 Schematic of a multilayer OLED structure 12

Figure 2-4 Operation regimes for an OFET and typical I-V characteristics.....14

Figure 2-5 Dependence of the mobility on charge-carrier density at vanishing electric field for different values of the dimensionless disorder parameter (σkBT) for different temperatures in units of $\mu 0$. Solid lines are the fits using the parametrization scheme in Eq. 2.18. Symbols are the numerical results. Reproduced with permission from [28].....20

Figure 2-6 Shift of the Fermi level for a p-doped organic semiconductor. With increasing dopant concentration, the Fermi level moves towards the HOMO level.....24

Figure 2-7 The schematic representation of the energy levels and the density of states due to p-type doping in both mechanisms of charge transfer complex (left) and ion pair formation (right) respectively. Reproduced with permission from [47].....27

Figure 3-1 Chemical structures of a) F4TCNQ a p-type dopant b) F6TCNNQ a p-type dopant c) α-NPD a hole transporting small molecule d) Spiro-TAD a hole transporting small molecule e) Spiro-OMeTAD solution processable hole transporting material 36

Figure 3-2 Energy level diagram of the materials used in this work.....37

Figure 3-3 Schematic of a thermal evaporator used for vacuum deposition of small molecule based thin films.....38

Figure 3-4: Schematic of spin-coating process.....39

Figure 3-5 Schematic of the wire bar coating process to create thin films.....41

Figure 3-6: Schematic of drop casting of solution processable materials to create thin films on substrates.....41

Figure 3-7 Dip coating steps used in thin film processing.....42

Figure 3-8 Schematic overview of the three dominant processes during OLED operation: 1) injection, 2) transport and 3) recombination.....44

Figure 3-9: Schematic energy diagram of a single charge carrier device: a) electron only device with two low work function electrodes and b) hole only device with two high work function electrodes 44

Figure 3-10 Hole current measurement of a Spiro-TAD hole only device 46

Figure 3-11 Schematic of a typical hole only structure used to measure single carrier charge transport in this work 46

Figure 3-12 Charge transport measurements of a single-layer OLEDs with Spiro-TAD (300 nm). Solid lines show the J-V characteristics and dotted lines show the photocurrent density. 47

Figure 3-13 Schematic representation of an AFM (Thorlabs) 48

Figure 4-1: Experimental current density-voltage characteristics of hole-only devices with a Spiro-TAD layer thickness of 100 nm. The solution-processed films spin-cast from chlorobenzene (red triangles), toluene (green squares), or chloroform (blue diamonds) are compared to a thermally evaporated (black circles) reference device. 54

Figure 4-2: Experimental current density-voltage characteristics of hole-only devices with an α-NPD layer with a thickness of 100 nm. Thermally evaporated devices (black squares) are compared to solution-cast films from different solvents: chloroform (green triangles) and chlorobenzene (red dots). 55

Figure 4-3: Temperature-dependent experimental (symbols) and simulated (lines) current density voltage characteristics of Spiro-TAD hole-only devices with a layer thickness of 180 nm, solution-processed from toluene (a) and vacuum-deposited (b). 56

Figure 4-4: Temperature-dependent experimental (symbols) and simulated (lines) current density voltage characteristics of Spiro-TAD hole-only devices with a layer thickness of 100 nm, solution-processed from toluene 57

Figure 4-5: Temperature-dependent experimental (symbols) and simulated (lines) current density voltage characteristics of Spiro-TAD hole-only devices with a layer thickness of 98 nm, solution-processed from chloroform 58

Figure 4-6: AFM topography (scale bar 200 nm) of vacuum-deposited Spiro-TAD films (a) and spin-cast from toluene solution (b). The measurement area size used is $1 \times 1\ \mu m^2$. 59

Figure 4-7: Atomic Force Micrographs (scale bar 200 nm) of α-NPD films processed by (a) thermal evaporation and solutions of (b) chloroform and (c) chlorobenzene. Films processed using chlorobenzene as a solvent are found to have surface roughness comparable to the vacuum-deposited films (2.4 and 2.8 nm respectively). The film processed using chloroform is found to have higher roughness (7.7 nm). The measurement area size used is $1 \times 1\ \mu m^2$ .. 60

Figure 4-8: J-V characteristics of single-layer OLEDs with Spiro-TAD (100 nm) as the emitter layer (lines). The symbols represent the corresponding luminance-voltage characteristics. 61

Figure 5-1: a) Schematic structure of a P-i-P device b) Image of an actual device 67

Figure 5-2: Temperature dependent J-V characteristics of an undoped α-NPD (150 nm) hole-only device. Dotted lines refer to experimental measurements. Solid lines refer to numerical simulations 68

Figure 5-3 a) J-V characteristics at room temperature (295 K) of α-NPD device doped with F6TCNNQ at various concentrations b) Temperature dependence of a 0.5% doped F6TCNNQ: α-NPD device..... 70

Figure 5-4: Temperature dependent J-V characteristics of a doped α-NPD (150 nm) hole-only device for various doping concentration: a) 1% b) 1.5% c) 2%. Dotted lines refer to experimental measurements. Solid lines refer to numerical simulations. d) Doping concentration vs ionized dopant concentration. 71

Figure 5-5:a) Depletion region capacitance measurement for a 1% doped F6TCNNQ-α-NPD device. b) ionized dopant concentrations measured by impedance spectroscopy (red) and drift-diffusion simulations (black) of doped F6TCNNQ-α-NPD device for various doping densities..... 73

Figure 5-6: Extracted background hole density as a function of temperature. The activation energy amounts to 60 meV 75

Figure 6-1: Chemical structure of Spiro-OMeTAD..... 82

Figure 6-2: Temperature dependent J-V characteristics of an undoped Spiro-OMeTAD (115nm) hole-only device. Dotted lines refer to experimental measurements. Solid lines refer to numerical simulations. 84

Figure 6-3: Doping of Spiro-OMeTAD with F4TCNQ and F6TCNNQ. J-V characteristics at 295 K and comparison with undoped Spiro-OMeTAD hole only device. 85

Figure 6-4: Current density with increased doping of Spiro-OMeTAD with F6TCNNQ at 295 K..... 86

Figure 6-5 : Temperature dependent J-V measurement of F4TCNQ doped Spiro-OMeTAD. Dotted lines refer to experimental measurements. Solid lines refer to numerical simulations. a) dopant concentration of 1% b) dopant concentration of 1.5% and c) dopant concentration of 2%..... 88

Figure 6-6: Temperature dependent J-V measurement of F6TCNNQ doped Spiro-TAD. Dotted lines refer to experimental measurements. Solid lines refer to numerical simulations. a) dopant concentration of 0.5 % b) dopant concentration of 1% and c) dopant concentration of 2%..... 89

Figure 6-7: Comparison of F6TCNNQ doping in α-NPD, Spiro-TAD, Spiro-OMeTAD. a) dopant ion concentrations versus doping concentrations b) a) doping efficiency versus doping concentrations c) conductivity vs doping concentration. 90

Figure 7-1: Chemical structure of PffBT4T-2DT 99

Figure 7-2: (a) Schematic of a field-effect transistor (side view) (b) Transfer curve of a unipolar OFET comprising a p-type semiconductor. At negative gate bias current flows and the current is depleted at positive gate bias. 101

Figure 7-3: a)-b) Transfer and output characteristics of a PffBT4T-2DT monolayer ring transistor. The channel length and width are 10 μm and 2500 μm, respectively. The drain voltages used in a) are -2 V and -30 V for the measurement in the linear and saturation regimes, respectively. c-d) The distribution of saturation and linear mobility (μsat and μlin) of the polymer monolayer transistors. S/D electrodes are functionalized by 2,3,4,5,6-pentafluorothiophenol (PFBT) SAMs. Over 80 transistors were measured. 102

Figure 7-4: The saturation mobility of PffBT4T-2DT monolayer as a function of temperature. M is the saturation mobility measured at different temperatures, and μ_{RT} is the value measured at room temperature. The activation energy is around 90 meV 103

Figure 7-5: The saturation mobility and on/off ratio as a function of layer number forPffBT4T-2DT PoM-FET. It is evident that the charge carrier transport remains independent of layer number. The identical transistor performance of monolayer and multilayers provides further evidence that the first monolayer close to the dielectric is mainly responsible for the charge carrier transport. 104

Figure 7-6: The influence of channel length on the saturation (a,c) and linear mobilities (b,d) of PffBT4T-2DT monolayer. Both ring (a,b) and interdigitate transistors (c,d) are analyzed. The channel width is 1000 μm and 10000 μm for ring and interdigitate transistor. 105

Figure 7-7: a) Total device resistance (R_{total}) as a function of the channel length (L) with various V_{GS} for PffBT4T-2DT monolayer transistor. The channel width is 1000 μm. B) Contact resistance times channel width (W) as a function of V_{GS}. C) The slopes of red lines in a), $(\Delta R_{total}/\Delta L)^{-1}$, as a function of V_{GS}. According to the inset equation, the mobility calculated by transfer-length-method is 1.3 $cm^2 V^{-1} s^{-1}$, in an excellent agreement with the value extracted from the transfer characteristics. 106

Figure 7-8: Integrated circuits based on PffBT4T-2DT PoM-FETs. A) Static input–output characteristics of a unipolar inverter based on PffBT4T-2DT monolayer with V_{GS} = 0 V. The supplied voltage, V_{dd}, is −5V, −10 V, and −20 V, respectively. The inverter layout is shown as an inset. B) A PoM-FET 7-stage ring oscillator operating at a frequency of 6.16 kHz with a supply voltage of −15 V. c A PoM-FET 15-bit code generator with a bit rate of about 330 bit s^{-1} at V_{dd} = −20 V..... 107

Figure 7-9: Schematic illustration of the measurement set-up for the ring oscillator. 107

Figure 7-10: Plots of corresponding gain of polymer monolayer inverter (Figure 7-8 a)). V_{in}, input voltage; V_{out}, output voltage. The inset shows a diagram of the logic gate..... 108

Figure 7-11: The frequency of polymer monolayer ring oscillator as a function of bias voltage..... 109

Figure 7-12: Block diagram of the 15-bit code generator..... 110

List of Tables

Table 3-1 The HOMO and LUMO energy levels of the materials used in this work.....35

Table 5-1: Doping efficiencies with increasing dopant concentration of a F6TCNNQ doped α-NPD device.....74

Table 5-2: Temperature dependent p_0 values obtained from the numerical simulations of the J-V curves for 2% doped α-NPD films.....76

Table 6-1 Doping efficiency of F6TCNNQ in Spiro-TAD 91

Table 6-2 Doping efficiency of F6TCNNQ in Spiro-OMeTAD 91

Table 7-1: Device performances of PffBT4T-2DT PoM-FETs with three different geometries of source/drain (S/D) patterns.....103

Nomenclature

Acronyms / Abbreviations

α-NPD	2,2′-Dimethyl-N,N′-di-[(1-naphthyl)-N,N′-diphenyl]-1,1′-biphenyl-4,4′-diamine
AFM	Atomic Force Microsocopy
Al	Aluminium
Au	Gold
CB	Chlorobenzene
CF	Chloroform
CPX	Charge transfer complex
CTLM	Circular transfer line method
E_F	Fermi level
EGDM	Extended Gaussian disorder model
EIB	Electron injection barrier
F4TCNQ	2,3,5,6-Tetrafluoro-7,7,8,8-tetracyanoquinodimethane
F6TCNNQ	1,3,4,5,7,8-Hexafluorotetracyanonaphthoquinodimethane
FET	Field-effect transistor

HIB	Hole injection barrier
HOMO	Highest occupied molecular orbital
HTL	Hole transport layer
HTM	Hole transporting material
IC	Integrated circuit
IPA	Ion Pair Formation
ITO	Indium tin oxide
LCAO	Linear Combination of Atomic Orbitals
LUMO	Lowest unoccupied molecular orbital
MoO_3	Molybdenum trioxide
OFET	Organic field-effect transistor
OLED	Organic light emitting diode
OPV	Organic photovoltaic
OSM	Organic small molecule
PEDOT:PSS	Poly(3,4-ethylenedioxythiophene)-poly(styrenesulfonate)
PffBT4T-2DT	Poly[(5,6-difluoro-2,1,3-benzothiadiazole-4,7-diyl)[3,3'''-bis(2-decyltetradecyl)[2,2':5',2'':5'',2'''-quaterthiophene]-5,5'''-diyl]]
PoM-FET	Polymer monolayer field-effect transistor
SAMFET	Self-assembled monolayer field-effect transistor
SCLC	Space-charge limited current

Spiro-TAD	2,2',7,7'-Tetrakis(N,N-diphenylamino)-2,7-diamino-9,9-spirobifluorene
Spiro-OMeTAD	2,2′,7,7′-Tetrakis(N,N-di-p-methoxyphenyl-amine)9,9′-spirobifluorene
TCNQ	7,7,8,8-Tetracyan-chinodimethan
TCTA	Tris(4-carbazoyl-9-ylphenyl)amine
Tol	Toluene

Chapter 1

Introduction

Since the pioneering work in organic electroluminescent devices by Tang and Van Slyke in 1987 [1] there has been large progress and ever-increasing interest in Organic light-emitting diodes (OLEDs) due to their application in areas such as full color display panels and lighting sources. Both industrial and academic research has led to the development of high-performance OLEDs with considerable improvements achieved in luminance efficiency, color range, device stability and different fabrication techniques.

OLEDs have also been widely commercialized in indoor lighting, displays in consumer electronics such as mobile phones, digital cameras, wearable electronics, and ultra-high-definition televisions. The commercial lighting product first introduced was by OSRAM in the form of a table lamp in 2008 [2], this was followed by Philips who launched a commercial lighting panel in 2009 [3]. Most of the commercial lighting panels that have since followed have achieved a power efficiency of 15 to 50 lmW^{-1}. OLEDs have additionally always had a drawback of having high manufacturing costs [4].

Further optimization of OLED performance is still widely investigated due to the challenges in standardization for lighting sources and display performances. A hurdle to high-performing OLEDs since the beginning has been the design and synthesis of appropriate polymeric and small molecule-based emitters, which have the ideal electrical and optical properties essential to fully use the generated singlet and triplet excitons for energy conversion. Another roadblock is the charge injection process, which affects the utilization of charge carriers. This is mainly determined by the electric properties of the transporting materials and device

architecture. The industry standard for fabrication of OLED devices is thermal evaporation, which is preferred over solution-processed deposition of organic materials. There are considerable advantages with thermal evaporation such as thickness control and pristine deposition conditions, but there are also drawbacks such as increased cost due to the wastage of about 70 to 80% of the organic materials in the chamber and the requirement of high vacuum deposition conditions [5]. The solution processing of organic materials has considerable advantages such as cost-effective processing of organic materials, especially for mass manufacturing and is more promising for large area displays [5]. However, the major challenges of solution processing that have hindered the wide scale adoption of the technique in industrial production are: a) solubility of some organic materials in organic solvents b) blending between layers during subsequent coatings to achieve multi-layer structures and c) morphological and compositional defects due to the processing. Both fabrication processes tend to lower the overall efficiency of the OLEDs when manufactured at large scale and has been one of the major obstacles for commercialization of competitive products.

The other bottleneck for real uptake of products in the market is the instability of the hole transporting materials (HTMs) in the stack. There has been extensive work in development of HTM and they mostly consist of triarylamines and benzidines in many forms [5-8]. The three main categories are, (i) amine family (TCTA, TPT1), (ii) benzidine family (a-NPD, NPB, TPD), and (iii) spirolinked or spirocyclic fluorine (spiro-TPD, spiro-2NPB, spiro- TAD). In wide-band gaps materials such as Spiro-OMeTAD there is need for doping to achieve the necessary electrical conductivity. The selection of dopant for high efficiency is not the only hurdle, the hygroscopic nature of the dopant itself makes the layer highly hygroscopic and leads to chemical degradation and causes device instability. The doping also induces degradation of charge selective layers. Next to the hygroscopic nature of the HTM, pin holes in the film morphology, humidity and thermally induced instability all contribute to lowered efficiency. HTMs are also important active materials in other organic devices as for example in hybrid inorganic/organic perovskite solar cells, where they are responsible for efficient hole extraction and prevent undesirable recombination processes leading to an improved efficiency [9]. The efficient device operation in multi-stacked devices is dependent on the

alignment of the energy levels of the emissive layer with the transport layers. For efficient hole injection, the highest occupied molecular orbital (HOMO) of the HTL must be less negative than that of the emitter and the high lying lowest unoccupied molecular orbital (LUMO) will ensure that electrons are blocked because of the low electron affinity. It is also essential that the conductivity of the hole transport layer (HTL) is high to reduce voltage loss during charge transport from the hole injecting contact to the emissive layer. A high conductivity can be achieved by a combination of high mobility and high charge carrier density The solubility of the HTL is also critical to obtain the same characteristics as in thermally evaporated devices.

Spiro-OMeTAD has a HOMO level around -5.1 eV and exhibits a hole mobility of 10^{-5} to 10^{-4} cm^2 $V^{-1}s^{-1}$ and has high solubility in organic solvents such as toluene or chlorobenzene [10]. There has been considerable research interest in the charge transport in HTMs in recent years. However, the clear correlation between fabrication and its dependencies on the transport has not been fully understood. There are also few reports that discuss the correlation between molecular structures and dopants, and carrier drift mobilities [10-12]. It is essential to understand the charge-transport parameters which have been obtained by the analysis of the charge-carrier drift mobilities in terms of the disorder of the materials. It has also been found that the films and their composition offer differences in transportation based on both the thickness and the device structure [13], hence this work not only focuses on different fabrication techniques for a range of small molecular hole transporting materials, but also uses different devices structures to investigate the transport, such as p-i-p devices, hole-only diodes and field-effect transistors and finally integrated circuits to investigate a real-life application of the monolayer.

Therefore, in the course of this thesis a selected system of investigations was performed to gather deeper insight into the phenomenon associated with processing of organic semiconductors and its effect on charge transport and device performance. The thesis is organized as follows:

- Chapter 2 is a primer and provides an overview of the main theoretical concepts that are necessary to comprehend the experimental analysis that are described in the following chapters in the thesis
- Chapter 3 provides a description of the key materials used and the experimental techniques for fabrication, characterization, electrical and optical measurements.
- Chapter 4 investigates the effect of solvents used for solution processing of organic small molecules and their effect on device performance
- Chapter 5 investigates the charge transport in thermally co-evaporated doped organic small molecules and the resulting doping efficiency when compared between different host-matrix systems
- Chapter 6 investigates the charge transport in solution-processed doped organic small molecules and the resulting doping efficiency when compared between different host-matrix systems
- Chapter 7 is an investigation of the transport properties of a polymeric monolayer organic field effect transistor of difluorobenzothiadiazole-oligothiophene copolymer (PffBT4T-2DT) with further development of the OFETs into logic gates, ring oscillators and integrated circuits
- Chapter 8 summarizes the findings of the investigations in this thesis and discusses the promising concepts and its future applications

References

[1] C.W. Tang and S. A. VanSlyke, Appl. Phys. Lett **51**, 913 (1987).

[2] C. Bölling, "Osram presents PirOLED, the first OLED luminaire", https://www.ledsmagazine.com/company-newsfeed/article/16690734/osram-presents-piroled-thefirst-oled-luminaire, 2010.

[3] R. Mertens, "Philips lumiblade OLED light - first looks", https://www.oled-info.com/philips-lumiblade-oled-light-first-looks, 2009.

[4] M. Halper, "OLEDs still face a cost challenge in general lighting", https://www.ledsmagazine.com/leds-ssl-design/article/14039209/oleds-still-face-a-cost-challenge-in-general-lighting-magazine, 2019.

[5] T.-W. Lee, T. Noh, H.-W. Shin, O. Kwon, J.-J. Park, B.-K. Choi, M.-S. Kim, D. W. Shin, and Y.-R. Kim, Adv. Funct. Mater. **19**, 1625 (2009).

[6] Y. Chen, H. Tian, Y. Geng, J. Chen, D. Ma, D. Yan, and L. Wang, J. Mater. Chem. **21**, 15332 (2011).

[7] A. Srivastava and B. Kumar, "Organic light emitting diodes-recent advancements", in 2017 14th IEEE India council international conference (INDICON) (2017), pp. 1–6.

[8] Q. Zhang, J. Chen, Y. Cheng, L. Wang, D. Ma, X. Jing, and F. Wang, J. Mater. Chem. **14**, 895 (2004).

[9] Q.-X. Tong, S.-L. Lai, M.-Y. Chan, K.-H. Lai, J.-X. Tang, H.-L. Kwong, C.-S. Lee, and S.-T. Lee, Chem. Mater. **19**, 5851 (2007).

[10] Y. Shirota and H. Kageyama, Chem. Rev. **107**, 953 (2007).

[11] J. Li, I. Duchemin, O. M. Roscioni, P. Friederich, M. Anderson, E. Da Como, G.Kociok-Köhn, W. Wenzel, C. Zannoni, D. Beljonne, X. Blase, and G. D'Avino, Mater. Horiz. **6**, 107 (2019).

[12] S. Fratini, , M. Nikolka, A. Salleo, et al., Nat. Mater. **19**, 491 (2020).

[13] L. Wang, S. Guo, K. Zhou, W. Ma, Sustain. Energy Fuels **4**, 4934 (2020).

Chapter 2

Theoretical fundamentals

2.1 Organic semiconductors

Inorganic semiconductors have played a dominating role in electronics since the invention of the transistor in the middle of the 20th century. The advance of society and technology has been rapidly fueled due to the ever-prevailing silicon based electronic devices. However, organic material-based devices have been rapidly advancing due to many advantages they offer over inorganic materials such as low cost, flexibility, scalability, and potential usage in transparent devices [1]. The key materials used can be classified into two groups for organic semiconductors: low molecular weight (small) molecules that are typically processed in vacuum and conjugated polymers, which are typically processed from solution. Typical examples for the two classes are shown in Figure 2-1. The common feature is the conjugation i.e., alternation of the single and double bonds along the backbone, which is responsible for their semiconducting properties [2].

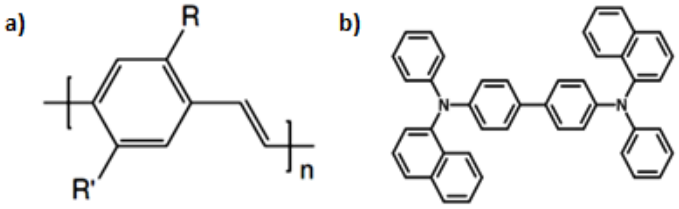

Figure 2-1 Chemical structures of a) poly(p-phenylene vinylene) (PPV) b) α-NPD

In an organic semiconductor the electronic structure is dominated by their conjugated π-system formed by sp^2-hybridized carbon atoms. The ground state of a carbon atom is $1s^2\ 2s^2\ 2p^2$. In order to be energetically favorable, the atomic orbitals of the valence electrons are hybridized, i.e., the linear combination of the 2s-orbital with the 2p-orbitals, where the 2s-orbital is combined with one, two or all three of the 2p-orbitals which is referred to as sp, sp^2 and sp^3 hybridization. The sp^2 hybridization is crucial for the formation of conjugated π-systems. In this case, the hybridization of the valence orbitals in the carbon atom (2s, $2p_x$, $2p_y$) forms three degenerate sp^2-orbitals with one p-orbital (p_z) remaining, schematically shown in the Figure 2-2 a). The three sp^2-orbitals are oriented in-plane at 120 degrees relative to each other and the p_z orbital is perpendicular to the plane. In a conjugated polymer, every carbon atom contributes two sp^2 orbitals and forms a covalent bond with the two adjacent carbon atoms called a σ-bond. The remaining p_z orbitals overlap above and below the plane and form another covalent bond, which is called a π-bond. The π-orbital is delocalized across the σ-bond above and below the nodal plane of the π-bond. The electrons in the π-bond are delocalized along the chain and are then associated with a molecular orbital. The contribution of these π-electrons to the bonding of the molecule is small and excitation of the π-electrons will not cause scission of the backbone σ-bonds, hence the structural integrity of the molecule is retained.

2.2 Linear combination of atomic orbitals

The description of the σ-bond and the π-bond is based on the linear combination of atomic orbitals method, where the molecular orbitals are approximated by a linear combination of the involved atomic orbitals [3]. In the Linear Combination of Atomic Orbitals (LCAO) it is assumed that the number of molecular orbitals and the sum of all involved atomic orbitals are equal. To construct the wavefunctions of the molecular orbitals ψ_j, the wavefunctions of the atomic orbitals ϕ_i can be used in a linear combination

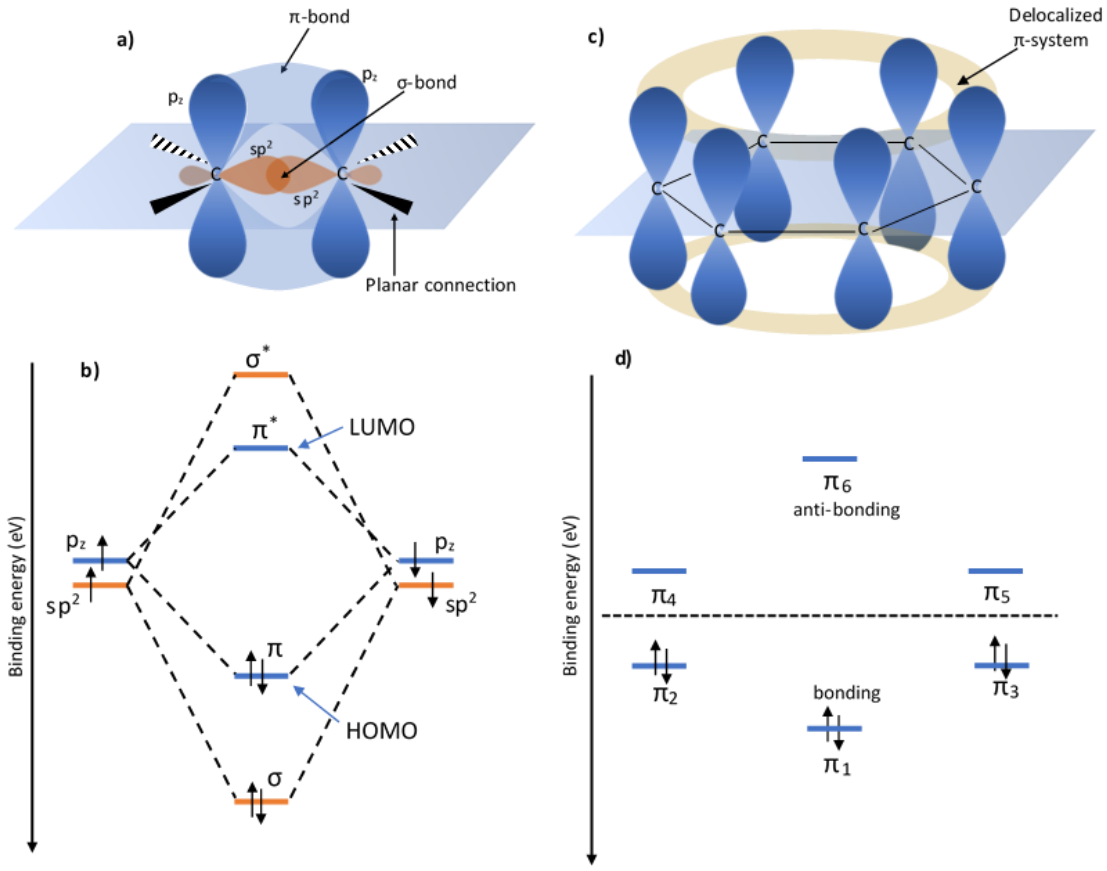

Figure 2-2 a) sp^2 hybridization of carbon atoms. b) highest occupied molecular orbital (HOMO) and lowest unoccupied molecular orbital (LUMO) level formation due to hybridization c) Molecular bonding in benzene d) Energy levels in benzene by the Hückel Method with degenerate HOMO and LUMO states.

$$\psi_j = \sum c_{ij}\phi_i, \tag{2.1}$$

where c_{ij} is determined by minimization of the total energy of the system.

The energy levels E_j of the molecule can then be calculated using the molecular orbital wavefunctions

$$E_j = \frac{\langle \psi_j | \hat{H} | \psi_j \rangle}{\langle \psi_j | \psi_j \rangle}, \tag{2.2}$$

where $\hat{H}$ denoted the Hamiltonian of the system. The energy levels of the σ- and the π-orbitals are represented in Figure 2-2 b) The energy levels of the sp^2 orbitals split into a bonding and antibonding orbital. The interaction between the π-electrons creates a bond length alteration which is called Peierls distortion. As a result, an energy gap is created between the HOMO and the LUMO. Here the HOMO is constituted by a π-orbital and the LUMO is made up of a π*- orbital.

An example of a π-conjugated system is the benzene molecule, which is shown in Figure 2-2 c). Each p-orbital contributes one electron, therefore there are 6 π-electrons which are delocalized over the whole carbon ring.

To analytically calculate the energy levels of the π-conjugated system, the Hückel method can be used which is based on the LCAO approach. By using the Rayleigh-Ritz method of the variation principle the minimization of the total energy of the system can be performed by minimizing the Eigenvalues of the energy with respect to the co-efficient c_{ij}.

$$\frac{\partial}{\partial c_{ij}} \langle \psi_j | \hat{H} | \psi_j \rangle = 0 \tag{2.3}$$

Inserting this into the above equation, a linear set of equations is obtained, which has only a non-trivial solution if

$$\left| H_{ij} - S_{ij} \right| = 0, \tag{2.4}$$

where $H_{ii} = \langle \phi_i | H | \phi_i \rangle$ is the Coulomb integral, $H_{ij} = \langle \phi_i | H | \phi_j \rangle$ is the resonance integral (for $i \neq j$) and $S_{ij} = \langle \phi_i | \phi_j \rangle$ is the overlap integral.

In the Hückel method [4], in order to simplify the problem, the π-orbitals are treated separately from the σ-orbitals by considering the interactions between the p_z orbitals of the neighboring carbon atoms of the π- system. The Coulomb integrals are set to be equal, hence

$H_{ii} = \alpha$, resonance integrals are only considered from neighboring atoms, $H_{ij} = \beta$ ($H_{ij} = 0$ for non-neighboring atoms) and overlap of the wavefunctions of different atoms is neglected, $S_{ij} = \delta_{ij}$. With these approximations, the equation can be expressed as a polynomial equation on the order of the number of involved carbon atoms, which can be analytically solved. Figure 2-2 d) shows the calculated energy levels of benzene, where the HOMO and LUMO levels are degenerate states.

The interaction between the π-electrons creates a bond length alteration which is called Peierls distortion [5]. As a result, an energy gap is created between the HOMO and the LUMO, which is an intrinsic property of the molecule. The energy gap of the semiconductor lies between 1-4 eV which makes them suitable for optoelectronic applications [6]. Optical excitations from the bonding to antibonding orbitals are also energetically feasible in the molecule as shown in the Figure 2-2 b). In organic semiconductors, the HOMO and LUMO form localized charge-transport states, which play a similar role to the valence and conduction band in inorganic semiconductors.

The length of the conjugated molecule and the side groups influence the energetic position of the HOMO and LUMO levels and hence the energy gap of the system. Therefore, by tailoring the properties of the molecules, the electronic and optical properties can be altered. When the size of the π-conjugated system increases, the energy gap is reduced. If electron donating side groups are present as side chain in the molecule, such as phenyl and amine groups, then the HOMO-LUMO energy values are raised in comparison to the unsubstituted system. Similarly, the presence of electron withdrawing groups, such as halides and nitro, can be used to lower the HOMO and LUMO levels. Also altering the side chain helps to improve the solubility and stability in solution. If alkyl groups are added to the molecule the solubility can be improved without drastically changing the optical or electronic properties.

2.3 Organic light emitting diodes

A typical OLED consists of multiple layers of organic materials sandwiched between two electrodes. However, in its most simplified form, an organic light emitting diode consists of a single layer of an organic semiconductor sandwiched between two metallic electrodes, one of which is transparent in order to transmit the light that is generated inside the OLED [6]. Figure 2-3 shows the schematic of a typical OLED structure.

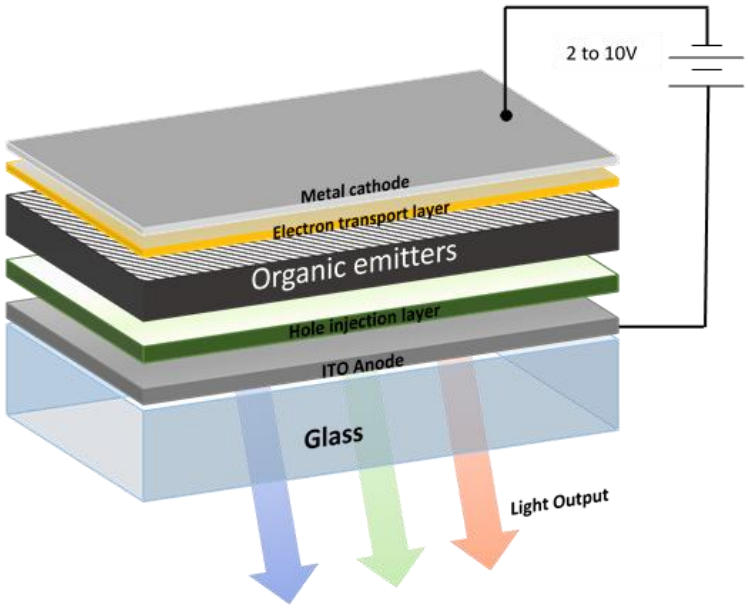

Figure 2-3 Schematic of a multilayer OLED structure

The three main processes in the operation of an OLED are i) charge injection i.e., when a voltage is applied between the electrodes, charges are injected into the organic semiconductor layer. For efficient charge injection, the work function of the anode and cathode are chosen such that they match the HOMO and LUMO of the organic semiconductor to obtain Ohmic contacts. This leads to a difference in the work function of the anode and cathode, which creates a built-in voltage. Only when the applied voltage is larger than the built-in voltage, holes and electrons are efficiently injected from the anode and cathode, respectively. The second process is ii) charge transport, due to the applied voltage an electric field is generated that helps transport the holes and electrons towards each other in the semiconductor layer.

The third process is iii) charge recombination. When the hole and electron recombine, a neutral exciton i.e., a bound state of an electron-hole pair is formed. The radiative decay of an exciton results in a photon of which the energy is determined by the energy gap of the organic semiconductor, and, as a result, determines the wavelength of the emitted light. The light is then transmitted through the transparent electrode.

2.4 Organic field-effect transistors

An organic field-effect transistor (OFET) is a three-terminal device, which comprises a semiconducting channel between a source and a drain electrode [7-9]. A typical structure of an OFET is shown in Figure 2 4. In an OFET, an organic semiconductor is used. OFETs are the basic building block for flexible integrated circuits and displays. The gate dielectric provides the electrical separation of the gate electrode from both the source and drain electrodes and the conductive channel.

When the charge carriers are injected at the source, they traverse through the channel and are then collected at the drain. The role of the gate on the channel can be modelled by considering the transistor as a parallel plate capacitor. The gate electrode and the organic semiconductor represent the parallel plates. When a positive (negative) bias is applied to the gate electrode, this results in accumulation of electrons (holes) in the organic semiconducting channel. The accumulated carriers in the channel can be controlled by modifying the applied gate bias, as the number of accumulated carriers is directly proportional to the product of the applied gate bias and the capacitance of the gate electric. Traps present at the gate-dielectric interface or in the semiconductor are filled preferentially before creating mobile carriers and therefore not all induced charge carriers are mobile. The threshold voltage (V_{th}) is the gate voltage/bias at which the current starts to flow. The gate bias is swept while the source and drain current is monitored, keeping the source and drain bias fixed. In the linear regime, the drain bias is much smaller than the gate bias. In the saturation regime, the drain bias is much larger than the gate bias.

The amount of charge carriers flowing through the channel can therefore be controlled by applying a voltage on the gate electrode. In an ideal field-effect transistor, without application of the gate voltage there is no current flowing in the channel i.e., it is in the OFF state. Upon applying a voltage on the gate electrode, current flows from the source to the drain electrode i.e., the transistor turns 'ON'. The on-off current ratio characterizes the ability of the device to switch off. A high on-off ratio is preferred and can be as high as 10^7 in organic transistors [10]. The charge carrier mobility in the organic semiconductor should be high and is a critical parameter for device performance in order to obtain high enough source-drain currents which can then be modulated by applying a gate voltage.

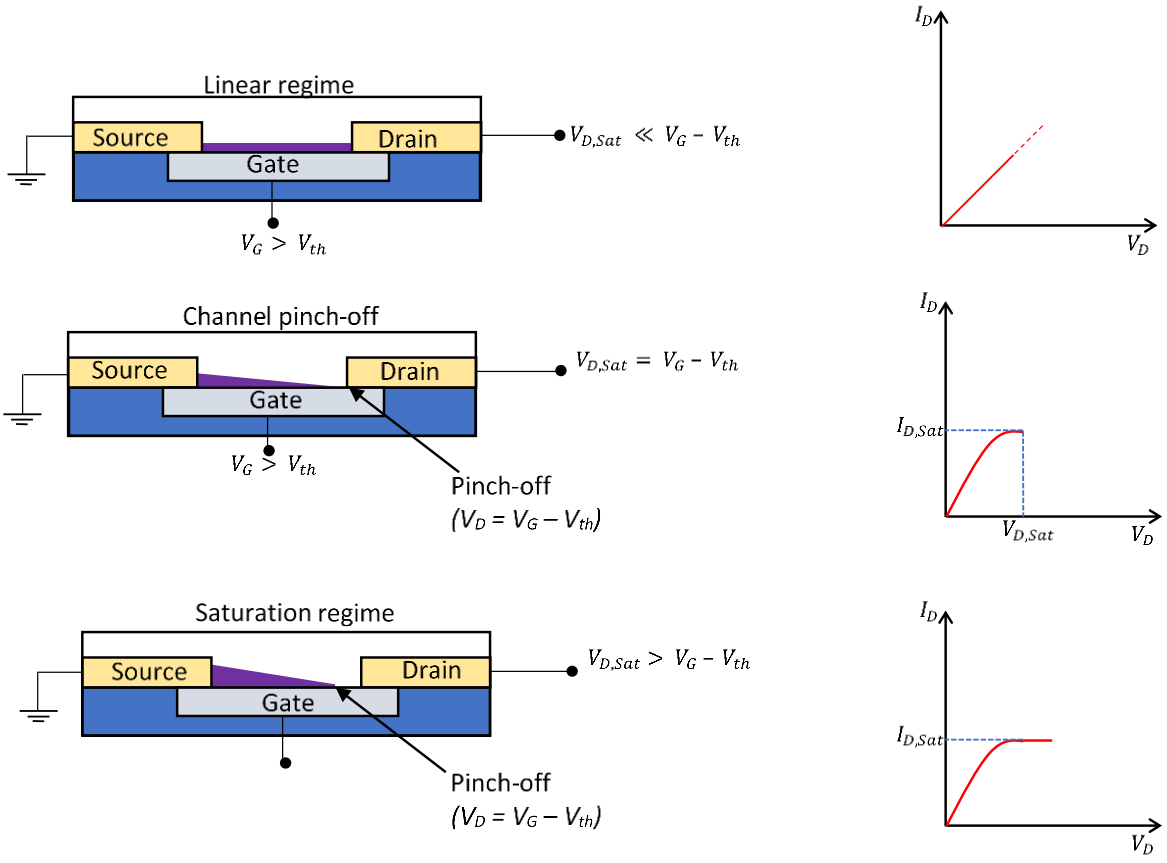

Figure 2-4 Operation regimes for an OFET and typical I-V characteristics

The transport in the OFETS can be derived analogously to the classical inorganic MOSFETs, and in the linear regime ($|V_d| << |V_g - V_{th}|$) the source and drain current is given by [11],

$$I_{sd}^{lin} = -\mu_{lin}\frac{C_{ox}W}{L}(V_g - V_{th})V_d \tag{2.5}$$

where W and L are the width and length of the channel, C_{ox} is the geometric gate capacitance and μ is the mobility of the charge carrier.

The mobility can be obtained from the first derivate of the source and drain current to the gate bias as [11],

$$\mu_{lin} = \frac{L}{V_d C_{ox} W}\frac{\partial I_{sd}}{\partial V_g} \tag{2.6}$$

When $|V_d| >> |V_g - V_{th}|$, the drain/source current is given by [11],

$$I_{sd}^{lin} = -\mu_{sat}\frac{C_{ox}W}{2L}(V_g - V_{th})^2. \tag{2.7}$$

The mobility is then obtained by taking the second derivate of the source and drain current to the gate bias [11],

$$\mu_{sat} = -\frac{L}{C_{ox}W}\frac{\partial^2 I_{sd}}{\partial V_g^2} \tag{2.8}$$

2.5 Charge-transport models for organic semiconductors

The intrinsic charge-carrier density of thermally excited charge carriers in organic semiconductors is generally very low in comparison to inorganic semiconductors[1]. Based on the height of the injection barrier of the device, the device current could either be limited by

[1] This is however dependent on the band gap and the doping of the material

the charge injection or by the bulk transport. The most effective way to investigate the injection barrier and charge transport in organic semiconductors is by using single-carrier devices, in which only one charge carrier type i.e., either holes or electrons dominate the transport characteristics. Single-carrier devices can be fabricated by matching the contact work functions with either the conduction band edge to probe electron transport or with the valence band edge to probe hole transport. Single-carrier devices used to probe electrons are called electron-only device and devices used to probe holes are called hole-only device.

When the contacts are ohmic, the current through a single-carrier device is limited by the bulk transport and is called space-charge limited current (SCLC) [12-13]. For undoped/intrinsic semiconductors in this regime, the number of charges injected into the device per unit time is limited by the electrostatic field due to the space–charge formation in the bulk of the organic semiconductor. Based on the Mott-Gurney law, which is the drift-only approximation of a trap-free SCLC, the current density is proportional to the square of the voltage applied and is inversely related to the device thickness to the third power and is given by [14]:

$$J_{SCLC} = \frac{9}{8}\varepsilon_0\varepsilon_r\mu\frac{V^2}{L^3}, \tag{2.9}$$

where ε_0 and ε_r are the vacuum and relative permittivity of the semiconductor, respectively.

The intrinsic charge carrier density n of a semiconductor in general can be estimated using Boltzmann statistics by [15-16]

$$n(T) = N_{eff}e^{-\frac{E_g}{k_BT}} \tag{2.10}$$

where N_{eff} is the effective density of states, E_g the energy gap of the semiconductor, k_B Boltzmann's constant and T the absolute temperature.

The intrinsic charge carrier density is usually in the range of 10^{-5} to 10^{3} cm^{-3} for organic semiconductors, whereas for inorganic semiconductors it lies in the range of 10^{10} to 10^{13} cm^{-3}.

The charge carrier density for organic semiconductors, depending on the band gap and purity it can be made extrinsic either by injecting charges or doping.

The charge-carrier mobility is one of the most important parameters to characterize the charge transport in semiconductors. The mobility is defined as

$$\mu = \frac{v}{E} \tag{2.11}$$

where v is the average drift velocity of a charge carrier and E is the electric field.

In organic semiconductors, charge transport occurs due to a phonon-assisted hopping process between localized states. Due to conformational variation of molecules or polymers, these localized states are distributed in energy. This energetic density-of-states (DOS) distribution is commonly referred to as energetic disorder. This is in contrast to inorganic semiconductors which have a periodic lattice and therefore exhibit delocalization of charge carriers with a large mean-free path. In inorganic semiconductors, charge transport is limited by scattering of the charge carriers due to phonons, which results in a reduction of mobility at higher temperatures due to increased phonon scattering [17]. In contrast, not only do organic semiconductors have a lowered mobility due to the high disorder and amorphous structure, but the mobility also lowers with reduction in temperature [16]. In addition, there are also physical defects in a polymer chain which cause a conjugation breakage. The consequence is observed in the energy distribution of the site energies resulting in a term referred to as energetic disorder. The energetic distribution of the DOS is frequently approximated by a Gaussian distribution, with about a width in the range of 0.05-0.2 eV for most organic small molecules and polymers. Increasing the temperature increases the thermally-assisted hopping rates, and therefor leads to an increase in charge-carrier mobility with temperature.

In addition to the mobility obeying Arrhenius' law for temperature activated transport, energetic disorder also is responsible for a dependence of the mobility on electric field [19-20]. Empirically, this can be described by the Poole-Frenkel model, which describes the mobility as a function of field and temperature as [21]

$$\mu(T,E) = \mu_\infty e^{-\frac{E_A}{k_B T}} e^{\gamma\sqrt{E}} \tag{2.12}$$

where μ_∞ is the mobility at $T \to \infty$ and $E = 0$, E_A is the activation energy, k_B the Boltzmann constant, T is the absolute temperature, E the electric field, and γ is a field-activation parameter.

Although the Poole-Frenkel model qualitatively describes the field and temperature dependence of the mobility in organic semiconductors, it is empirical and cannot be used for all materials. An improved charge transport model was proposed by Bässler et al., where the hopping sites are assumed to be localized and the adjacent site energies are assumed to be uncorrelated [22]. The energetic sites are given by a Gaussian distribution in energy and the mobility is dependent on how fast charge carriers hop from one site to a neighboring site and in turn depends on the energetic difference and spatial distance between hopping sites. When under thermal equilibrium, the charges in the semiconductor are 'relaxed' with the mean of their distribution located at the equilibrium energy level $E_{eq,e}$, which is present at $\frac{\sigma^2}{k_B T}$ below $E_{0,e}$, the center of the density of states. Charges need to be excited to the transport energy level, $E_{a,e}$ as very few transport sites are present at $E_{eq,e}$. There are enough transport sites at the transport energy level for the charges to hop from one site to the other. It has been theoretically calculated to show that the transport energy level, $E_{a,e}$is located near the center of the DOS at $\frac{\sigma^2}{18 k_B T}$ [22-25].

Under the influence of an external electric field, the difference in energies of the individual sites decrease. The probability of an electron to jump to a site of higher energy increases resulting in a direct dependence of the mobility on the electric field. In addition, it is found that charge carriers located around $\frac{\sigma^2}{2 k_B T}$ jump to the transport energy level and the temperature-dependent activation energy ($\frac{4\sigma^2}{9 k_B T}$) therefore results in a temperature dependence of the mobility [22-25].

$$\mu_{GDM} = \mu_{\infty} exp\left[-\left(\frac{2\sigma}{3k_BT}\right)^2\right] \times exp\left[C\left(\left(\frac{\sigma}{k_BT}\right)^2 - \Sigma^2\right)\sqrt{E}\right], \text{For } \Sigma \geq 1.5$$

(2.13)

$$\mu_{GDM} = \mu_{\infty} exp\left[-\left(\frac{2\sigma}{3k_BT}\right)^2\right] \times exp\left[C\left(\left(\frac{\sigma}{k_BT}\right)^2 - 2.25\right)\sqrt{E}\right], \text{For } \Sigma < 1.5$$

where μ_{∞} is a mobility prefactor $T \to \infty$, $C = 3 \times 10^{-4}\ \mathrm{cm}^{\frac{1}{2}}\mathrm{V}^{-\frac{1}{2}}$ is a numerical constant dependent on the site separation and Σ represents the degree of positional disorder of hopping sites. This model for the charge-carrier mobility considers the temperature and electric field dependence. However, the mobility is also dependent on the charge carrier concentration (*n* for electrons and *p* for holes), which, in a device, are injected by the application of an electric field.

In the EGDM this dependence of the charge carrier mobility on the density is also taken into account [26]. The mobility both increases with increasing charge-carrier density and electric field. The following parametrized equation summarizes all the mobility dependencies to give [27],

$$\mu_{EGDM}(T, p, E) = \mu_{np}(T, p) \times \mu_E(T, E) \tag{2.14}$$

where $\mu_{np}(T, p)$ describes the temperature and carrier density dependence and is given by

$$\mu_{np}(T, p) = \mu_0 C_1 \exp\left[-C_2\left(\frac{\sigma}{k_BT}\right)^2 + \frac{1}{2}\left(\left(\frac{\sigma}{k_BT}\right)^2 - \left(\frac{\sigma}{k_BT}\right)\right)(2pa^3)^{\delta}\right] \tag{2.15}$$

And δ is given by

$$\delta = 2\frac{\ln\left(\left(\frac{\sigma}{k_BT}\right)^2 - \left(\frac{\sigma}{k_BT}\right)\right) - ln\big(ln(4)\big)}{\left(\frac{\sigma}{k_BT}\right)^2} \tag{2.16}$$

where $\mu_{np}(T, p)$ describes the temperature and carrier density dependence.

$$\mu_E(T, E) = \exp\left[0.44\left(\left(\frac{\sigma}{k_BT}\right)^{\frac{3}{2}} - 2.2\right) \times \sqrt{1 + 0.8\left(\frac{Eea}{\sigma}\right)^2} - 1\right] \tag{2.17}$$

When $p \to 0$ and $E \to 0$ the equation can be simplified to obtain the temperature dependence of mobility.

$$\mu_0(T) = \mu_0 C_1 \exp\left(-C_2 \left(\frac{\sigma}{k_B T}\right)^2\right) \tag{2.18}$$

where $\mu_0 = \frac{a^2 v_0 e}{\sigma}$.

μ_0 is the mobility prefactor, v_0 is the attempt to hop frequency, e is electronic charge, σ the width of the Gaussian disorder, k_B is Boltzmann's constant, T is the temperature and a is the lattice constant. $C_1 = 1.8 \times 10^{-9}$ and $C_2 = 0.42$ are constants.

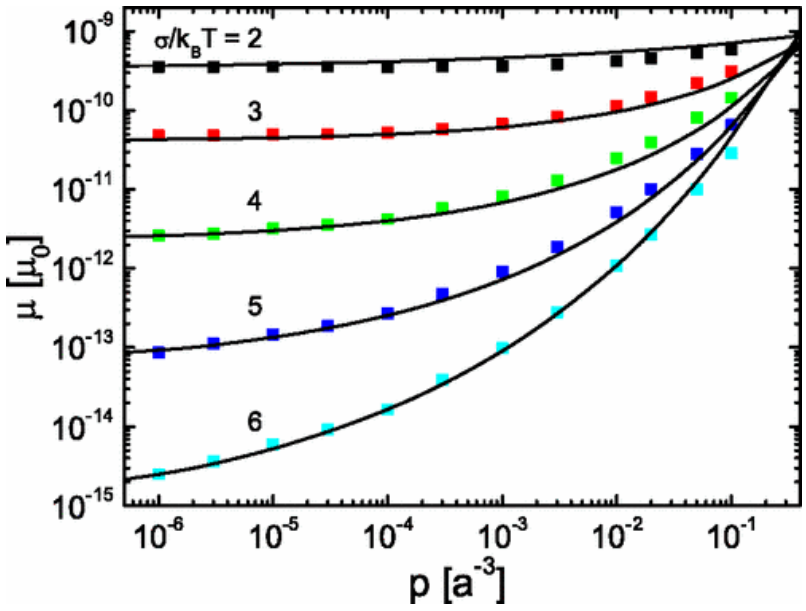

Figure 2-5 Dependence of the mobility on charge-carrier density at vanishing electric field for different values of the dimensionless disorder parameter ($\frac{\sigma}{k_B T}$) for different temperatures in units of μ_0. Solid lines are the fits using the parametrization scheme in Eq. 2.18. Symbols are the numerical results. Reproduced with permission from [28]

2.6 Device characteristics

In an organic-semiconductor device, the charges are injected at the electrode interfaces. The electrodes are typically made of metals or metal oxides. The energetic difference between the Fermi level E_F of the electrode and the HOMO is called the hole injection barrier (HIB), while the difference between E_F and the LUMO onset is called the electron injection barrier (EIB).

When the injection barrier is low, the flow of the current is limited by the semiconductor and not by the contacts, such a contact is called an Ohmic contact [28]. This contact can be made selective to holes or electrons as explained below. However, the injection barriers can also be high, resulting in resistance to injection of carriers leading to an injection limited current.

In non-Ohmic contacts the charge injection consists of two processes by which the energetic barriers are overcome on the application of an electric field. In the first process, an electron at the Fermi level of the electrode tunnels through the barrier which is reduced due to the externally applied electric field. This effect is called Fowler-Nordheim tunneling and is dominant for large electric fields and at low temperatures [29]. In the second process i.e., the thermionic injection, a thermally activated electron can overcome the tilted barrier. In both cases, the barrier is lowered by an image charge induced by the electron at equal distance to the interface, which is called the Schottky-effect [30,31].

In both OLEDs and OFETs the most important process is the transport of charge-carriers. In order to isolate and study the transport of the individual carriers, electron and hole-only devices can be fabricated. Such devices consist of one injecting electrode for Ohmic charge injection and a counter electrode, which blocks the injection of the opposite sign charge carrier. In a hole-only device the high work function of the anode used provides Ohmic hole injection into the HOMO and the work function of the cathode is chosen to be sufficiently high to create an injection barrier which is large enough to prevent electron injection into the LUMO [32-33]. This results in a pure hole current as there are no injected electrons

contributing to this. Similarly, an electron only device can be created which will have a pure electron current due to the absence of hole injection.

2.7 Doping in organic semiconductors

The doping of organic semiconductors allows to control the charge transport properties in an organic semiconductor by increasing the charge carrier density, while additionally facilitating charge injection from the contacts. The initial process of doping involved strongly oxidized gases and later small atoms were used to improve the conductivity [34, 35]. However, in both methods, the devices were found to be instable due to a tendency of the dopants to diffuse in the organic layers and thereby causing degradation. A more efficient and stable way to dope organic semiconductors is to use molecular dopants which due to their larger size are found to be less prone to diffusion than atomic dopants [33].

2.8 Mechanisms of doping

In inorganic semiconductor technology, doping is widely used to improve the density of charge carriers. By incorporating impurity atoms such as pentavalent impurities like phosphorus or trivalent impurities like boron into the crystalline semiconductor host material of silicon with four valence electrons either n-type or p-type doping is achieved [36]. If a trivalent impurity is used, it increases the density of holes and if a pentavalent impurity is used, it increases the density of electrons [36]. Based on classical semiconductor theory, the density of negative n_0 and positive p_0 charge carriers in an undoped semiconductor can be calculated from Fermi-Dirac statistics depending on the position of the conduction band E_C and valence band E_V to be [36],

$$n_0 = N_C \cdot e^{\frac{E_F - E_C}{k_B T}} \; and \; p_0 = N_V \cdot e^{\frac{E_V - E_F}{k_B T}} \tag{2.19}$$

where N_C is the effective density of states in the conduction band and N_V is the effective density of states in the valence band.

In case of intrinsic semiconductors, $n_0 \approx p_0$ and the Fermi level is located close to the center of the gap where $E_g = E_C - E_V$ and is hence the Fermi level energy is given by,

$$E_F = \frac{E_g}{2} + \frac{k_B T}{2} \ln\left(\frac{N_V}{N_C}\right) \tag{2.20}$$

The introduction of the impurity atoms with a density of N_D leads to shallow donor states with E_D located below the conduction band edge, which leads to a shift of the Fermi level towards the conduction band. Similarly, when acceptor states with E_A are introduced above the valence band edge due to the presence of the acceptor atoms with density N_A in a p-type semiconductor, there is a shift of the Fermi level towards the valence band [36].

$$|E_C - E_D| < \left|k_B T \ln\left(\frac{N_D}{N_C}\right)\right| \text{and} |E_V - E_A| < \left|k_B T \ln\left(\frac{N_A}{N_V}\right)\right| \tag{2.21}$$

In extrinsic semiconductors, the shallow states are located at the band edge and their ionization energy is less than room temperature thermal energy and hence the dopant atoms are ionized even below room temperature. In comparison, in an intrinsic semiconductor the ionization energy can sometimes be higher than room temperature thermal energy. Hence in a doped semiconductor, the number of mobile charge carriers is independent of the temperature and is directly proportional to the number of dopant atoms present.

The fermi level is thus given by

$$E_F = E_C - k_B T \left(\frac{N_C}{N_D}\right) \text{and } E_F = E_V + k_B T \left(\frac{N_V}{N_A}\right) \tag{2.22}$$

which shows that the number of carriers, the conductivity and the position of the Fermi level can be controlled precisely by changes in the dopant concentration N_D and N_A [36]. For dopant concentrations in the range of 10^{-7} to 10^{-4} (atomic ratio), this leads to dramatic

increases in conductivity as the crystallinity of the semiconductor is largely undisturbed at these dopant concentrations, which leads to a retention of the charge carrier mobility [36-37].

However, the doping mechanism is largely different in organic semiconductors. The use of small atoms like halides or alkali metals as dopants led to device instabilities, which were found to be linked to the tendency of these small dopants to diffuse throughout the organic layer [38], in contrast to inorganic semiconductors where the dopants are covalently bound to the host atom. In order to overcome this issue, small donor or acceptor molecules were used as molecular dopants which given their size have a smaller tendency to diffuse [39, 40]. The usage of dopant molecules leads to an increase in conductivity by several orders of magnitude and thereby enables high performance devices. [39, 40]

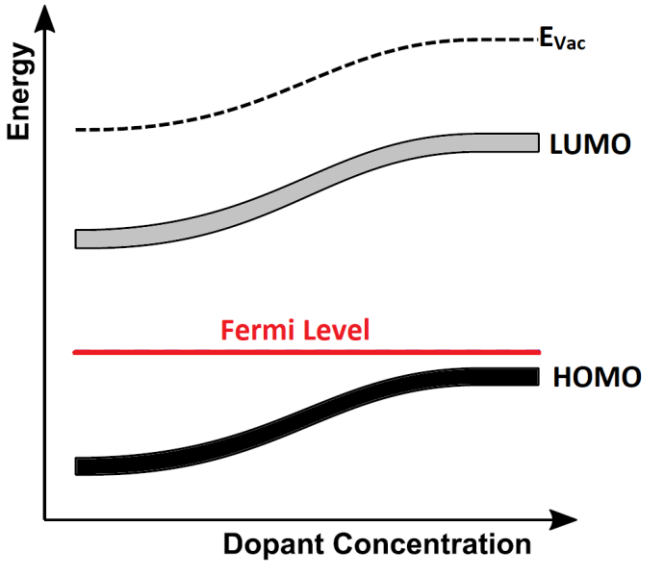

Figure 2-6 Shift of the Fermi level for a p-doped organic semiconductor. With increasing dopant concentration, the Fermi level moves towards the HOMO level

As discussed above in the case of inorganic semiconductors, doping leads to a shift of the Fermi level which is also found to be true for organic semiconductors. The Fermi level moves increasingly towards the respective transport level i.e., HOMO for p-type and LUMO for n-type doping with increasing dopant concentrations [15, 36-37]. In contrast to the doping behavior in inorganic semiconductors, there is a saturation in both the conductivity and the

Fermi level shift at few mole-percent dopant concentrations (up to 10%). As shown in Figure 2-6, there is a pinning of the Fermi level at the edge of the respective transport level and hence at a particular dopant concentration (which is material dependent), the shift stops [41].

Another contrast to inorganic semiconductors is that the doping efficiency of molecular dopants is found to be very low. This necessitates the use of dopant concentrations in the order of mole percent. This in turn influences the morphology and structure of the thin films. For pristine films that are crystalline, the addition of the dopants leads to an amorphous growth and therefore a reduction in mobility. For ordered materials this reduction in mobility has a greater impact on the conductivity than the doping effect of an increased charge carrier density [42]. This effect however reverses at sufficiently high dopant concentration, at which point the increase in the charge carrier density will outweigh the decrease in mobility and cause a net increase in the conductivity again. For amorphous organic semiconductors, however, this effect is found to be different [43, 44]. With decreasing order, the mobility decrease due to doping is smaller than the increase in charge carrier density, at low electric fields and low dopant concentrations. Therefore, there is a strong increase in conductivity. However, at very high dopant concentrations the doping efficiency is found to decrease with increasing dopant concentration resulting in a decrease in conductivity [44].

At the beginning of the doping research in organic semiconductors, gases like iodine, bromine and chloride were the most commonly used p-dopants [45-46]. However, it has been observed that due to the tendency of the atomic dopants to diffuse, there is device instability. This led to the development of molecules with a quinone structure and unsatisfied aromatic rings which are the most popular variety of p-dopants. TCNQ is the standard molecule used from this class and has been studied in great detail as it has an ability to form charge-transfer complexes when used with small molecular donors. The biggest limitation of TCNQ has been its electron affinity of 4.2 eV, which prevents usage in most organic semiconductors having ionization energies in the range of 5-6 eV [36]. This is the main reason that there has been considerable research and development of other molecules to be used for doping a wider range of organic semiconductors and leading to considerable industrial applications.

Despite the advantages such as tuning of the optical gap through varying the chemical compositions and large area processability, the usage of organic molecules is still limited due to the low doping efficiencies observed which in turn points to the lack of in depth understanding of the mechanisms behind molecular doping in comparison to the inorganic semiconductors.

There are primarily two distinct mechanisms identified based on the phenomena observed during doping of organic semiconductors: the ion-pair formation and the charge-transfer complex formation [47].

2.8.1 Ion Pair formation

On doping an organic semiconductor with a p-type dopant, the underlying assumption for the ion pair formation (IPA) is that the electron affinity of the acceptor is the same or higher than the ionization energy of the host such that it facilitates the transfer of one electron from the HOMO of the host to the LUMO of the dopant [47]. This results in the formation of an anion (acceptor) and cation (host) i.e., the ion-pair. The formation of the ion-pair in molecular doped organic semiconductors has been observed and investigated primarily via spectroscopy due to the diagnostic ion absorption features observed in visible and IR regions [48-52].

In order to understand how mobile charge carriers, arise from the ion pair formation it is needed to know where the IPA levels are in energy in comparison to the levels of the surrounding organic semiconductors. As organic semiconductors respond to charging with bond-length changes and stabilization of the molecular orbitals, the second ionization energy is higher than the first and the electron affinity of a cation is higher than that of the neutral molecule [53]. Therefore, the occupied and unoccupied HOMO-derived sublevels of the cation split due to the consequence of the on-site Coulomb interaction which in turn originates from the energy difference between the electron affinity and the ionization energy of the cation. This is schematically shown for a p-type dopant in the Figure 2-7.

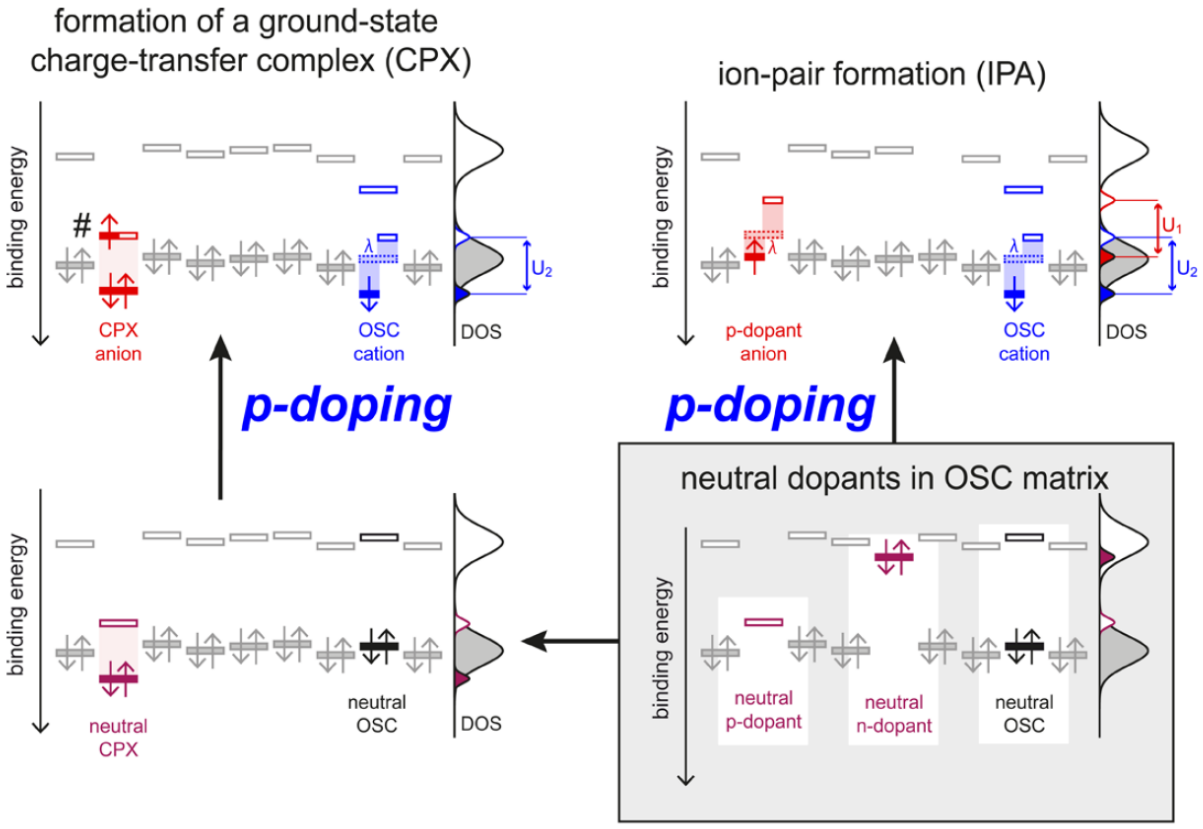

Figure 2-7 The schematic representation of the energy levels and the density of states due to p-type doping in both mechanisms of charge transfer complex (left) and ion pair formation (right) respectively. Reproduced with permission from [47].

2.8.2 Charge transfer complex formation

The mobile carrier density is also thought to originate from an alternate mechanism of the ground state charge transfer complex (CPX) formation [47]. The hybridization of the of the molecular orbitals of the dopant and the frontier molecular orbitals of the host lead to the formation of a new set of bonding and anti-bonding orbitals (occupied and empty respectively). For a Hückel-type host-dopant model, the energy of the occupied and empty hybrid orbitals of the charge-transfer complex is given by [47,54]:

$$E_{CPX,H/L} = \frac{H_{host} + L_{dopant}}{2} \pm \sqrt{(H_{host} + L_{dopant})^2 + 4\beta^2} \qquad (2.23)$$

It is important to note that the CPX is charge-neutral and the HOMO of the organic semiconductor and the LUMO of the dopant do not have to be in resonance, the hybridization can also take place when the LUMO of the dopant is higher or lower in energy to the HOMO of the host. This process therefore can also take place in cases where an ion-pair formation cannot occur. The CPX also exhibits absorption bands in spectroscopic investigations [54-55]. For a p-type dopant, usually the ionization energy of the CPX is higher and the electron affinity is lower than the ionization energy of the host. This results in the creation of a filled level above the host and an empty level below the transport level of the organic semiconductor. This is schematically depicted in Figure 2-7.

2.9 Conclusion

In this chapter, the most important concepts required for the understanding of the investigations presented in this thesis were discussed. This included topics ranging from linear combination of atomic orbitals in organic semiconductors, the device characteristics of organic light emitting diodes and field-effect transistors, the charge transport models used for investigation of the devices, the doping techniques, and the underlying doping mechanisms.

References

[1] A. Heinrichsdobler, J. C. Roigk, F. Schirmeier, C. J. Brabec, and T. Wehlus, Adv. Mater. Technol. **2**, 1700166 (2017).

[2] B. Lüssem, M. Riede, and K. Leo, Phys. Status Solidi A **210**, 9 (2013).

[3] N. Karl, *Organic semiconductors* (Springer Berlin Heidelberg, 1974).

[4] E. Hückel, Zeitschrift für Physik **70**, 204 (1931).

[5] Y. Sakamoto, T. Suzuki, M. Kobayashi, Y. Gao, Y. Fukai, Y. Inoue, F. Sato, and S. Tokito, J. Am. Chem. Soc. **126**, 8138 (2004).

[6] S.-J. Zou, Y. Shen, F.-M. Xie, J.-D. Chen, Y.-Q. Li, and J.-X. Tang, Mater. Chem. Front. **4**, 788 (2020).

[7] K. Myny, S. Steudel, S. Smout, P. Vicca, F. Furthner, B. van der Putten, A. Tripathi, G. Gelinck, J. Genoe, W. Dehaene, and P. Heremans, Org. Electron. **11**, 1176 (2010).

[8] J. S. Chang, A. F. Facchetti, and R. Reuss, IEEE J. Emerg. Sel. Topics Circuits Syst. **7**, 7 (2017).

[9] X. Wu, S. Mao, J. Chen, and J. Huang, Adv. Mater. **30**, 1705642 (2018).

[10] H. Kleemann, K. Krechan, A. Fischer, K. Leo, Adv. Funct. Mater. **30**, 1907113 (2020).

[11] C. Reese, Z. Bao, Adv. Funct. Mater. **19**, 763 (2009).

[12] B. K. Crone, P. S. Davids, I. H. Campbell, and D. L. Smith, J. Appl. Phys. **84**, 833 (1998).

[13] G. G. Malliaras, J. R. Salem, P. J. Brock, and C. Scott, Phys. Rev. B **58**, R13411 (1998).

[14] D. Joung, A. Chunder, L. Zhai, and S. I. Khondaker, Appl. Phys. Lett. **97**, 093105 (2010).

[15] J.-L. Bredas, Mater. Horiz. **1**, 17 (2014).

[16] A. Kahn, Mater. Horiz. **3**, 7 (2016).

[17] N. F. Mott, Can. J. Phys. **34**, 1356 (1956).

[18] A. Miller and E. Abrahams, Phys. Rev. **120**, 745 (1960).

[19] M. Van der Auweraer, F. C. De Schryver, P. M. Borsenberger, and H. Bässler, Adv. Mater. **6**, 199 (1994).

[20] P. W. M. Blom, M. J. M. de Jong, and M. G. van Munster, Phys. Rev. B **55**, R656 (1997).

[21] J. Frenkel, Phys. Rev. **54**, 647 (1938).

[22] H. Bässler, Phys. Status Solidi B **175**, 15 (1993).

[23] Y. Gartstein and E. Conwell, Chem. Phys. Lett. **245**, 351 (1995).

[24] D. H. Dunlap, P. E. Parris, and V. M. Kenkre, Phys. Rev. Lett. **77**, 542 (1996).

[25] S. V. Novikov, D. H. Dunlap, V. M. Kenkre, P. E. Parris, and A. V. Vannikov, Phys. Rev. Lett. **81**, 4472 (1998).

[26] R. Coehoorn, W. F. Pasveer, P. A. Bobbert, and M. A. J. Michels, Phys. Rev. B **72**, 155206 (2005).

[27] N. B. Kotadiya, H. Lu, A. Mondal, Y. Ie, D. Andrienko, P. W. Blom, and G.-J. A. Wetzelaer, Nat. Mater. **17**, 329 (2018).

[28] W. Pasveer, J. Cottaar, C. Tanase, R. Coehoorn, P. Bobbert, P. Blom, D. De Leeuw, and M. Michels, Phys. Rev. Lett. **94**, 206601 (2005).

[29] S. M. Sze, K. K. Ng, *Physics of Semiconductor Devices* (John Wiley & Sons, 2006).

[30] J. G. Simmons, Phys. Rev. Lett. **15**, 967 (1965).

[31] I. H. Campbell, P. S. Davids, D. L. Smith, N. N. Barashkov, and J. P. Ferraris, Appl. Phys. Lett. **72**, 1863 (1998).

[32] Y. Shen, A. R. Hosseini, M. H. Wong, and G. G. Malliaras, ChemPhysChem **5**, 16 (2004).

[33] G. Horowitz, A. Yassar, and H. von Bardeleben, Synth. Met. **62**, 245 (1994).

[34] C. K. Chiang, C. R. Fincher, Y. W. Park, A. J. Heeger, H. Shirakawa, E. J. Louis, S. C. Gau, A. G. MacDiarmid, Phys. Rev. Lett. **39**, 1098 (1977)

[35] Y. Yamamoto, K. Yoshino, Y. Inuishi, J. Phys. Soc. Japan 47, **1887** (1979)

[36] C. Kittel, *Introduction to Solid State Physics* (John Wiley & Sons, 2005).

[37] E. J. Meijer, C. Detcheverry, P. J. Baesjou, E. van Veenendaal, D. M. de Leeuw, and T. M. Klapwijk, J. Appl. Phys. **93**, 4831 (2003).

[38] G. Parthasarathy, C. Shen, A. Kahn, S. R. Forrest, J. Appl. Phys. **89**, 4986 (2001).

[39] B. Lüssem, C.-M. Keum, D. Kasemann, B. Naab, Z. Bao, K. Leo, Chem. Rev. **116**, 13714 (2016).

[40] I. Salzmann, G. Heimel, J. Electron Spectros. Relat. Phenomena **204**, 208 (2015).

[41] G. Heimel, I. Salzmann, N. Koch, AIP Conference Proceedings **1456**, 148 (2012)

[42] H. Kleemann, C. Schuenemann, A. A. Zakhidov, M. Riede, B. Lüssem, K. Leo, Org. Electron. **13**, 58 (2012).

[43] K.-H. Yim, G. L. Whiting, C. E. Murphy, J. J. M. Halls, J. H. Burroughes, R. H. Friend, J.-S. Kim, Adv. Mater. **20**, 3319 (2008).

[44] D. T. Duong, C. Wang, E. Antono, M. F. Toney, A. Salleo, Org. Electron. **14**, 1330 (2013).

[45] G. Sharma, S. Sangodkar, and M. Roy, Mater. Sci. Eng. B **41**, 222 (1996).

[46] K. Kanai, K. Akaike, K. Koyasu, K. Sakai, T. Nishi, Y. Kamizuru, T. Nishi, Y. Ouchi, and K. Seki, Appl. Phys. A **95**, 309 (2009).

[47] Ingo Salzmann, Georg Heimel, Martin Oehzelt, Stefanie Winkler, Norbert Koch, Acc. Chem. Res. **49** (3), 370 (2016).

[48] P. Pingel, D. Neher, Phys. Rev. B **87**, 115209 (2013)

[49] F. Ghani, A. Opitz, P. Pingel, G. Heimel, I. Salzmann, J. Frisch, D. Neher, A. Tsami, U. Scherf, N. Koch, J. Polym. Sci., Part B: Polym. Phys. **53**, 58 (2015).

[50] P. Pingel, L. Y.Zhu, K. S. Park, J. O. Vogel, S. Janietz, E. G. Kim, J. P. Rabe, J. L. Bredas, N. Koch, J. Phys. Chem. Lett. **1**, 2037 (2010).

[51] J. H. Lee, J. Lee, Y. H. Kim, C.Yun, B. Lussem, K. Leo, Org. Electron. **15**, 16 (2014).

[52] P. Pingel, D. Neher, Phys. Rev. B **87**, 115209 (2013).

[53] S. Winkler, P. Amsalem, J. Frisch, M. Oehzelt, G. Heimel, N. Koch, Mater. Horiz. **2**, 427 (2015).

[54] H. Méndez, G. Heimel, A. Opitz, K. Sauer, P. Barkowski, M. Oehzelt, J. Soeda, T. Okamoto, J. Takeya, J.-B. Arlin, J.-Y Balandier, Y. Geerts, N. Koch, I. Salzmann, Angew. Chem., Int. Ed. **52**, 7751 (2013).

[55] H. Méndez, G. Heimel, S. Winkler, J. Frisch, A. Opitz, K. Sauer, B. Wegner, M. Oehzelt, C. Röthel, S. Duhm, D. Többens, N. Koch, I. Salzmann, Nat. Commun. **6**, 8560 (2015).

Chapter 3

Experimental techniques

In this chapter, the materials used in this thesis will be introduced as well as the procedures, with which samples were prepared. Additionally, the experimental setups (the theory of which was described in Chapter 2), and data analysis methods will be described.

3.1 Materials and properties

Throughout the work in this thesis, a large number of host and dopant materials in various combinations were investigated. The chemical structures of the materials used as well as their properties are summarized in Figure 3-1 and Table 3-1 respectively [1-4].

Material	**HOMO**	**LUMO**
F4TCNQ	-8.34 eV	-5.24 eV
F6TCNNQ	-7.8 eV	-5.37 eV
α-NPD	-5.4 eV	-2.3 eV
Spiro-TAD	-5.4 eV	-2.4 eV
Spiro-OMeTAD	-5.1 eV	-1.8 eV

Table 3-1 The HOMO and LUMO energy levels of the materials used in this work

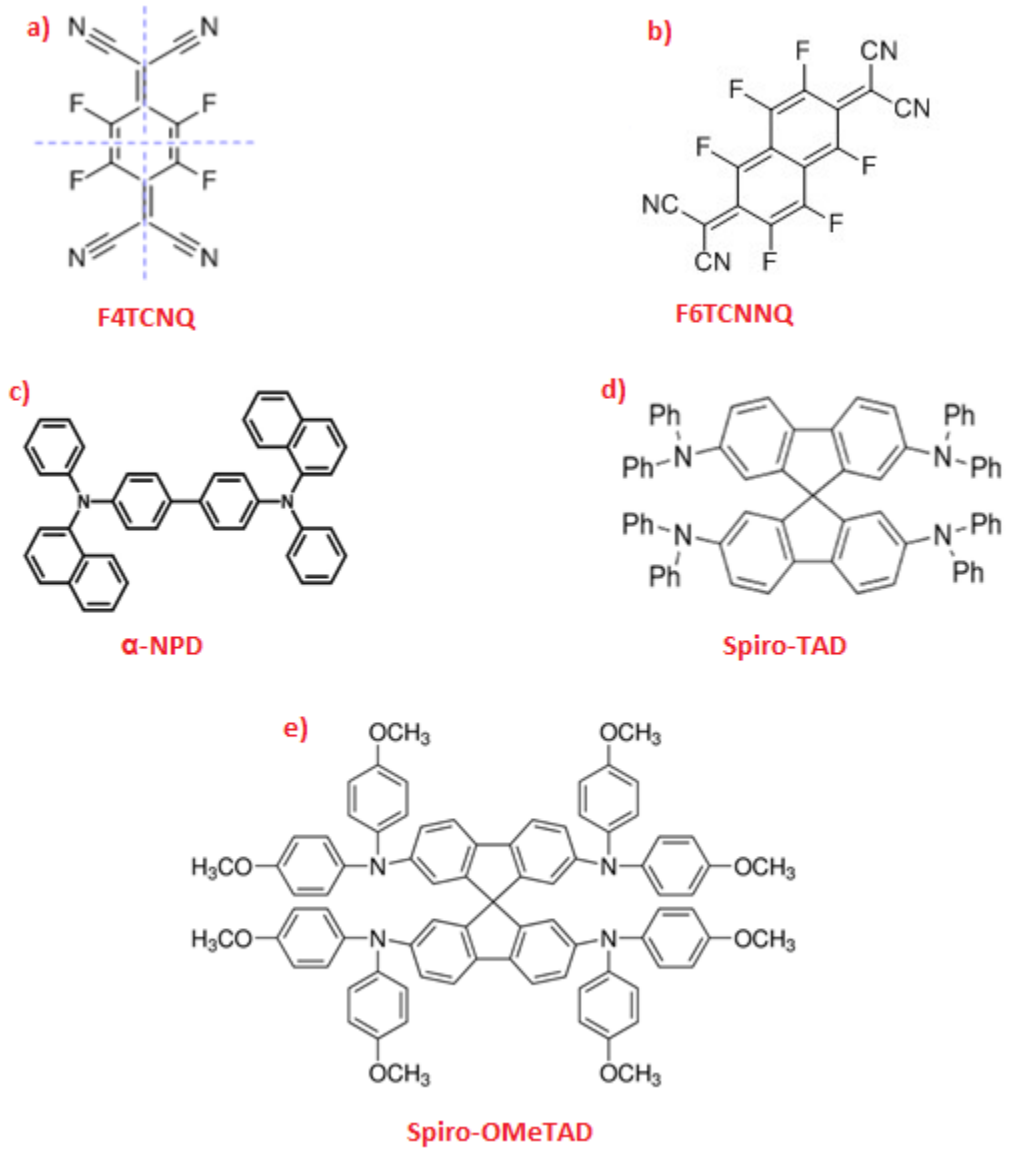

Figure 3-1 Chemical structures of a) F4TCNQ a p-type dopant b) F6TCNNQ a p-type dopant c) α-NPD a hole transporting small molecule d) Spiro-TAD a hole transporting small molecule e) Spiro-OMeTAD solution processable hole transporting material

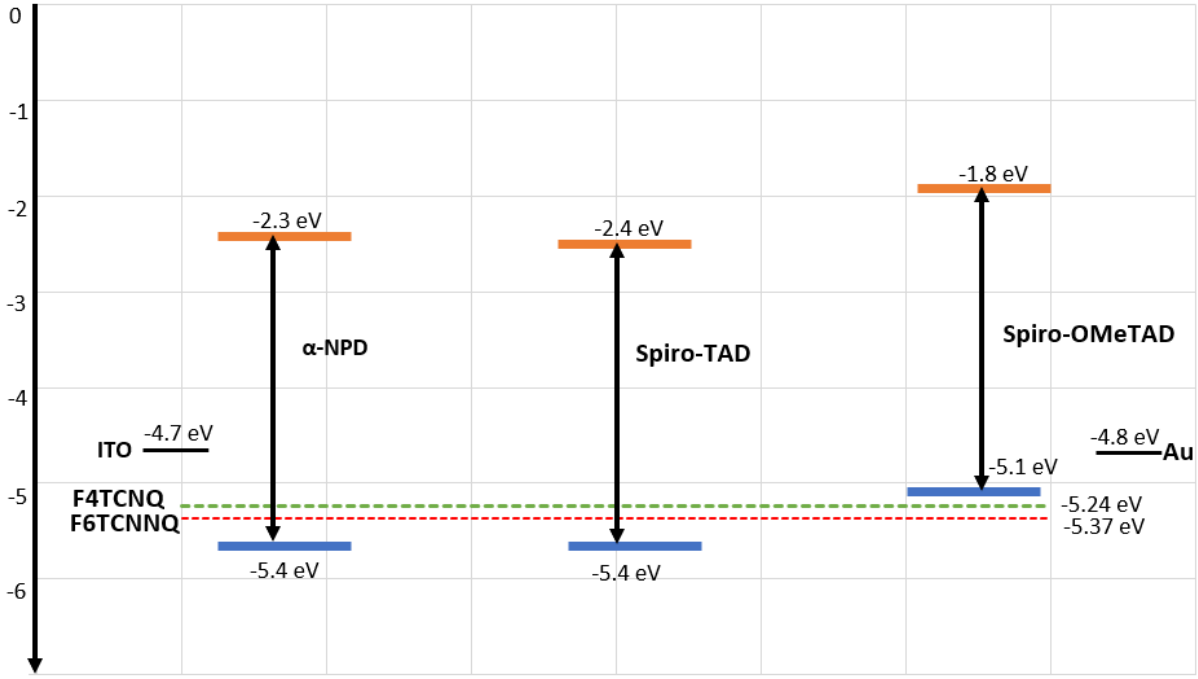

Figure 3-2 Energy level diagram of the materials used in this work

3.2 Thin film processing

The industry standard for thin film deposition and coating is through thermal evaporation in high vacuum. This usually results in high film uniformity, reproducibility, thickness control and multilayer deposition. However, this comes attached with drawbacks such as high setup cost, large material consumption and low throughput. In comparison, solution processing methods are more favorable for flexible substrates and offer low-cost manufacturing, reduced wastage of materials and high versatility.

But depending on the material characteristics and the solvents used, solution processed films might be difficult to control and have reproducibility issues. It is important to choose the best strategy in order to obtain the best performance. This section discusses in detail some of the methods used in the preparation of thin films characterized in this work.

3.2.1 Thermal evaporation

Thermal evaporation is a very widely used process for making thin film OLEDs of small molecules [5]. This allows multiple layers to be deposited with precise layer thickness control. There is also a possibility to make doped films by co-evaporating the host molecules together with the dopant molecules. The material to be deposited is placed in a small crucible and heated to a temperature such that it reaches a state of sublimation. A schematic representation of thermal evaporation is shown in Figure 3-3.

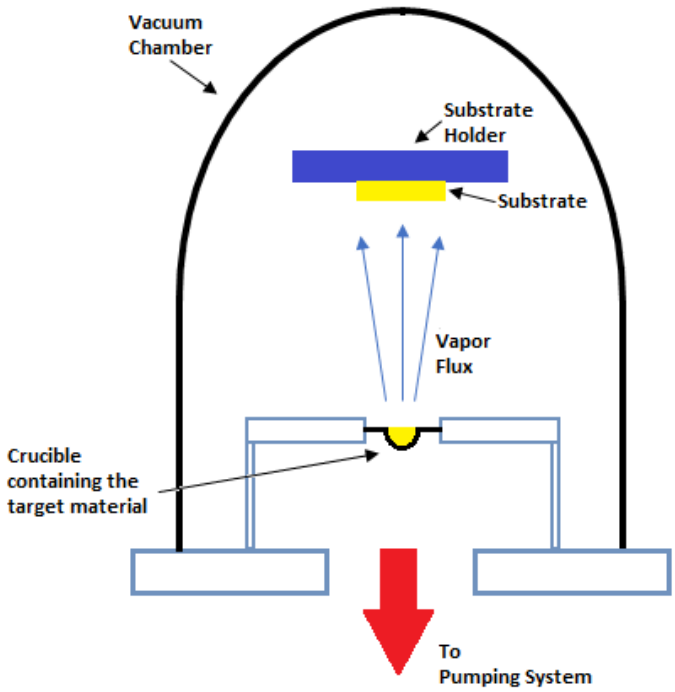

Figure 3-3 Schematic of a thermal evaporator used for vacuum deposition of small molecule based thin films

3.2.2 Spin coating

Spin coating is a very widely used low-cost solution processing technique to form thin films on top of substrates [6]. As shown in Figure 3-4 a predetermined amount of the desired material dispersed homogenously in the appropriate solvent is cast onto the substrate, which

is then rotated at high speeds causing the centrifugal force to spread the liquid over the entire substrate. The evaporation of the solvent leads to the formation of a solid film over the entire substrate. The thickness of the film can be adjusted by rotation speed, time of rotation and the solution concentration. The disadvantage of spin coating is that the area of the substrates is usually small (typically 5-300 mm), preventing upscaling (example: for 55 inch display) in an industrial process, and requires dispersion of a large amount of the solution, which is wasted during the rotation of the substrate. In this work, spin coating was carried out with a LabSpin6 TT from Suss MicroTec. In this a cleaned substrate such as glass or ITO patterned glass or silicon substrate is placed on to a chuck and held in place using vacuum. The required polymer or small molecule solution is dropped on to the center of the substrate and homogenously distributed by the rotation of the chuck. A typical process was the preparation of the α-NPD film with a thickness of about 100 nm. In the first step, a solution of 10 mg/ml (Chloroform) was dispersed, and the substrate was first rotated at 500 rounds per minute (rpm) for 10 seconds and then in the next step it was rotated for two minutes at 1500 rpm (film drying). The film thickness resulting from spin coating can be controlled by adjusting the polymer solution concentration and the rotation speed.

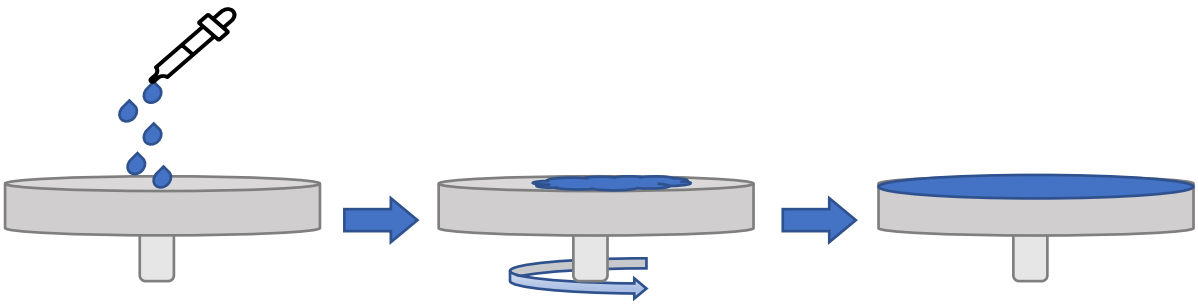

Figure 3-4: Schematic of spin-coating process

3.2.3 Wire-bar (Mayer rod) coating

This solution-coating method involves the usage of an automated wire-bar, which is moved over the substrate with constant speed resulting in spreading the solution uniformly over the substrate [7]. Before the movement of the rod, the solution is poured over the substrate in

front of the rod. There is a gap between the substrate and the wires of the rod, which enables the distribution of the solution over the substrate. The thickness of the resulting film is determined by the temperature of the plate, the applied speed of the wire-bar and the dimensions of the wire, which is wound around the bar. The substrate temperature can also be controlled which results in homogenous films formation with typically lower use of material. Mayer rod-coating is a well-established process in the coating industry [7] to obtain high quality films. Wire bar coating was performed with a K202 control coater (RK PrintCoat Instruments Ltd, UK). In this work, films of about 100 nm thickness were prepared by wire-bar coating. α-NPD was dissolved in chlorobenzene with a typical concentration of 15 mg dissolved in 1 ml of the solvent. Proper dissolution occurred at 80 °C under vigorous stirring (magnetic stirrer). The cleaned substrate is put onto the heated plate and fixed with two sacrificial glass slides on either side. The wire-bar starts its movement on top of the first adjacent glass slides, then moves over the actual substrate, and stops on top of the second adjacent glass slide after the substrate. This has been depicted schematically in Figure 3-5. Using these two sacrificial glass slides, the solution can be homogeneously distributed over the entire sample.

3.2.4 Drop-casting

In Figure 3-6 it can be seen that, by dropping the solution on to the substrate, after which the solvent is allowed to evaporate, a thin film is formed. The thickness of the resulting film is controlled by varying the viscosity of the solution [8]. The films are very easy to process, and it also allows for large substrates to be processed, however the thin film coating is usually non-uniform and there is typically a coffee-ring effect.

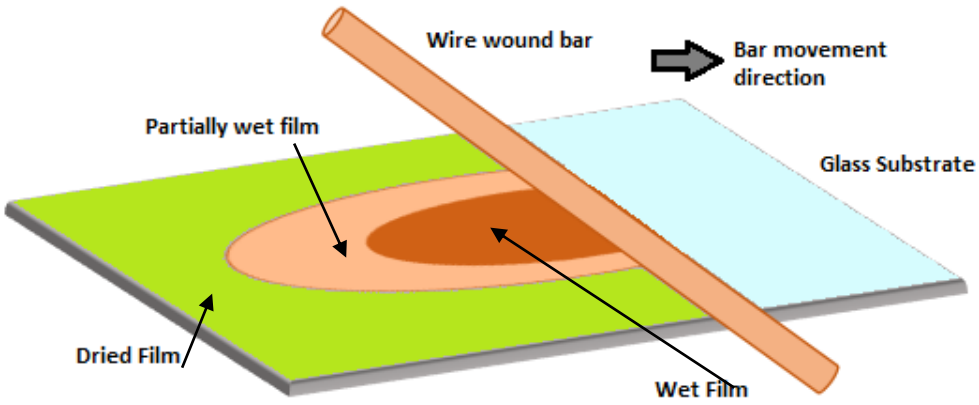

Figure 3-5 Schematic of the wire bar coating process to create thin films

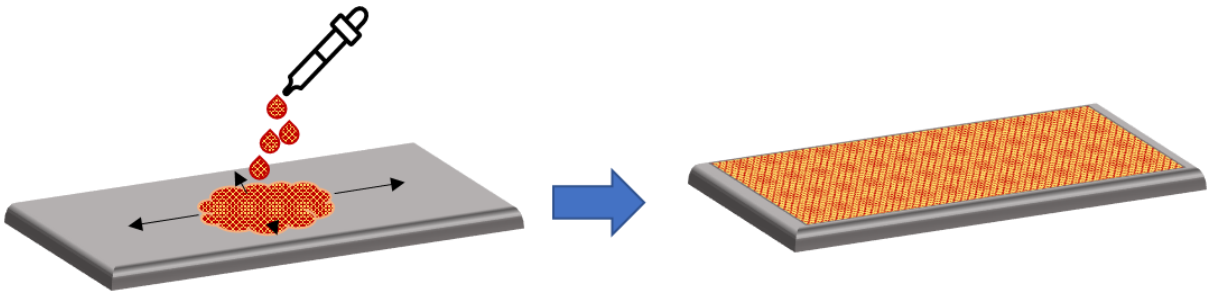

Figure 3-6: Schematic of drop casting of solution processable materials to create thin films on substrates

3.2.5 Dip coating

Deposition of a film obtained by immersion and withdrawal of a substrate into a solution is generally indicated as dip coating (Figure 3-7). The coating thickness is controlled by the withdrawal speed, concentration of the solution, viscosity, and boiling point of the solvent. Dip-coating is a cheap and simple method with no waste of raw material [9]. However,

double-side coating of bare substrates is unavoidable and uniform film formation is restricted to viscous solutions.

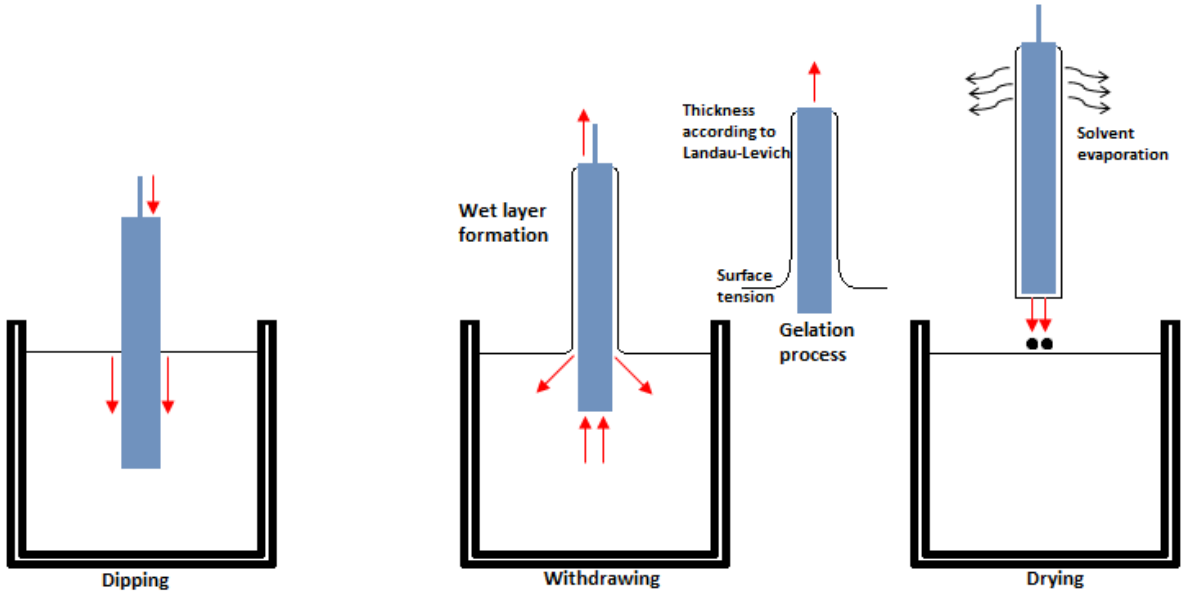

Figure 3-7 Dip coating steps used in thin film processing.

3.3 Sample preparation

The devices used for all the measurements in this thesis were prepared under inert atmosphere or under vacuum. For solution processed molecules and polymers, a nitrogen filled glovebox was used where the water and oxygen levels were less than 1 ppm. Chloroform (CF), chlorobenzene (CB) and toluene (Tol) were procured from Sigma Aldrich GmbH (>99.9% purity, inhibitor-free) and the stock solutions were prepared only using dry and degassed solvents i.e., further degassing was performed by pump thaw freezing before usage. The host and dopant materials used were handled only in the nitrogen filled gloveboxes, where they were weighed and then dissolved in appropriate amounts dependent on the thickness desired. The stock solutions were stirred and used immediately. Especially for doped devices, solutions were always prepared from the stock solutions directly before deposition of thin films. About 25-75 µl was dropped onto the cleaned ITO patterned glass

substrates covered with 100 nm of PEDOT:PSS and spin coated at various speeds and times to achieve the desired thickness.

The thermal evaporation was performed in vacuum systems with base pressures less than 10^{-8} mbar. The small molecule was loaded into quartz crucibles surrounded by tantalum wires and heated by the current flow resistively. The crucibles were loaded into the vacuum chamber together with the pre-cleaned substrates and then pumped down to pressures below 10^{-8} mbar. By heating the crucible above the sublimation temperature of the materials, the small molecules were sublimed. The thickness was controlled by using a quartz crystal microbalance and a steady rate (5 Å/min) was obtained before the shutter was opened for the actual deposition.

3.4 Device working principle

In order to clearly understand the charge transport in a semiconductor thin film, it is necessary to disentangle the effects of electrons and holes. This is achieved using hole-only and electron-only devices. In an OLED, the work functions of the anode and cathode match the energy levels of the HOMO and LUMO respectively. The energy diagram is shown in Figure 3-8. ITO covered PEDOT:PSS layer is used as anode and hole-injection layer respectively and barium with an aluminum capping layer is the cathode.

In a hole-only device, the injection of electrons must be blocked. There two hole-injecting contacts are used. The energy diagram is shown in Figure 3-9. For the bottom contact ITO with a PEDOT:PSS layer is used and thermally evaporated MoO_3 is used as a top-hole injecting contact. For an electron-only device, the hole injection at the electrodes need to be blocked. The ITO is replaced with an oxidized aluminum contact which has a work function of around 3.1eV below vacuum and prevents hole injection. Electron-injecting barium with an aluminum capping layer is then used as a top contact.

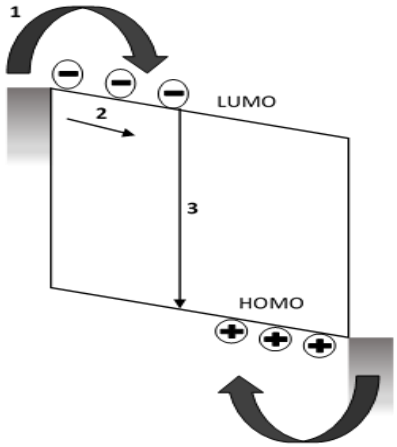

Figure 3-8 Schematic overview of the three dominant processes during OLED operation: 1) injection, 2) transport and 3) recombination

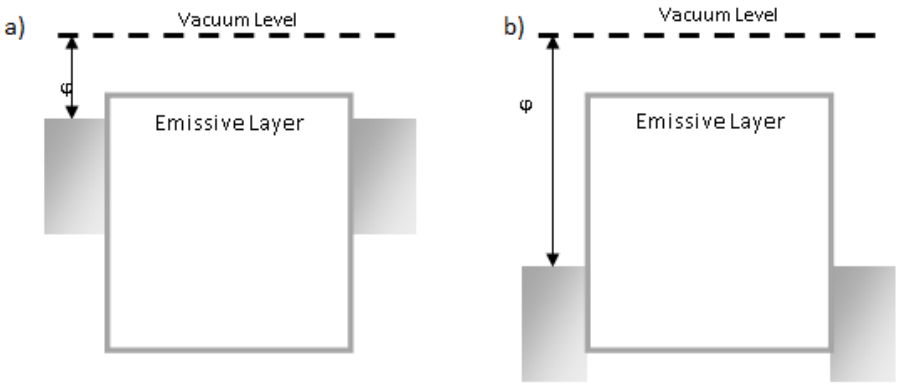

Figure 3-9: Schematic energy diagram of a single charge carrier device: a) electron only device with two low work function electrodes and b) hole only device with two high work function electrodes

3.5 Device characterization

The charge transport in organic semiconductors is characterized by analyzing the current-voltage characteristics (I-V) of both single carrier and double carrier devices. In this thesis, the devices were prepared as described in the previous section and then measured using a Keithley 2400 source meter. The light output of a PLED is measured using a silicon

photodiode that is connected to a Keithley 6514 electrometer. To measure the luminance (L), a Konica Minolta LS-100 luminance meter was used. The Electroluminescence spectrum is measured with an Ocean Optics USB400-UV-Vis-ES spectrometer.

In order to measure the current density -voltage (J-V) characteristics of a PLED, a voltage sweep is applied typically from 0 to 6V with a step size of 0.1V. At 6V, the voltage is swept back to -2V and subsequently increased back to 0 V. A J-V curve of a typical Spiro-TAD LED is shown in solid lines in black in Figure 3-12. In reverse bias the leakage current of the device is obtained which is also observed at very low voltage in forward bias. The device current at low voltages is primarily dominated by the leakage and it scales linearly with the applied voltage. Above 3 V, the current follows an exponential increase. Due to the different work functions of the electrodes, a built-in voltage exists across the device, which gives rise to an internal electric field at 0 V. When the voltage applied is lower than the built-in voltage, the electric field is in the opposite direction to the current flow, and therefore the measured current is dominated by a diffusion current. In this case the current density is exponentially dependent on the voltage applied [10]. At voltages above the built-in voltage, the electric field changes sign, resulting in a drift current. In the case of a space-charge-limited drift current, the current density is quadratically dependent on the voltage.

In symmetric hole-only devices, hole injection is possible from both contacts depending on the sign of the applied voltage, resulting in a hole current present in both forward and reverse bias. In this case, the voltage is swept from 0 to 5 V and -5 to 0V. This is shown in Figure 3-10. For the curve to be symmetric, both the contacts must be Ohmic. The analysis of charge transport from J-V characteristics requires knowledge of the film thickness. Therefore, there is a need to measure and control the thickness of the film of every device. A Bruker DektakXT Stylus Profiler was used to measure the film thickness. The thin film is scratched with a needle, exposing the glass substrate underneath. The surface profiler is then used to measure the height difference between the thin film and the glass surface.

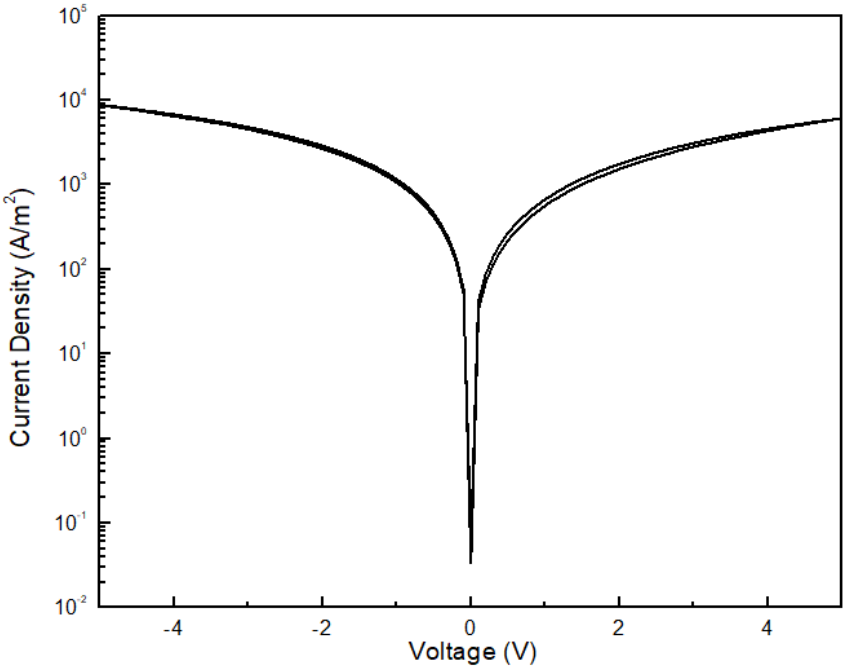

Figure 3-10 Hole current measurement of a Spiro-TAD hole only device

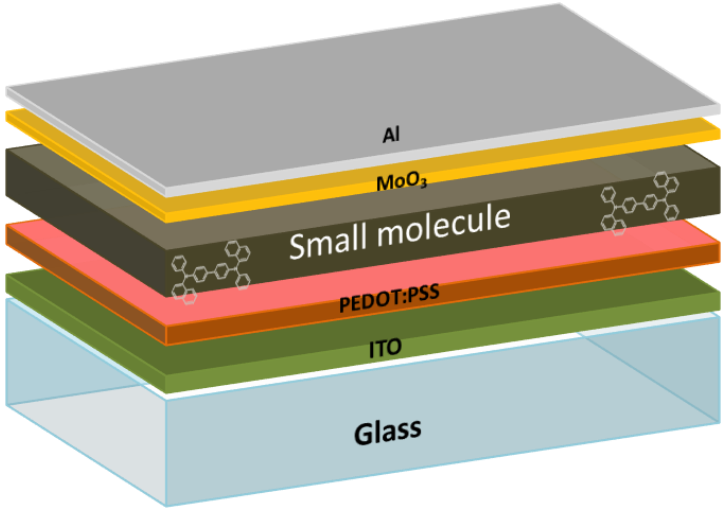

Figure 3-11 Schematic of a typical hole only structure used to measure single carrier charge transport in this work

3.6 Atomic force microscopy

Atomic force microscopy (AFM) was carried out with a Nanoscope Dimension 3100 (Bruker) and with Si tips and Al backside coating in tapping mode.

In an AFM measurement, the surface of a sample is scanned with a tip mounted to the cantilever. The tip can either be in contact with the surface or slightly above the surface which is called the non-contact mode. Tapping mode is a special case of non-contact mode where the cantilever is further vibrated using an actuator. The cantilever oscillates close to its resonance frequency.

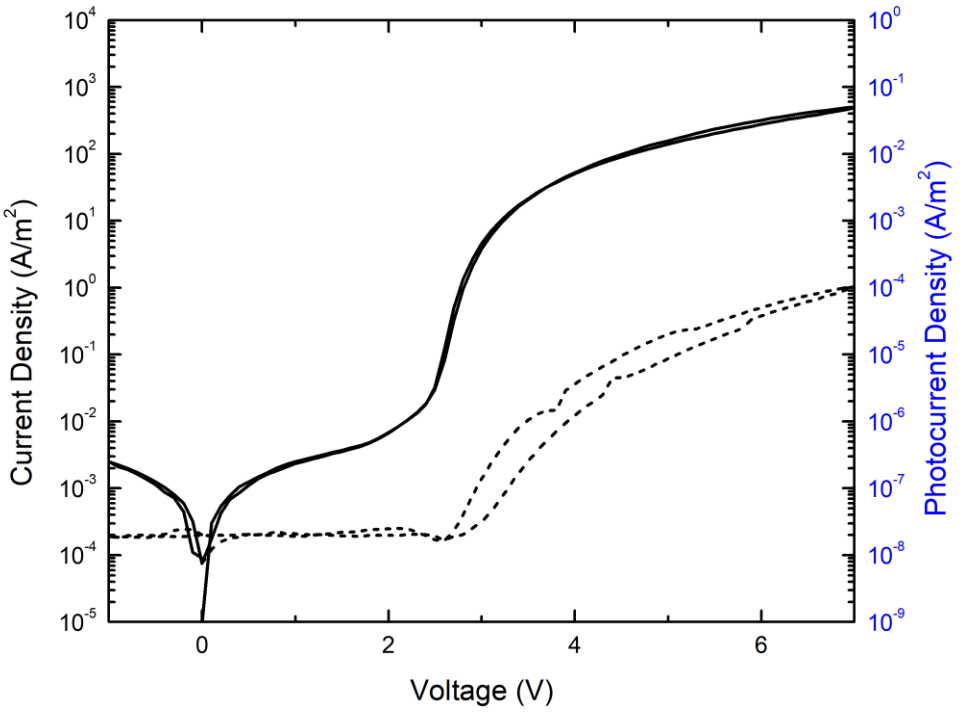

Figure 3-12 Charge transport measurements of a single-layer OLEDs with Spiro-TAD (300 nm). Solid lines show the J-V characteristics and dotted lines show the photocurrent density.

When in contact with the surface, the free oscillation of the cantilever gets damped and the amplitude of oscillation is decreased. The cantilever had a force constant 26 N/m and the resonance frequency was around 270 kHz. A scan frequency of 0.5 Hz was applied which means that one line was scanned back and forth within two seconds. In this work, the measurements were performed in constant amplitude oscillation. To keep the amplitude constant during the surface scan, the feedback loop moves the cantilever up or down by means of a piezoelectric element. The signal for the feedback is given by a laser which is focused onto the cantilever such that the reflected beam hits a photodiode sensor. The change in the height position which is used by the piezoelectric element as a corrective measure for the amplitude of the cantilever results in the desired height signal of the measurement.

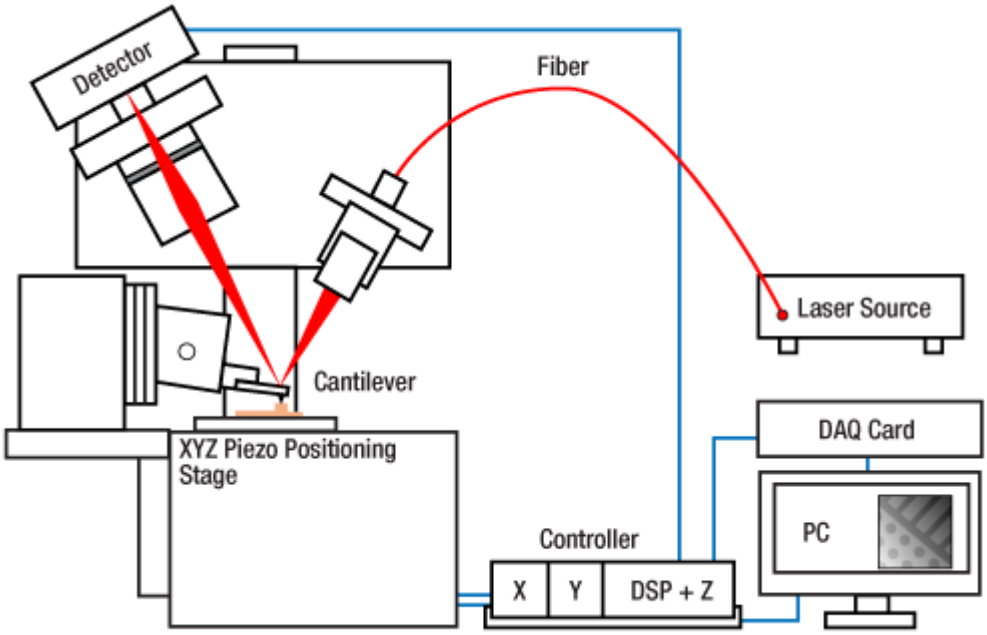

Figure 3-13 Schematic representation of an AFM (Thorlabs)

The three-dimensional (3D) data were processed using the software Gwyddion. The pictures are shown as 2D images, where x- and y position define the probed area. The height is color-coded (see Figure 4-6 and Figure 4-7).

References

[1] S. Olthof, W. Tress, R. Meerheim, B. Lüssem, and K. Leo, J. Appl. Phys. **106**, 103711 (2009).

[2] I. E. Jacobs and A. J. Moulé, Adv. Mater. **29**, 1703063 (2017).

[3] J. Li, I. Duchemin, O. M. Roscioni, P. Friederich, M. Anderson, E. Da Como, G.Kociok-Köhn, W. Wenzel, C. Zannoni, D. Beljonne, X. Blase, and G. D'Avino, Mater. Horiz. **6**, 107 (2019).

[4] Shahnawaz, S. Sudheendran Swayamprabha, M. R. Nagar, R. A. K. Yadav, S. Gull, D. K. Dubey, and J.-H. Jou, J. Mater. Chem. C **7**, 7144 (2019).

[5] J. P. Spindler, J. W. Hamer, and M. E. Kondakova, "OLED manufacturing equipment and methods", in *Handbook of advanced lighting technology*, edited by R. Karlicek, C.-C. Sun, G. Zissis, and R. Ma (Springer International Publishing, 2017), pp. 417–441.

[6] N. Sahu, B. Parija, S. Panigrahi, Indian J Phys **83**, 493 (2009)

[7] M. Pandey, N. Kumari, S. Nagamatsu, and S. S. Pandey, J. Mater. Chem. C **7**, 13323 (2019).

[8] B. H. Lee, S. H. Park, H. Back, and K. Lee, Adv. Funct. Mater. **21**, 487 (2011).

[9] G. P. Rigas and M. Shkunov, Polym. Sci. Ser. C **56**, 20 (2014).

[10] P. de Bruyn, A. H. P. van Rest, G. A. H. Wetzelaer, D. M. de Leeuw, and P. W. M. Blom, Phys. Rev. Lett. **111**, 186801 (2013)

Chapter 4

Charge transport in undoped small molecules

This chapter[2] presents a study of charge transport in the amorphous organic small molecules α-NPD (N,N-di(1-naphthyl)-N,N-diphenyl-(1,1-biphenyl)-4,4-diamine) and SpiroTAD (2,2,7,7-tetrakis(N,N-diphenylamino)-9,9-spirobifluorene)). Charge transport is investigated in solution-processed films and compared to charge transport in vacuum-deposited films of the same molecule. By optimizing the deposition conditions, such as solvent and concentration, equal charge-transport parameters for solution-processed and vacuum-deposited films are demonstrated. Modelling of the charge carrier transport characteristics was performed by drift-diffusion simulations. The dependence of the charge carrier mobility on temperature, carrier density and electric field was found to be the same for vacuum deposition and solution processing. In both material processing cases, hole mobilities of 4×10^{-8} $m^2V^{-1}s^{-1}$ for Spiro-TAD and 0.8×10^{-8} $m^2V^{-1}s^{-1}$ for α-NPD is obtained, demonstrating that solution processing can be a viable alternative to vacuum deposition in terms of charge transport.

4.1 Introduction

The field of display technology and lighting in the last decade has been revolutionized by the discovery of organic light-emitting diodes (OLEDs) based on π-conjugated organic semiconductors [1, 2]. In addition, small-molecular organic semiconductors are widely used

[2] The content of this chapter has been adapted from: D. K. Mangalore et al., APL Mater. **7**, 011105 (2019)

in charge-transport layers in perovskite photovoltaic devices [3]. The opportunity presented by these technologies has driven the research to find cheaper alternatives to the traditional deposition method of layers of organic small molecules by thermal evaporation in high vacuum. The solubility of organic semiconductors in organic solvents renders them suitable for film deposition from solution, which can be scaled up to a cost-effective roll-to-roll process [1, 2]. However, it is unclear whether solution-processed films of organic semiconductors can maintain the same film quality and charge-transport characteristics as compared to vacuum-deposited films. Usually, to obtain solution processability, the chemical structure of organic molecules is modified, typically by adding solubilizing side chains to the conjugated moiety [4, 5]. However, these insulating sidechains also affect the charge-transport properties, complicating a direct comparison with their vacuum-deposited counterparts.

Solution-processed small-molecular charge-transport layers in OLEDs have been reported as early as two decades ago [6]. More recently, efforts have been made to systematically replace vacuum-deposited transport- and emitting-layers in OLED stacks by solution processed layers and investigating their effect on the OLED performance [7–9]. To compare the charge-transport characteristics of individual layers of solution- and vacuum-deposited small molecules, single-carrier devices have been investigated [7, 8]. Dissimilar current-voltage characteristics were obtained, possibly affected by the presence of a variation in injection barrier [7]. While morphological differences have been investigated in films of spin-coated and vacuum-deposited amorphous small molecules [10], a detailed analysis and comparison of the charge-transport properties of solution- and vacuum-deposited films of organic small molecules has not been reported to date. Additionally, the modelling of the transport characteristics from different processing conditions has not been investigated.

In this chapter, we investigate the hole transport in solution-processed and vacuum-deposited films of the commonly used amorphous hole-transport molecules α-NPD and Spiro-TAD by space-charge-limited current measurements in single-carrier devices with Ohmic hole contacts and verify it by numerical modelling. After optimizing the solution process, smooth

and uniform films with near identical charge-transport properties are obtained as compared to vacuum-deposited films of the same molecule.

4.2 Sample fabrication and characterization

The two investigated hole-transport materials, Spiro-TAD and α-NPD (both sublimed grade) were purchased from Luminescence Technology Corp. and Sigma-Aldrich, respectively, and used as received. The hole-only devices were fabricated in sandwich geometry consisting of a bottom electrode, a small molecule thin film and a top electrode [11, 12]. Glass substrates pre-patterned with indium-tin oxide were first cleaned with neutral soap and then rinsed with deionized water, followed by sonication in acetone and isopropanol, and UV-ozone treatment. Next, a 55 nm thick film of poly(3,4-ethylenedioxythiophene): polystyrene sulfonate (PEDOT:PSS; Clevios P VP Al4083, Heraeus) was spin-coated from an aqueous dispersion and then annealed at 140 °C for 10 minutes in air. Subsequently, organic thin films of α-NPD or Spiro-TAD were deposited by either spin coating or conventional vacuum-deposition. For spin coating, solutions of different concentrations in chloroform, chlorobenzene or toluene were spin cast in nitrogen atmosphere, followed by annealing for 10 min at 50 °C. Alternatively, vacuum deposition was carried out at a deposition rate of 1-2 Å/s at a base pressure of 1×10^{-7} mbar. For Ohmic-contact formation, a 5 nm layer of tris(4-carbazoyl-9-ylphenyl)amine (TCTA) was vacuum-deposited between the hole-transport layer and the vacuum-deposited MoO_3(10 nm)/Al(100 nm) top electrode [13].The current density-voltage (J-V) characteristics were recorded with a Keithley 2400 source meter. All measurements were carried out in nitrogen atmosphere. The thickness of the films was measured using a Bruker Dektak XT Profilometer. In the solution process, Spiro-TAD was deposited using three different solvents.

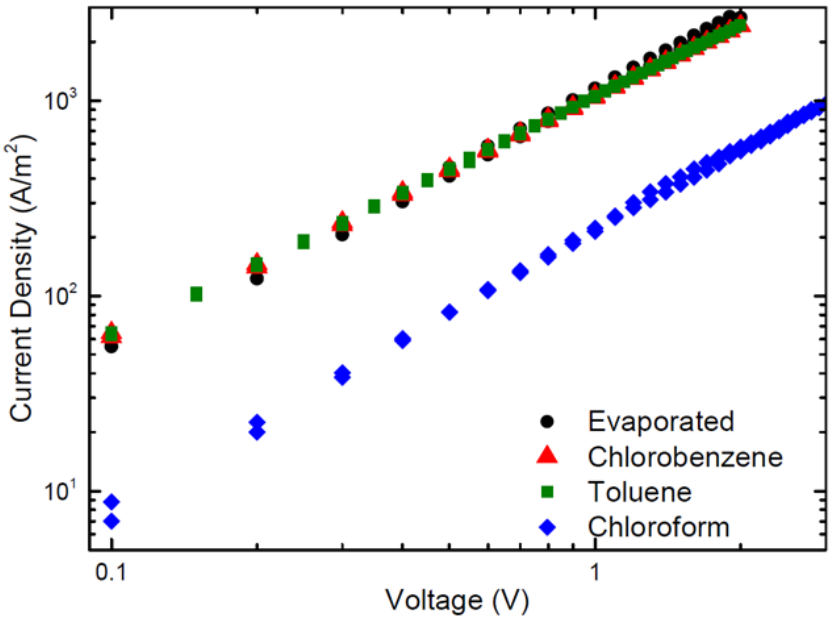

Figure 4-1: Experimental current density-voltage characteristics of hole-only devices with a Spiro-TAD layer thickness of 100 nm. The solution-processed films spin-cast from chlorobenzene (red triangles), toluene (green squares), or chloroform (blue diamonds) are compared to a thermally evaporated (black circles) reference device.

4.3 Results and Discussion

The current density-voltage characteristics of the hole-only devices were then compared to a thermally evaporated control device, as shown in Figure 4-1. Similar current densities to the control device were obtained for the solution-processed films when using chlorobenzene or toluene as a solvent. As the current density scales directly with the hole mobility in a space charge-limited device, the almost identical J-V characteristics indicate that hole transport in these solution-processed films is equal to the hole transport in the vacuum-deposited film. On the other hand, the current in the chloroform-processed Spiro-TAD device is a factor of 4 lower, showing that the used solvent can influence the hole transport. A more prominent effect of the solvent is observed for α-NPD. α-NPD was found to be less soluble and more difficult to process from solution. However, for chlorobenzene-processed films, the measured

hole current was found to approach the current of the vacuum-deposited control device, as shown in Figure 4-2.

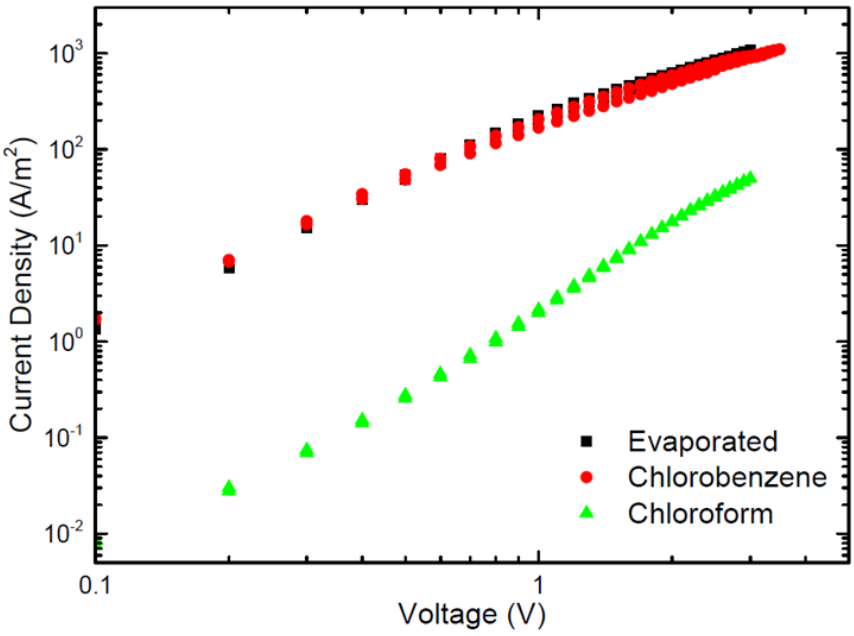

Figure 4-2: Experimental current density-voltage characteristics of hole-only devices with an α-NPD layer with a thickness of 100 nm. Thermally evaporated devices (black squares) are compared to solution-cast films from different solvents: chloroform (green triangles) and chlorobenzene (red dots).

The results above demonstrate that solution-processed films of Spiro-TAD and α-NPD can have similar hole transport to their vacuum-deposited counterparts at room temperature.

To investigate the charge transport in more detail, temperature-dependent J-V characteristics were measured, which were modelled with one-dimensional drift-diffusion simulations [14], from which the hole mobilities were evaluated. The charge-carrier mobility in disordered organic semiconductors is dependent on temperature, charge-carrier density and electric field [14, 15]. For hopping transport between states having a Gaussian distribution in energy, the mobility has been described by the extended Gaussian disorder model (EGDM) [14].

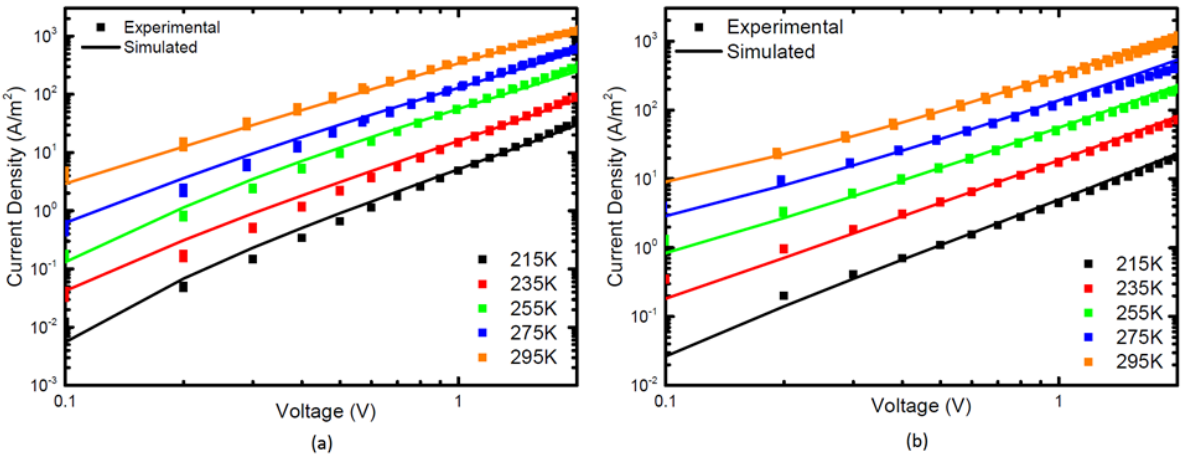

Figure 4-3: Temperature-dependent experimental (symbols) and simulated (lines) current density voltage characteristics of Spiro-TAD hole-only devices with a layer thickness of 180 nm, solution-processed from toluene (a) and vacuum-deposited (b).

In this model, the charge transport is characterized by the width of the density-of-states distribution σ, the lattice constant a and a mobility prefactor μ_∞. With increasing energetic disorder, the mobility becomes increasingly dependent on temperature, according to [14]

$$\mu_0(T) = \mu_\infty c_1 \exp\left[-c_2 \left(\frac{\sigma}{kT}\right)^2\right] \tag{4.1}$$

where $c_1 = 1.8 \times 10^{-9}$ and $c_2 = 0.42$ are given by the EDGM, k is the Boltzmann constant and T is the temperature. Here, $\mu_0(T)$ denotes the temperature-dependent mobility in the limit of vanishing carrier density and electric field. Apart from the influence of σ on the temperature dependence, also the density dependence of the mobility becomes stronger for increased energetic disorder.

The lattice constant a mostly influences the field dependence of the mobility, with a stronger field dependence for larger lattice constants. The constants c_1 and c_2 are obtained in Ref. [14] from the parametrization of the solution of the Master equation for hopping transport on a cubic lattice of sites with Gaussian distribution of energy. Even though these constants are obtained for a lattice model, it has been shown that for simulated morphologies of α-NPD a constant $c_2 = 0.41$ is obtained, very similar to the constant in the EGDM, justifying its applicability [16]. The constant c_1 can be included in the mobility prefactor. The mobility prefactor μ_∞ is a temperature-independent parameter that only influences the magnitude of the mobility and is used as a fit parameter, next to the density of states distribution and the lattice constant.

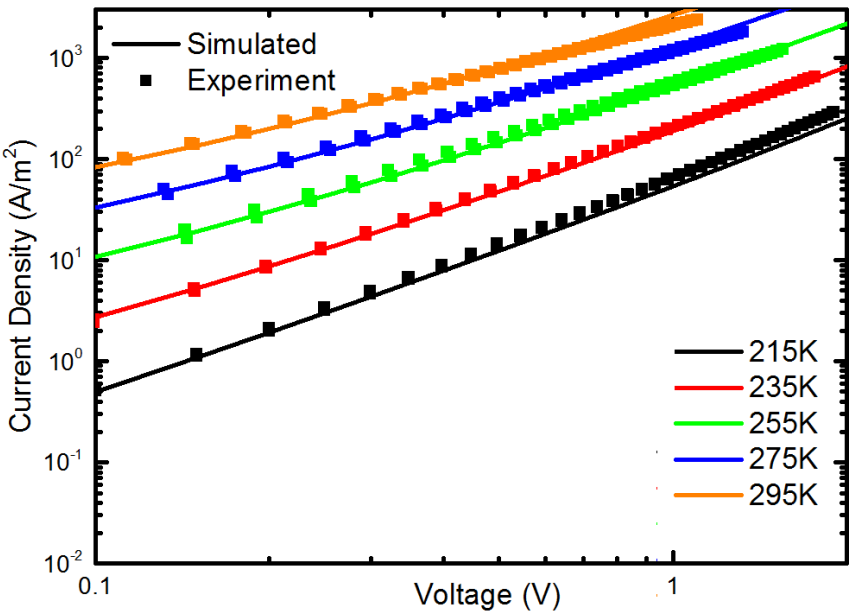

Figure 4-4: Temperature-dependent experimental (symbols) and simulated (lines) current density voltage characteristics of Spiro-TAD hole-only devices with a layer thickness of 100 nm, solution-processed from toluene

The experimental temperature-dependent J-V characteristics were modelled with drift diffusion simulations incorporating the EGDM mobility function, as displayed in Figure 4-3. The experimental data can be consistently described for both solution-processed and

thermally evaporated films, with the same set of parameters. We find that the energetic disorder is 0.09 eV in both thermally evaporated and optimized solution processed devices. The used lattice constant was 1.1 nm in both cases. The mobility at 295 K at zero electric field and carrier density was found to be 4 $\times 10^{-8}$ $m^2V^{-1}s^{-1}$ for both solution- and vacuum-deposited films. This value is also consistent with time-of-flight measurements on thermally evaporated Spiro-TAD [17]. The temperature dependent *J-V* measurements of a hole-only device with a different Spiro-TAD thickness (100 nm) can also be modeled with the same parameters and fits with the EGDM (see Figure 4-4). The results from the two different thicknesses show that equal mobilities can be obtained irrespective of the device thickness.

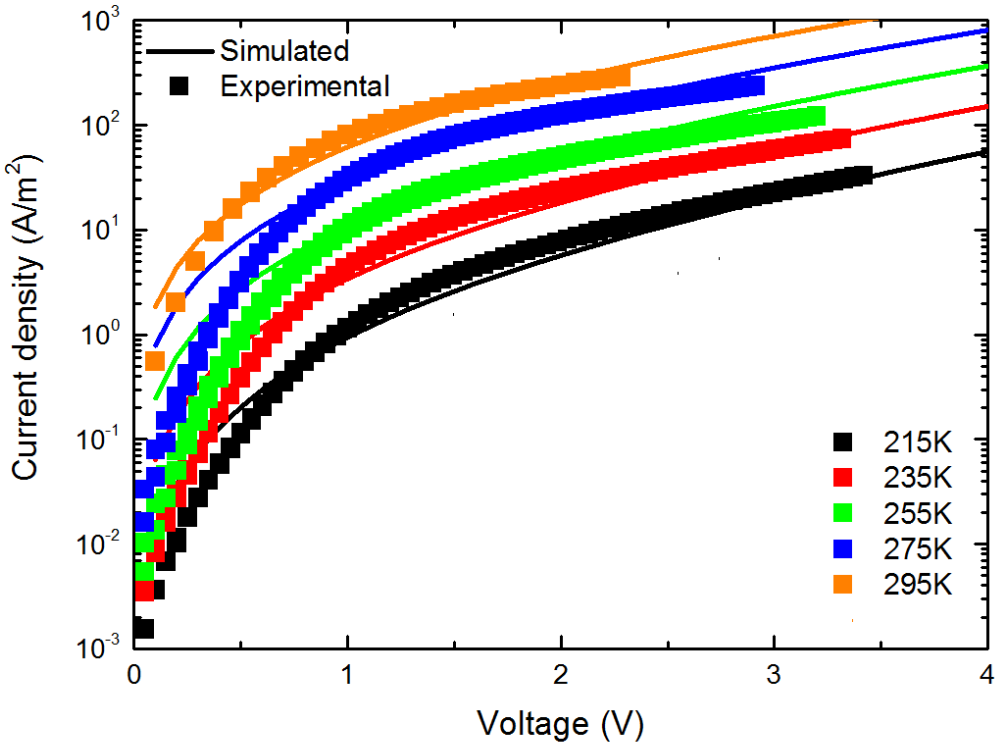

Figure 4-5: Temperature-dependent experimental (symbols) and simulated (lines) current density voltage characteristics of Spiro-TAD hole-only devices with a layer thickness of 98 nm, solution-processed from chloroform

For α-NPD, the hole mobility in the chlorobenzene-processed film amounted to 0.9 $\times 10^{-8}$ $m^2V^{-1}s^{-1}$, approaching the value for the vacuum-deposited reference. The energetic disorder was found to be 0.09 eV in both cases, similar to previously reported values [11,16]. The similar mobility and disorder values obtained for solution-processed and vacuum-deposited films of α-NPD and Spiro-TAD show that charge transport can be equally good for both deposition methods. The lower mobility in chloroform-cast films may arise from increased energetic disorder in these films. This hypothesis is supported by the increased temperature dependence of the J-V characteristics in chloroform-cast films compared to toluene-cast films (see Figure 4-5). When modeled using the EGDM, we find that the disorder parameter in chloroform-cast films is 0.12 eV, which is larger than the energetic disorder obtained for toluene-cast and vacuum-deposited films (0.09 eV).

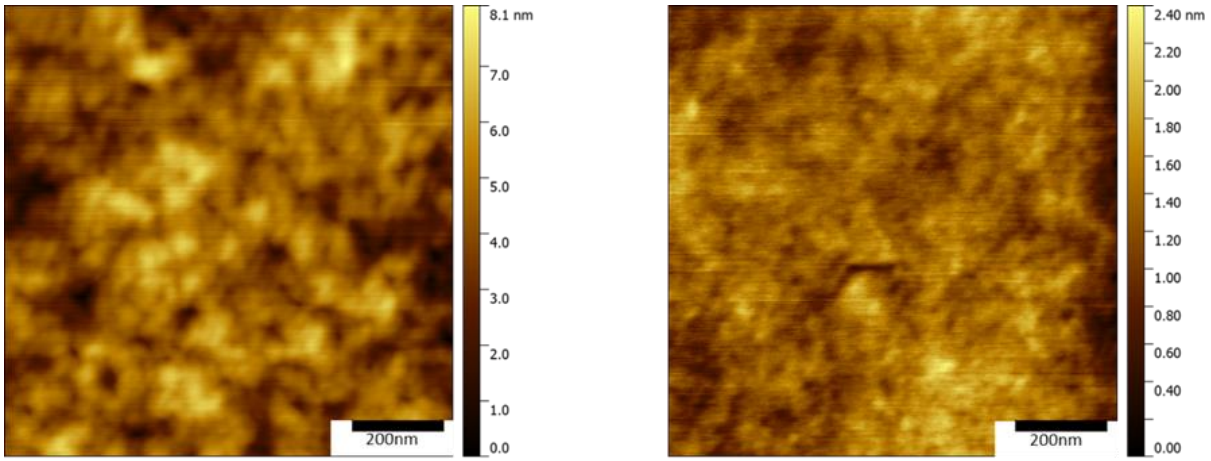

Figure 4-6: AFM topography (scale bar 200 nm) of vacuum-deposited Spiro-TAD films (a) and spin-cast from toluene solution (b). The measurement area size used is 1 × 1 μm^2.

In order to compare the surface morphology, spin-coated and vacuum-deposited films thin films were prepared on glass-ITO substrates. The spin cast films were deposited in a nitrogen atmosphere from solutions of Spiro-TAD in chlorobenzene and toluene. Figure 4-6 shows the atomic-force microscopy (AFM) images of the vacuum-deposited and spin-coated thin films of Spiro-TAD on the ITO substrates. The root mean square (RMS) roughness values of the

surface of films obtained by thermal evaporation, chlorobenzene deposition, and toluene deposition were 8.1 nm, 2.4 nm, and 2.1 nm, respectively. Hence, the spin-coated Spiro-TAD films are even smoother in comparison to the thermally-evaporated films. For α-NPD, the RMS roughness was determined to be 2.8 nm for the thermally evaporated film and 2.4 nm for the chlorobenzene-cast film as shown in Figure 4-7. The chloroform-cast film had an RMS roughness of 7.7 nm. As expected for amorphous materials, the AFM topography images do not show any distinct features.

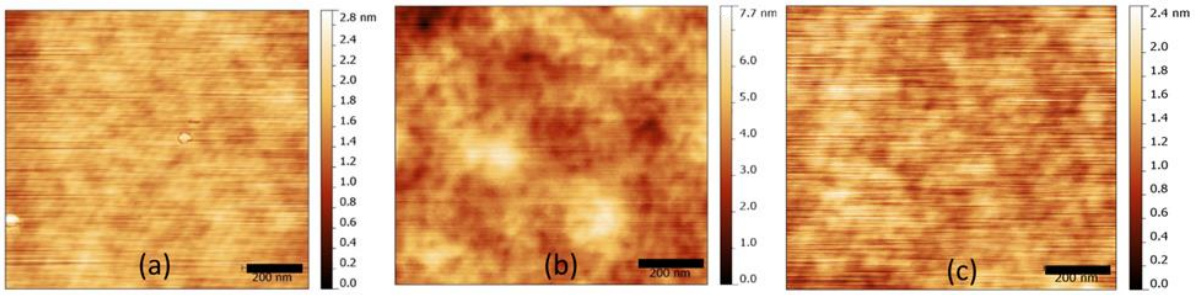

Figure 4-7: Atomic Force Micrographs (scale bar 200 nm) of α-NPD films processed by (a) thermal evaporation and solutions of (b) chloroform and (c) chlorobenzene. Films processed using chlorobenzene as a solvent are found to have surface roughness comparable to the vacuum-deposited films (2.4 and 2.8 nm respectively). The film processed using chloroform is found to have higher roughness (7.7 nm). The measurement area size used is $1 \times 1\ \mu m^2$

To investigate how the current-voltage characteristics compare in double-carrier devices, OLEDs were fabricated by sandwiching a Spiro-TAD between a hole-injection layer of PEDOT:PSS an electron-injecting Ba(5 nm)/Al(100 nm) top electrode. As can be seen in Figure 4-8 the J-V characteristics are almost identical for the solution-processed and vacuum deposited device. Due to large built-in voltage, also the leakage current is visible at low voltages. The leakage current predominantly depends on the film quality. Interestingly, it is observed that the leakage current for the solution-processed film is even somewhat lower than for the thermally evaporated film in this case, indicating that a closed and pinhole-free film is obtained with the solution process.

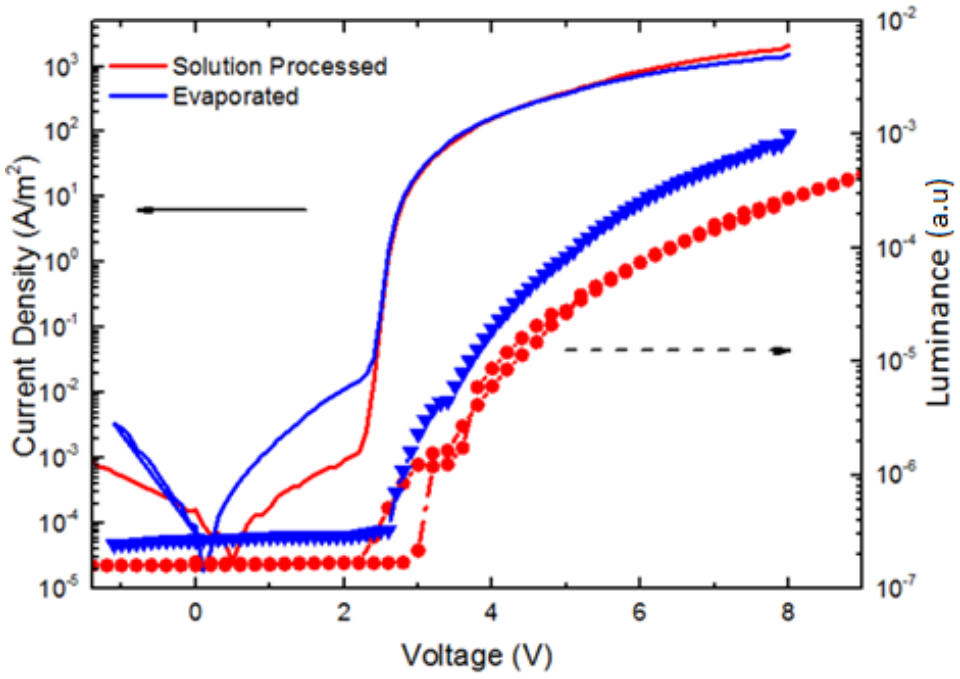

Figure 4-8: J-V characteristics of single-layer OLEDs with Spiro-TAD (100 nm) as the emitter layer (lines). The symbols represent the corresponding luminance-voltage characteristics.

Also plotted in Figure 4-8 is the recorded light output. In contrast to the current density, the measured luminance is lower for the solution-processed device. The reason for this can be an increased concentration of electron traps, which lowers the light output because of an increased amount of non-radiative trap-assisted recombination. Another reason can be the presence of a slightly higher injection barrier for electrons in the solution-processed device, which is not unlikely considering the low electron affinity of Spiro-TAD [18]. However, the fact that the (hole-dominated) current is the same in the also in an OLED configuration once more shows that equal hole-transport behavior can be equally good in a solution-processed device.

4.4 Conclusion

In summary, hole transport was studied in films of the small molecules of Spiro-TAD and α-NPD deposited using two different methods: solution processing and thermal evaporation. Even though these molecules are originally designed for vacuum deposition, the obtained hole mobility can reach equal values when these materials are deposited from solution.

Numerical simulations of the temperature-dependent hole transport using the EGDM resulted in equal values for the energetic disorder, amounting to 0.09 eV for both materials and deposition processes. The numerical simulations are found to be in excellent agreement with the experimental transport characteristics. AFM characterization indicated that the solution processed films were smooth and uniform. Our comprehensive experimental and numerical study of the transport properties for different deposition conditions shows that solution processing can be tailored to be a viable alternative to vacuum deposition for charge-transport layers in optoelectronic devices.

References

[1] R.-P. Xu, Y.-Q. Li, and J.-X. Tang, J. Mater. Chem. C **4**, 9116 (2016).

[2] H.-W. Chen, J.-H. Lee, B.-Y. Lin, S. Chen, and S.-T. Wu, Light Sci. Appl. **7**, 17168 (2018).

[3] R. A. Belisle, P. Jain, R. Prasanna, T. Leijtens, and M. D. McGehee, ACS Energy Lett. **1**, 556 (2016).

[4] K. S. Yook and J. Y. Lee, Adv. Mater. **26**, 4218 (2014).

[5] L. Duan, L. Hou, T.-W. Lee, J. Qiao, D. Zhang, G. Dong, L. Wang, and Y. Qiu, J. Mater. Chem. **20**, 6392 (2010).

[6] J. Salbeck, N. Yu, J. Bauer, F. Weissortel, and H. Bestgen, Synth. Met. **91**, 209 (1997).

[7] T.-W. Lee, T. Noh, H.-W. Shin, O. Kwon, J.-J. Park, B.-K. Choi, M.-S. Kim, D. W. Shin, and Y.-R. Kim, Adv. Funct. Mater. **19**, 1625 (2009).

[8] S. Feng, L. Duan, L. Hou, J. Qiao, D. Zhang, G. Dong, L. Wang, and Y. Qiu, J. Phys. Chem. C **115**, 14278 (2011).

[9] G.-J. A. Wetzelaer, D. Hartmann, S. G. Santamarıa, M. Perez-Morales, A. S. Portillo, M. Lenes, W. Sarfert, and H. J. Bolink, Org. Electron. **12**, 1644 (2011).

[10] M. Shibata, Y. Sakai, and D. Yokoyama, J. Mater. Chem. C **3**, 11178 (2015).

[11] R. Rohloff, N. B. Kotadiya, N. Cr˘aciun, P. W. Blom, and G. Wetzelaer, Appl. Phys. Lett. **110**, 073301 (2017).

[12] A. Kunz, P.W. Blom, and J. J. Michels, J. Mater. Chem. C **5**, 3042 (2017).

[13] N. B. Kotadiya, H. Lu, A. Mondal, Y. Ie, D. Andrienko, P. W. Blom, and G.-J. A. Wetzelaer, Nat. Mater. **17**, 329 (2018).

[14] W. Pasveer, J. Cottaar, C. Tanase, R. Coehoorn, P. Bobbert, P. Blom, D. De Leeuw, and M. Michels, Phys. Rev. Lett. **94**, 206601 (2005).

[15] L. J. Koster, E. Smits, V. Mihailetchi, and P. Blom, Phys. Rev. B **72**, 085205 (2005).

[16] A. Masse, P. Friederich, F. Symalla, F. Liu, R. Nitsche, R. Coehoorn, W. Wenzel, and P. A. Bobbert, Phys. Rev. B **93**, 195209 (2016).

[17] T. P. Saragi, T. Spehr, A. Siebert, T. Fuhrmann-Lieker, and J. Salbeck, Chem. Rev. **107**, 1011 (2007).

[18] A. Kahn, N. Koch, and W. Gao, J Polym Sci B Polym Phys. **41**, 2529 (2003).

Chapter 5

Charge transport in organic semiconductor films of α-NPD doped with the high electron affinity dopant F6TCNNQ

In this chapter[3], we investigate the charge transport in p-type doped films of the archetypical hole transport material α-NPD doped with the high electron affinity dopant, F6TCNNQ. Analysis of space-charge-limited current measurements for different doping concentrations reveals that only a small percentage of free charge carriers is generated with respect to the doping concentration, which is corroborated by impedance measurements. It is observed that higher applied electric fields assist the dissociation of coulombically bound charge-transfer states.

5.1 Introduction

Molecular doping of organic semiconductors has been widely used in the last decades to obtain increased conductivity and reduced contact barriers in charge-transport layers in organic light-emitting diodes (OLEDs), solar cells, field effect transistors (FETs) etc. [1-3]. One of the main disadvantages found in organic semiconductors is the low charge carrier

[3] The contents of this chapter has been adapted from: D. K. Mangalore, P. W. M. Blom, G.-J. A. H. Wetzelaer, Study of charge transport in doped hole transport layers with the high electron affinity dopants, Under review

mobility, which stems from the low orbital overlap between the weakly interacting molecules. Combined with the low intrinsic charge-carrier concentrations in organic semiconductors, this results in low electrical conductivity. To increase the conductivity, organic semiconductors can be doped with molecular dopants that have either a high electron affinity to obtain p-type doping [4-6], or a low ionization energy to obtain n-type doping [7]. Such dopants induce charge transfer, such that the charge-carrier concentration in the host increases. Apart from increasing the conductivity, the increased charge-carrier concentration reduces the width of the depletion layer near the electrode-semiconductor interface, resulting in improved charge injection from the electrode.

Although doped charge transport layers have been successfully used in devices, it remains challenging to decouple the effects of the mobility and the charge-carrier concentration on the conductivity of doped organic thin films. For small molecular doped films as used in OLEDs, a detailed experimental investigation of the charge transport beyond conductivity measurements is lacking.

5.2 Sample fabrication and characterization

To investigate the effect of p-type doping on the charge transport of α-NPD, we performed space-charge-limited current measurements on hole-only devices[4], using F6TCNNQ as a strong dopant. At low doping concentrations, the current is expected to depend linearly on voltage in the low voltage regime. At low voltage, the doping-induced charge-carrier concentration is larger than the injected charge concentration. At higher voltage, the space-charge density will become higher than the doping-induced charge concentration, resulting in a quadratic space-charge-limited current. As a result, the mobility can be obtained from the higher voltage region, which can be used to infer the doping-induced charge-carrier concentration in the linear regime at low voltage [8]. This allows for discrimination of the effects of charge concentration and mobility on the conductivity in doped organic films.

[4]The devices were fabricated by Novaled GmbH

Such measurements were performed on hole-only devices, consisting of a lightly doped α-NPD layer sandwiched between heavily doped α-NPD hole-injection layers. The hole-only devices were prepared on glass substrates with indium-tin oxide electrodes. The first layer consists of α-NPD (host) doped with 10% F6TCNNQ (dopant), prepared by thermally co-evaporation under vacuum, to form a 10 nm injection layer. The process was repeated to obtain the thicker (150 nm or 200 nm) layer of α-NPD (host) which was again doped with F6TCNNQ. The doping ratio was varied from 0.5% to 4% to comprehensively study and understand the effect of doping over a range of doping concentrations. Finally, an injection layer of 10 % doped α-NPD was deposited. For, the top contact Au was thermally deposited then capped with Al. The schematic of the device structure is shown in Figure 5-1: a) Schematic structure of a P-i-P device b) Image of an actual device. The J-V characteristics were measured using a Keithley 4200 SCS under vacuum.

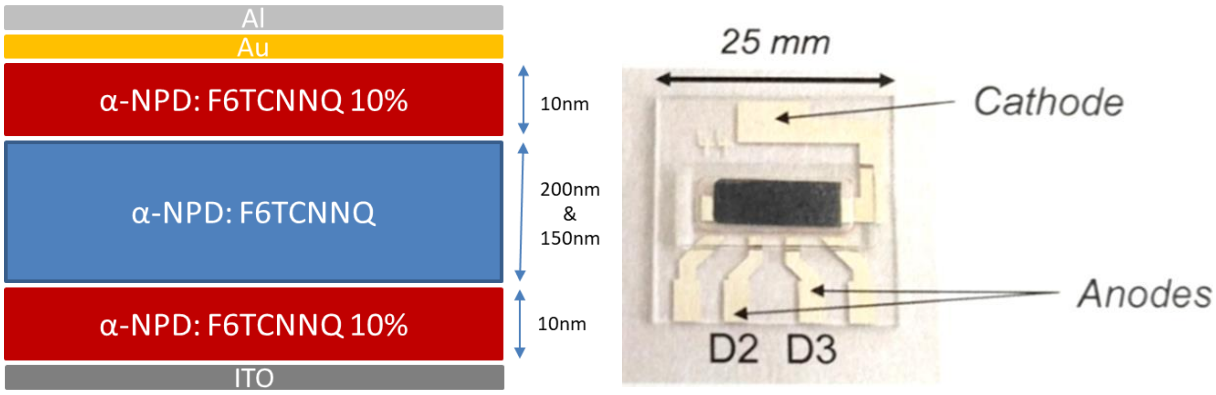

Figure 5-1: a) Schematic structure of a P-i-P device b) Image of an actual device

5.3 Results and Discussion

5.3.1 Current-Voltage characteristics of hole-only oevices of α-NPD doped with F6TCNNQ

First, the charge transport in undoped α-NPD was investigated. The measured current density-voltage characteristics are displayed in Figure 5-2. The hole currents show typical

space-charge limited behavior, with a quadratic dependence of the current on voltage. This allows for direct determination of the mobility by using the Mott-Gurney square law [9]

$$J_{SCLC} = \frac{9}{8}\epsilon_0\epsilon_r\mu_p\frac{V^2}{L^3} \tag{5.1}$$

where $\epsilon_0\epsilon_r$ are the permittivity of the layer, μ_p is the hole mobility and L, is the layer thickness of the transport layer. A hole mobility of 3×10^{-8} m^2 V^{-1} s^{-1} was determined, consistent with previously obtained values [10].

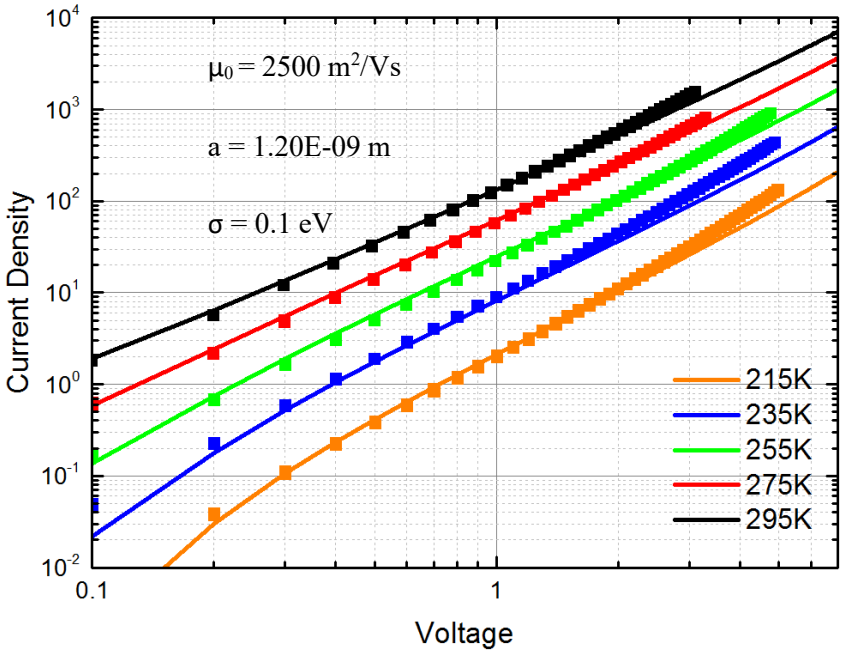

Figure 5-2: Temperature dependent J-V characteristics of an undoped α-NPD (150 nm) hole-only device. Dotted lines refer to experimental measurements. Solid lines refer to numerical simulations

The charge transport can be analyzed more precisely by simulating the current density-voltage characteristics with drift-diffusion simulations incorporating a mobility that depends on temperature, charge-carrier density and electric field. To this end, we used the mobility function as described by the extended Gaussian disorder model (EGDM) [11], derived for hopping transport in a Gaussian distributed density of states (DOS) (See 2.5 for more details).

The solid lines in Figure 5-2 have been numerically calculated with a a = 1.2 nm and σ = 0.1 eV. A mobility pre-factor $\mu_0 = 2.5 \times 10^3$ m^2 V^{-1} s^{-1} was used, equating to a mobility of 3 × 10^{-8} m^2 V^{-1} s^{-1} at 295 K extrapolated to zero field and density. These parameters are similar to hole only devices previously reported [10] and the temperature dependence of the J-V characteristics is well described at both low and high fields.

For the doped devices, the addition of the p-type dopant F6TCNNQ results in free holes being created in the semiconducting layer. The density of free holes induced by the dopant, p_0, is higher than the charge density injected from the contacts contributing to the space-charge-limited current in the undoped devices at low voltages. An Ohmic current will flow at low voltages as both the background carrier density p_0 and the mobility are constant. The ohmic current is given by [13]

$$J_{ohm} = q p_0 \mu_p \frac{V}{L} \tag{5.2}$$

where q is the magnitude of electron charge, p_0 the free hole density, μ_p the hole mobility at low voltage, and L is the thickness of the semiconductor layer. With increasing voltage, the injection of charges from the contacts increases and space charge builds up in the semiconductor. At higher voltages, the formed space charge will outnumber the background density p_0, leading to the observance of a space-charge-limited current, in which the density increases linearly with voltage, resulting in a quadratic voltage dependence of the current.

Figure 5-3 a shows the *J-V* characteristics as a function of doping concentration. The linear part of the J-V characteristics at low voltage is governed by the product of the hole density p_0 and the hole mobility μ_p. For doping concentrations up to 2%, only the linear part of the *J-V* characteristics increases, while the curves converge at higher voltages, suggesting that the mobility does not substantially increases with doping concentration. The change in the linear regime is therefore due to an increased background density p_0. With $\mu_p(T, p, E)$ known, the background density of free holes can be determined. For instance, a background density of $p_0 = 2 \times 10^{21}\ m^{-3}$ was found for a doping concentration of 1%. Since the mobility depends

on charge-carrier density, the additional background density due to doping results in a minor increase in mobility.

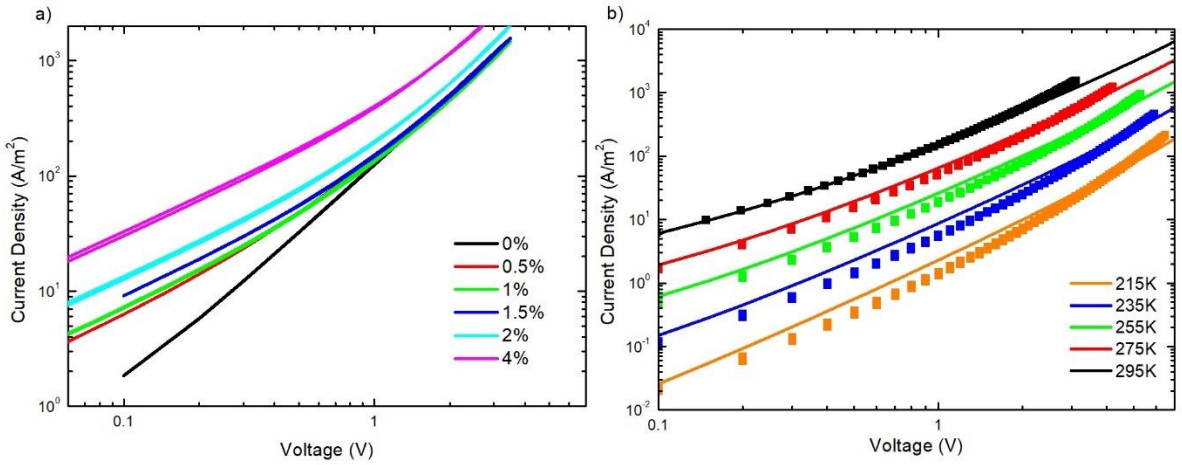

Figure 5-3 a) J-V characteristics at room temperature (295 K) of α-NPD device doped with F6TCNNQ at various concentrations b) Temperature dependence of a 0.5% doped F6TCNNQ: α-NPD device.

In Figure 5-3 b), the temperature dependence of the current is displayed. The background charge density p_0 was assumed to be temperature independent in the simulations, which results in good agreement with the experiments at low voltage. However, for high doping concentrations and low temperatures, the simulations deviate from the experiment at high applied voltage. In previous work, this phenomenon has been ascribed to field-assisted ionization, which effectively results in a field-dependent background density p_0. Here, the simulations contain a constant value for p_0. Since the effects of charge density and electric field are taken into account in the simulated mobility, the deviation from experiment likely results from p_0 being increased at higher applied electric fields. Such effect can be interpreted as the field-assisted dissociation of charge-transfer states, resulting in a higher mobile carrier concentration a higher applied electric field.

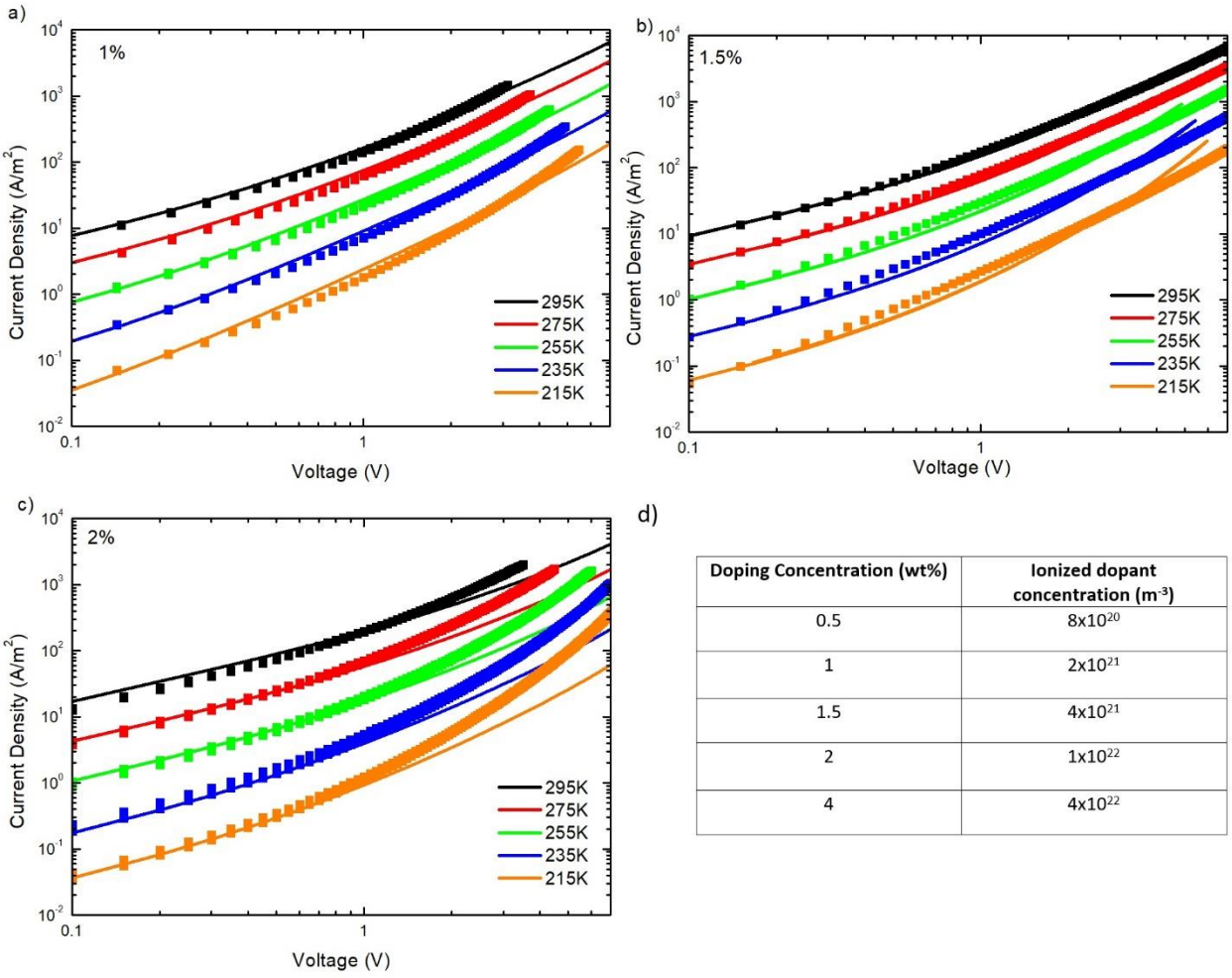

Doping Concentration (wt%)	Ionized dopant concentration (m^{-3})
0.5	$8x10^{20}$
1	$2x10^{21}$
1.5	$4x10^{21}$
2	$1x10^{22}$
4	$4x10^{22}$

Figure 5-4: Temperature dependent J-V characteristics of a doped α-NPD (150 nm) hole-only device for various doping concentration: a) 1% b) 1.5% c) 2%. Dotted lines refer to experimental measurements. Solid lines refer to numerical simulations. d) Doping concentration vs ionized dopant concentration.

5.3.2 Impedance spectroscopy on Schottky diodes of doped α-NPD layers

For the determination of the ionized dopant density, impedance spectroscopy was performed on doped α-NPD p-i-p devices which behave like Schottky diodes. For sufficiently high doping concentrations and efficient doping conditions we observe that the depletion region width will be thinner than the device thickness (see A.1). For such a case, the capacitance

will vary with the applied voltage. This variation of the capacitance with voltage at any given ionized dopant density N_D is given by [12]

$$\frac{1}{C^2} = \frac{2\left(V_{bias} - V - {k_b T}/{q}\right)}{q\varepsilon_s N_D} \tag{5.3}$$

As a result, plotting the C^{-2} versus the voltage and extracting the slope gives the ionized dopant density N_D .

$$N_D = \frac{2}{q\varepsilon_s}\left[-\frac{1}{d(1/C^2)/dV}\right] \tag{5.4}$$

The J-V characteristics of the F6-TCCNQ: α-NPD hole only devices were analyzed as shown in Figure 5-4. When the applied voltage exceeds the built-in voltage, the forward bias is space charge limited and the p_0 can be obtained from the J-V characteristics similar to the method described previously for single carrier hole only devices. In this case, the p_0 obtained at 1% is $2 \times 10^{21}\ m^{-3}$.

It is important to note that changing voltage changes the depletion region and therefore the obtained ionized dopant concentration. Due to the difference in the fermi level between the highly doped interlayer and low doped bulk there is an apparent injection barrier like behavior.

Next the same device was used for impedance measurements where an alternating voltage of magnitude 100mV was applied and under reverse bias the voltage was varied from 0 to -0.5 V. For every DC bias voltage, a frequency scan was then made over a range of 10 Hz to 200 kHz and the impedance was measured. By modelling the device as a parallel RC circuit for the depletion region in series with the parallel RC circuit for the bulk semiconductor, the value for the capacitance of the depletion region is then calculated at each bias. The plot is as shown in figure. The slope of the plot of C^{-2} versus the voltage gives the ionized dopant density as mentioned above. In this case at 1% the value is found to be $8 \times 10^{21}\ m^{'-3}$. The two methods are found to be in good agreement and confirms the analysis and interpretation of the charge carrier density dependent mobility.

a)

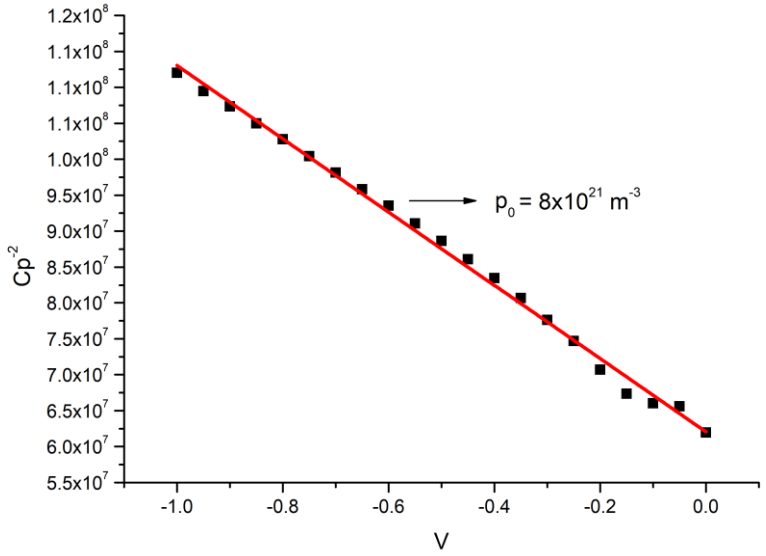

b)

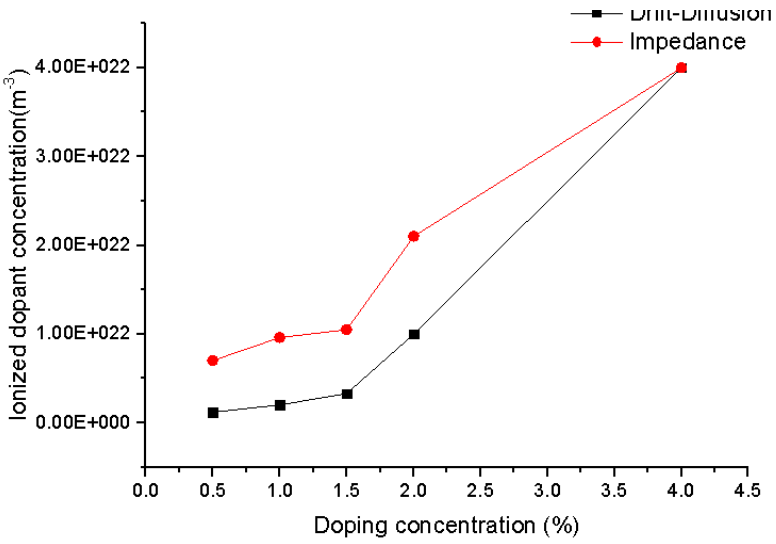

Figure 5-5:a) Depletion region capacitance measurement for a 1% doped F6TCNNQ-α-NPD device. b) ionized dopant concentrations measured by impedance spectroscopy (red) and drift-diffusion simulations (black) of doped F6TCNNQ-α-NPD device for various doping densities.

The numerical simulations were performed with a 0V barrier at the injecting contact. At an ohmic contact, charge carrier diffuse into the organic semiconductor. The carrier density at the interface depends on the barrier height. In order to investigate the effect of the diffused charge carrier concentrations, a small barrier was introduced (0.1eV) however it can be seen (see A.4) that there is no distinguishable effect. Therefore, it is not trial to isolate this effect and calculate the exact charge carrier concentration. This still points that the obtained values of p_0 using both techniques are in the same order of magnitude.

Based on the above evaluations, it can be seen that the mobility as measured in the undoped sample is not just changed by the carrier density p_0 but also by the $F6TCNNQ^-$ counter ions. In small molecules, it has been seen that the hole transport is dominated by energetic disorder.

The doping of small molecules results in an increase of this energetic disorder and also an increase in the width of the DOS is expected due to potential fluctuations which might arise from the Coulomb field of the dopant ions distributed throughout the host matrix. Due to this

Doping concentration [wt%]	**Doping concentration [#molecules/cm^3]**	**Charge concentration due to doping in alpha-NPD [cm^{-3}]**	**Doping efficiency [%]**
0.5	$7x10^{18}$	$1.2x10^{15}$	$1.17x10^{-02}$
1	$1.4x10^{19}$	$1.8x10^{15}$	$1.29x10^{-02}$
1.5	$2.1x10^{19}$	$3x10^{15}$	$1.43x10^{-02}$
2	$3x10^{19}$	$1x10^{16}$	$3.33x10^{-02}$
4	$6x10^{19}$	$4x10^{16}$	$6.67x10^{-02}$

Table 5-1: Doping efficiencies with increasing dopant concentration of a F6TCNNQ doped α-NPD device

The comparison of the amount of dopant carriers with the free carrier density gives doping efficiencies << 1%. A possible explanation for this could be an energetic mismatch between the host and dopant molecules. From the temperature dependence of p_0 the activation

energy can be calculated. Figure 5-5 a) shows the capacitance of the depletion region versus voltage at room temperatures. The zero-voltage capacitance is found to slightly reduce upon cooling down the sample which shows that the free holes available have reduced with reducing temperature.

Due to this reduction in the density, the depletion region should grow and therefore the capacitance C should be smaller as described by the equation below [13].

$$\frac{1}{C^2} = \frac{2\left((V - V_{bi} - \frac{kT}{q}\right)}{q\varepsilon_s p_0} \tag{5.5}$$

where V_{bi} is the built-in voltage and ε_s is the permittivity of the semiconductor.

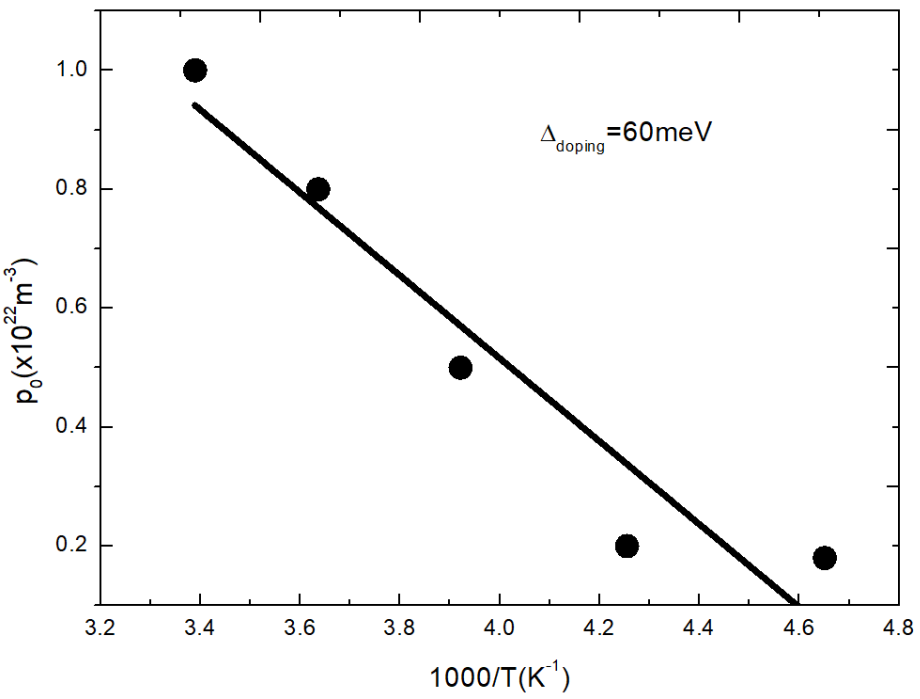

Figure 5-6: Extracted background hole density as a function of temperature. The activation energy amounts to 60 meV

T(K)	p_0(x10^{22}m^{-3})
295	1
275	0.8
255	0.5
235	0.2
215	0.1

Table 5-2: Temperature dependent p_0 values obtained from the numerical simulations of the J-V curves for 2% doped α-NPD films

From the slopes of the C^{-2}-V characteristics, p_0 can be determined at various temperatures. Figure 5-6 shows the temperature dependence of p_0 for 1% doping concentration. For this doping concentration the activation energy for the ionization of free holes from the $F6TCNNQ^-$ ions can be obtained and amounts to 60 meV. This shows that in the temperature range of 215-300 K, p_0 only changes by a factor of ≈ 5.

The temperature dependence p_0 values for 2% doped films are shown in Table 5-2. Due to the absence of a large activation energy and the fact that p_0 is small, it is difficult to distinguish the doping-induced density from the density of diffused charge carriers from the electrodes in the J-V measurements.

5.4 Conclusion

In conclusion, charge transport was investigated in films of the α-NPD (host) doped with the high electron affinity dopant F6TCNNQ. While charge transfer from dopant to host occurs, the concentration of mobile charge carriers is only a fraction of the doping concentration, resulting in doping efficiencies in the order of 0.1-0.01%. At higher electric fields, more mobile charges are generated, which is interpreted as the dissociation of Coulombically bound charge transfer states. This demonstrates that while charge transfer may be efficient,

free charge-carrier generation is severely limited by the Coulombic attraction of the countercharge on the dopant.

References

[1] R.-P. Xu, Y.-Q. Li, and J.-X. Tang, J. Mater. Chem. C **4**, 9116 (2016).

[2] H.-W. Chen, J.-H. Lee, B.-Y. Lin, S. Chen, and S.-T. Wu, Light Sci. Appl. **7**, 17168 (2018).

[3] R. A. Belisle, P. Jain, R. Prasanna, T. Leijtens, and M. D. McGehee, ACS Energy Lett. **1**, 556 (2016).

[4] Y. Liu, B. Nell, K. Ortstein, Z. Wu, Y. Karpov, T. Beryozkina, S. Lenk, A. Kiriy, K. Leo, and S. Reineke, ACS Appl. Mater. Interfaces **11**, 11660 (2019).

[5] W. Gao and A. Kahn, Appl. Phys. Lett. **79**, 4040 (2001).

[6] W. Gao and A. Kahn, J. Appl. Phys. **94**, 359 (2003).

[7] T.-W. Lee, T. Noh, H.-W. Shin, O. Kwon, J.-J. Park, B.-K. Choi, M.-S. Kim, D. W. Shin, and Y.-R. Kim, Adv. Funct. Mater. **19**, 1625 (2009).

[8] Y. Zhang, B. de Boer, and P. W. M. Blom, Adv. Funct. Mater. **19**, 1901 (2009).

[9] R. Rohloff, N. B. Kotadiya, N. Cr˘aciun, P. W. Blom, and G. Wetzelaer, Appl. Phys. Lett. **110**, 073301 (2017).

[10] D. K. Mangalore, P. W. M. Blom, and G.-J. A. H. Wetzelaer, APL Mater. **7**, 011105 (2019).

[11] W. Pasveer, J. Cottaar, C. Tanase, R. Coehoorn, P. Bobbert, P. Blom, D. De Leeuw, and M. Michels, Phys. Rev. Lett. **94**, 206601 (2005).

[12] Y. Zhang and P. W. Blom, Org. Electron. **11**, 1261 (2010).

Chapter 6

Efficient doping of solution processed Spiro-OMeTAD

In this chapter[5], we investigate the charge transport in solution-processed Spiro-OMeTAD layers and compare the doping efficiency of the two p-type dopants, F4TCNQ and F6TCNNQ at low to moderate doping concentration in a diode device configuration. It is found that the addition of dopants drastically improves the conductivity of Spiro-OMeTAD. By numerical modelling of the current density-voltage characteristics, it is found that the doping efficiency at low electric fields is above 1%, which is considerably higher than the doping efficiency of evaporated Spiro-TAD:F6TCNNQ reference films. In addition, the doping efficiency is observed to increase with increasing electric fields, possibly originated from field-assisted ionization of the dopants.

6.1 Introduction

Hole transport layers (HTLs) play a very important role in the performance of OLEDs and OPVs. In order to minimize charge accumulation and to also prevent recombination of holes i.e., the positive charge carriers, the energetics and mobilities of these layers must be highly controlled and balanced for optimal device performance [1]. For example, in perovskite solar

[5] The contents of this chapter has been adapted from: D. K. Mangalore, P. W. M. Blom, G.-J. A. H. Wetzelaer, Study of charge transport in doped hole transport layers with the high electron affinity dopants, Under review

cells, the HTL provides hole conduction and electron blocking, which results in reduced recombination and increased fill factor (FF) and power conversion efficiency (PCE) [2-3].

In perovskite solar cells, the HTL also plays a role in the structural integrity as it is generally on top of the active layer and impacts the stability and lifetime. To realize these devices commercially, the two main criteria are performance and stability. For this to be realized it is important to optimize and understand the functioning of such hole transport layers. Organic polymers such as PTAA, poly(3,4-ethylenedioxythiophene) polystyrene sulfonate (PEDOT:PSS), or poly(3-hexylthiophene) (P3HT) are commonly used as hole transport layers, as they are found to have high mobility and can be solution processed [1]. However, batch-to-batch molecular weight variation can not only alter the physical and chemical properties but also drive-up manufacturing costs.

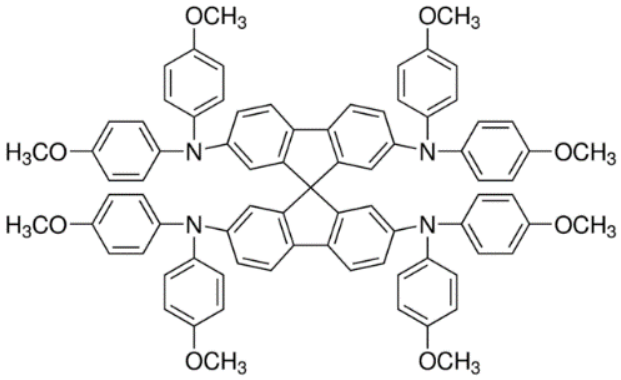

Figure 6-1: Chemical structure of Spiro-OMeTAD

Organic small molecule-based hole transport layers such as α-NPD [4], Spiro-TAD [4] and Spiro-OMeTAD [5] have been very widely used as they are versatile with respect to their material characteristics. They demonstrate high batch-to-batch consistency in not only synthesis but also device fabrication, as films of organic small molecule (OSM) HTLs are typically amorphous. With the intention of tuning the properties, p-dopants such as F4TCNQ and F6TCNNQ are also commonly used [6]. In this Chapter, the charge transport in solution-processed layers of Spiro-OMeTAD doped with F4TCNQ or F6TCNNQ are investigated. By

solution processing the active layers, the effect of the dopant on the performance of the individual layers is presented in this work. A comparison between Spiro-OMeTAD and Spiro-TAD doped with F6TCNNQ, and the doping efficiency of both systems is discussed in this chapter.

Generally, the electronic effects of doping are investigated by measuring the charge-carrier mobility in OFET or diodes. However, in OFETs the charge transport is confined in an active layer which is at the gate dielectric which makes it difficult to evaluate the bulk transport properties. In addition, there is a much higher charge carrier density in comparison to diodes, due to which the doping effects might not be clearly visible. In addition, the two different doping characteristics i.e., the field induced doping and the free carrier induced doping cannot be observed in an OFET architecture. Therefore, in this work we use a diode architecture to investigate the charge transport in doped Spiro-OMeTAD.

To alter the semiconducting properties of the pristine organic small molecules, the dopant impurity is added to the bulk matrix. For p-type doping, in contrast to inorganic systems, this process corresponds to the chemical oxidation. The tetracyanoquinodimethane (TCNQ) based doping systems have an advantage that they are compatible with both vacuum and solution processing techniques [7]. TCNQ is a known electron acceptor capable for forming charge-transfer complexes for improved optoelectronic properties and fluorinated TCNQ derivatives have been successfully used to obtain doped Spiro-OMeTAD based HTLs [8]. However, a detailed investigation of the charge transport in such films is lacking.

6.2 Sample fabrication and characterization

To investigate the hole transport properties in the undoped bulk layer, hole only devices of Spiro-OMeTAD were fabricated using glass substrates with a patterned ITO electrode which was spin coated with PEDOT:PSS followed by an annealing step at 140 °C for 10 min to remove residual water. The Spiro-OMeTAD was purchased from Sigma-Aldrich and used without any purification and dissolved in chlorobenzene and spin coated to create a 100 nm

thick layer. To create a hole-only device, a 5 nm top contact of MoO_3 was evaporated[6]. In order to create a robust top contact, it was then covered with a 100 nm Al layer which was exposed to oxygen to create a self-passivated oxide layer. For the p-doped hole only devices, the Spiro-OMeTAD was doped using either F4TCNQ or F6TCNNQ. The solvent used was chlorobenzene and different ratios of Spiro-OMeTAD and the dopant were dissolved and after separately being filtered in advance, were spin cast to form 100 nm thick doped layers.

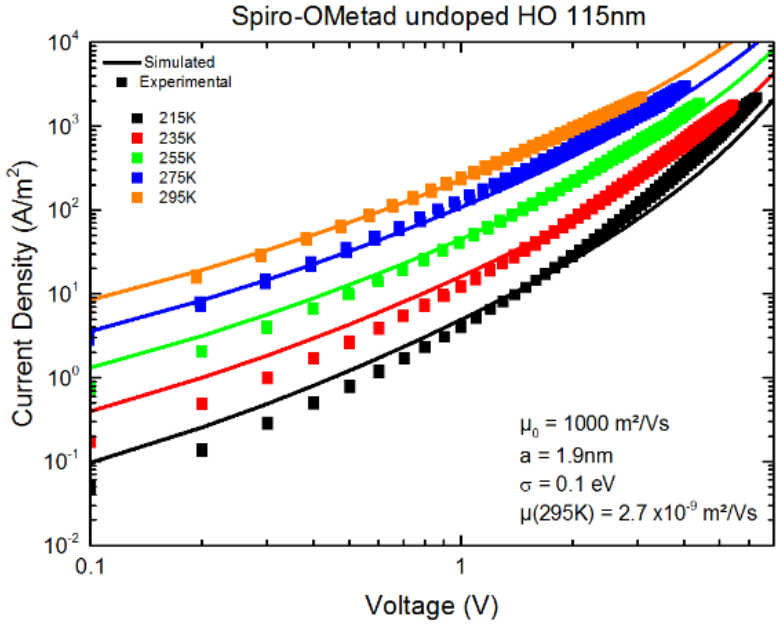

Figure 6-2: Temperature dependent J-V characteristics of an undoped Spiro-OMeTAD (115nm) hole-only device. Dotted lines refer to experimental measurements. Solid lines refer to numerical simulations.

The F4TCNQ was purchased from Sigma Aldrich and the F6TCNNQ was provided by Novaled GmbH. Finally, a 5/100 nm MoO_3/Al top electrode was deposited on the organic layer by thermal evaporation at a chamber pressure of 10^{-7} mbar. The entire process was carried out in an inert nitrogen atmosphere to maintain device stability and eliminate exposure to air. Current–voltage characteristics of the diodes were recorded in the dark and in nitrogen atmosphere using a Keithley 2400 Source Meter.

[6] No interlayer was needed to achieve ohmic contact with MoO_3 and bulk

6.3 Results and Discussion

The MoO_3 contact is used to provide an ohmic contact for the hole-only devices. From a work function point of view, both PEDOT:PSS (5.1 eV) and MoO_3 (6.86 eV [9]) should provide Ohmic hole contacts with the HOMO of Spiro-OMeTAD (-5.1 eV), giving rise to space-charge-limited currents in the undoped devices. Charge transport was investigated by characterizing temperature dependent current density-voltage characteristics.

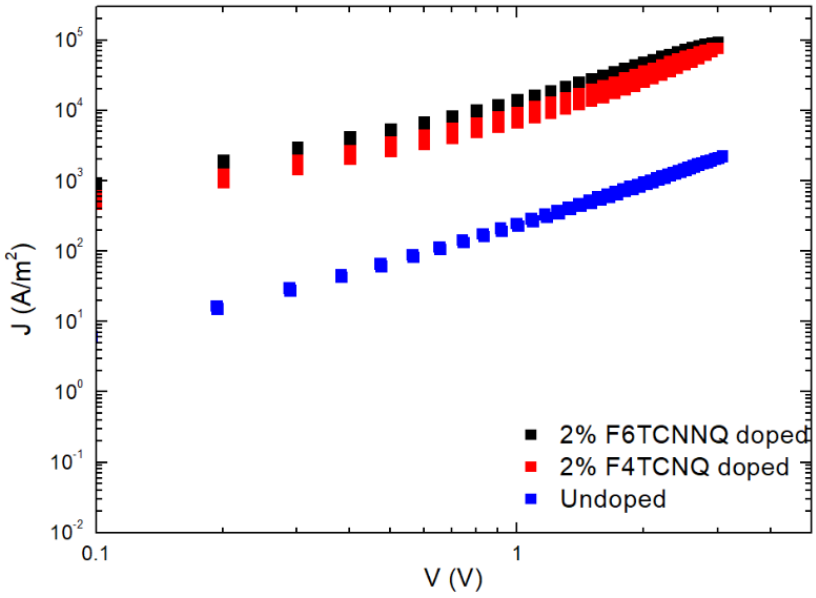

Figure 6-3: Doping of Spiro-OMeTAD with F4TCNQ and F6TCNNQ. J-V characteristics at 295 K and comparison with undoped Spiro-OMeTAD hole only device.

As shown previously [10] the current depends exponentially on the injection barrier and hence the selection of the ohmic charge-injecting contact is important for the determination of the transport characteristics. This ensures that the measured current is not limited by the injection rate, and the calculated mobility is not underestimated.

Figure 6-2 shows the current density versus voltage (*J-V*) characteristics of a PEDOT:PSS/ undoped Spiro-OMeTAD/MoO_3/Al hole-only device at various temperatures. The *J-V* characteristics are also numerically modelled as shown by the solid lines. In the hole-only

device the measured current is found to be a space-charge-limited current (SCLC). For this case, the current density J_{SCLC} can be described by [11]

$$J_{SCLC} = \frac{9}{8}\varepsilon_0\varepsilon_r\mu_p\frac{V^2}{L^3} \tag{6.1}$$

, where $\varepsilon_0\varepsilon_r$ is the permittivity, μ_p is the charge carrier mobility, V the voltage, and L the layer thickness. As can be seen from the above equation, the current scales with thickness to the third power and is directly dependent on the square of the applied voltage. The charge-carrier mobility can be obtained by fitting the SCLC equation to the *J-V* characteristics measured.

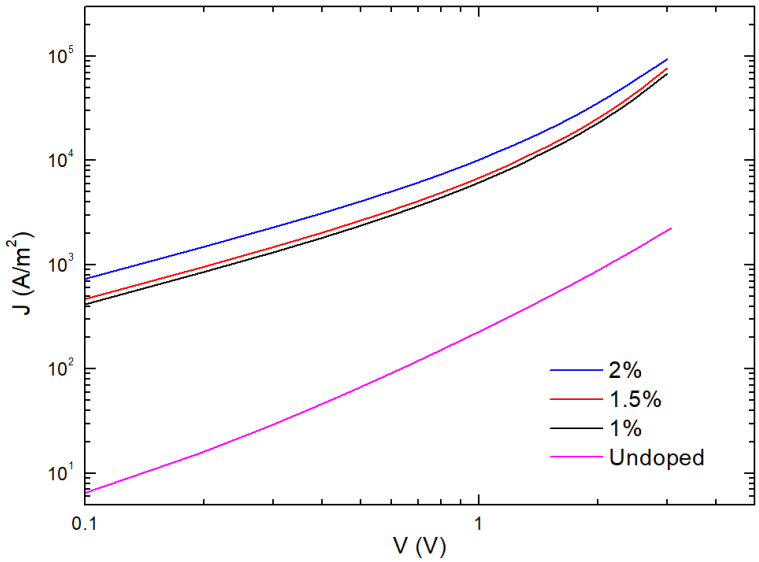

Figure 6-4: Current density with increased doping of Spiro-OMeTAD with F6TCNNQ at 295 K

In the case of disordered organic semiconductors, the charge-carrier density is also dependent on the carrier density and the electric field which leads to a voltage dependent mobility. Extended Gaussian Disorder Model (EGDM) can therefore be used to describe systems with hopping transport between localized energy states and having a Gaussian distribution of the energy states [12]. The EGDM is a well-established mobility model [13-15]and describes the

transport in the system using the following parameters: the width of the density-of-states distribution σ, the lattice constant a and a mobility prefactor μ_0 (See 2.5 for more details).

The current density of an undoped Spiro-OMeTAD hole-only diode as a function of voltage in presented in Figure 6-2 for various temperatures. At low bias voltages, the current density scales with the square of the voltage, which indicates a space-charge limited current. Therefore, the charge transport in the diode is bulk limited. The current density-voltage characteristics are fitted with drift-diffusion simulations incorporating the EGDM. As fit parameters, a room temperature mobility of 2.7×10^{-9} m^2V^{-1} s^{-1} is used with a lattice constant a=1.9 nm and disorder σ =0.1 eV. This is found to be in good agreement with the values reported so far for Spiro-OMeTAD [5]. It is observed that the current density increases and reaches up to 2 orders of magnitude higher current densities (for the measurement at 295 K) at the highest dopant (2%) concentration than that of the undoped Spiro-OMeTAD hole only device (Figure 6-3). The current density is observed to increase with change in doping concentration (Figure 6-4, Doping concentration: 0%, 1%, 1.5%, 2%). The slope indicates that the current is controlled by doping-induced charges and no longer only by the build-up of space charge.

The electron affinity of F6TCNNQ has been previously determined to be 5.60 eV [16] and is one of the strongest organic molecular oxidizing agents used in organic semiconductors. In comparison the electron affinity of F4TCNQ has been previously found to be 5.45eV [16] and is still suitable to be used with small molecules such has Spiro-TAD and Spiro-OMeTAD (See 3.1)

For the doped devices, the numerical drift diffusion model was also used to model the charge transport, which, as in the simulation of the undoped device, incorporates a mobility that depends on the charge-carrier density and the electric field because of energetic disorder. However, for the doped devices, an additional charge concentration p_0 was added, which is the charge density that arises due to doping. The solid lines in Figure 6-5 show a good agreement between the experimental and the simulated data at low voltage. However, at higher voltages the experimental current deviates from the simulations. In the next step,

charge transport in Spiro-TAD doped with F6TCNNQ is measured and it is observed (Figure 6-6) that the current density increases with increase in doping concentration. (See 3.1 for material properties of the hosts and dopants). The numerical analysis is repeated for the charge transport in Spiro-TAD devices and it is observed that similar to doped Spiro-OMeTAD devices there is a good agreement between the experimental and the simulated data at low voltage, however at higher voltages the experimental current deviates from the simulations. Additionally, it is seen that the current densities in Spiro-TAD devices are lower than in Spiro-OMeTAD devices.

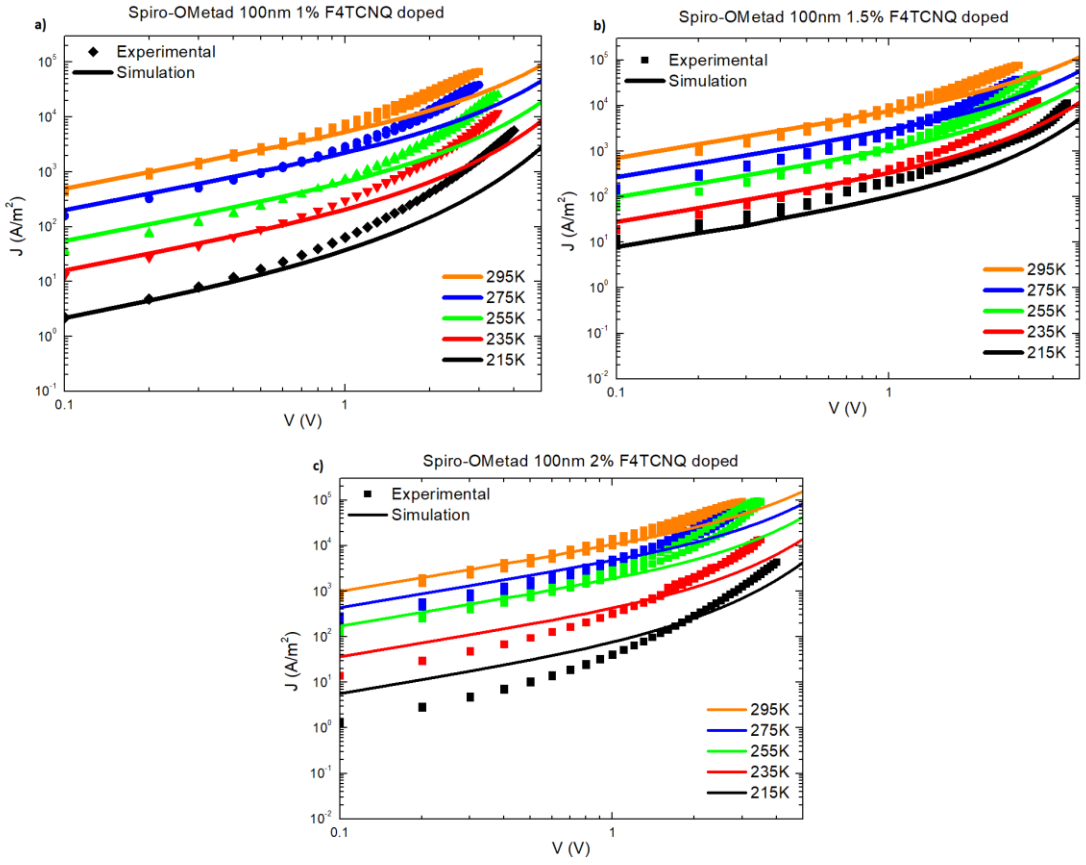

Figure 6-5 : Temperature dependent J-V measurement of F4TCNQ doped Spiro-OMeTAD. Dotted lines refer to experimental measurements. Solid lines refer to numerical simulations. a) dopant concentration of 1% b) dopant concentration of 1.5% and c) dopant concentration of 2%

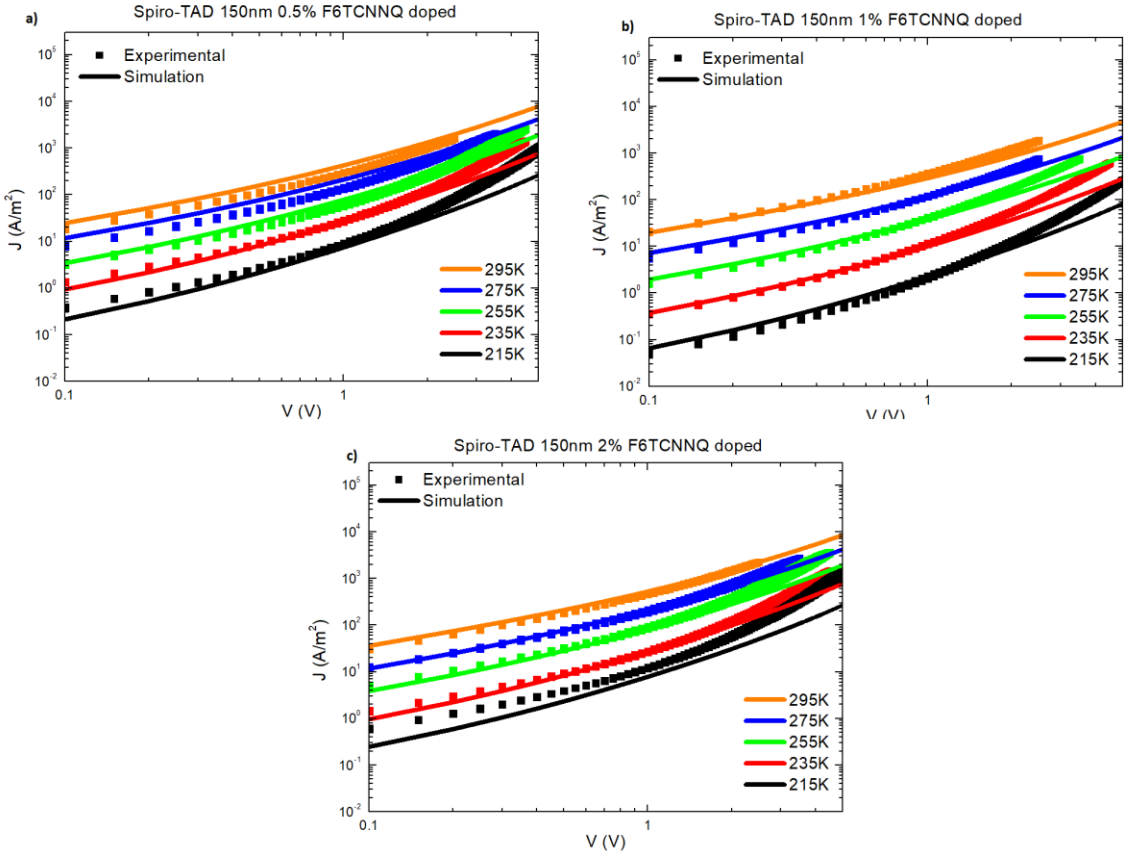

Figure 6-6: Temperature dependent J-V measurement of F6TCNNQ doped Spiro-TAD[7]. Dotted lines refer to experimental measurements. Solid lines refer to numerical simulations. a) dopant concentration of 0.5 % b) dopant concentration of 1% and c) dopant concentration of 2%

Since the simulations already contain the effect of the charge-carrier density and electric field on the mobility, an additional factor must affect the transport at higher applied voltages. At higher doping concentrations and lower temperatures, the deviation of the simulations from the experiment is observed to increase.

[7] These devices were fabricated by Novaled GmbH

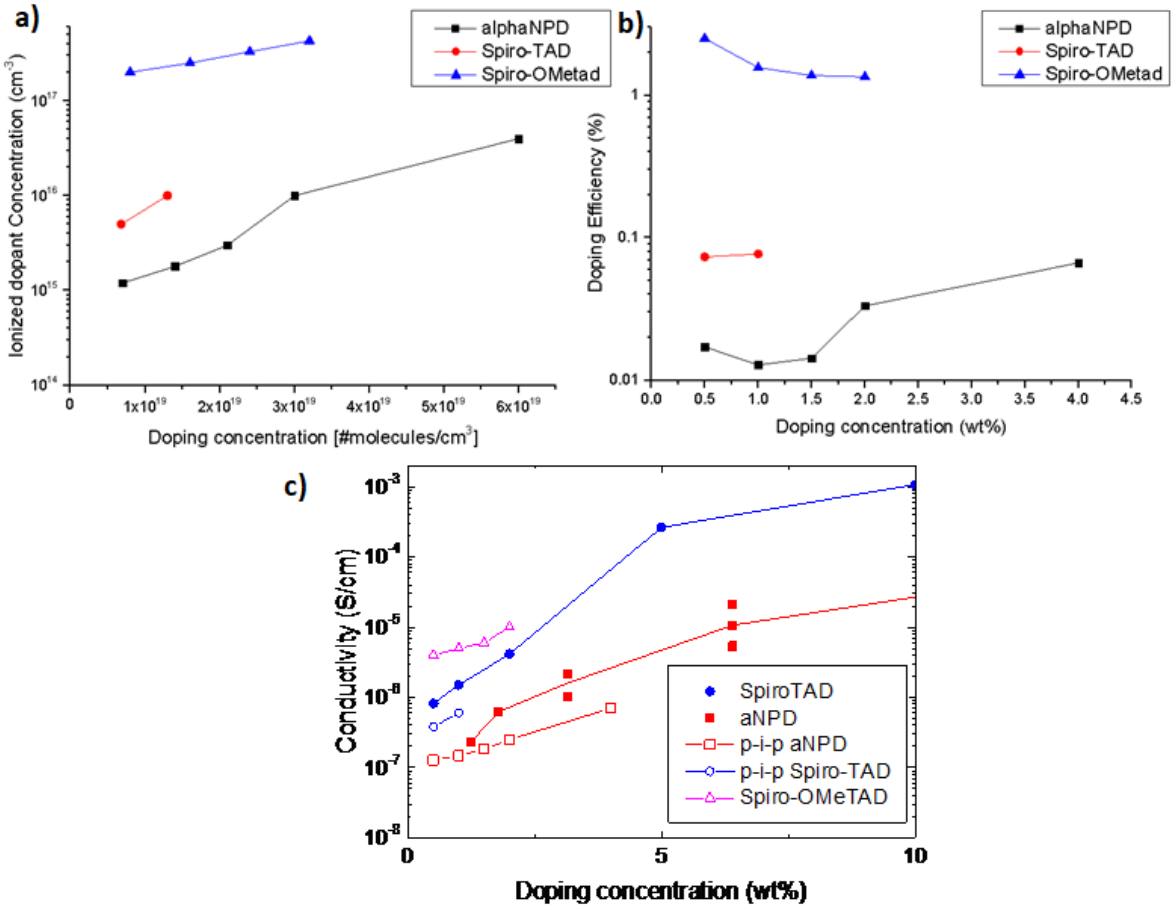

Figure 6-7: Comparison of F6TCNNQ doping in α-NPD, Spiro-TAD, Spiro-OMeTAD. a) dopant ion concentrations versus doping concentrations b) a) doping efficiency versus doping concentrations c) conductivity vs doping concentration.

Such behavior has been observed previously for a conjugated polymer doped with F4TCNQ, which was ascribed to field-assisted ionization of the dopant [17]. This implies that with increasing electric fields, more free charge carriers from the dopants are generated. Possibly, this results from field-assisted dissociation of charge-transfer states between a hole in the semiconductor and an electron on the dopant. In the simulations presented in Figure 6-5 and Figure 6-6, the doping-induced charge density p_0 was assumed to be field independent, explaining the deviations between the simulations and the experimental characteristics. However as indicated for the increasing field, the dotted lines vary from the experimental

measurements showing at high electric fields (E) and low temperatures (T<270 K) the model calculations start becoming inconsistent and with higher voltages, the curves exhibit an increasing dependence on the electric field's indicating field assisted ionization of the dopant concentrations. Figure 6-7 shows the extracted dopant ion concentrations (at low fields) versus dopant concentrations in the samples measured.

Doping concentration [wt.%]	**Doping concentration [#molecules/cm^3]**	**Charge concentration due to doping in Spiro-TAD [cm^{-3}]**	**Doping efficiency (in %)**
0.5	6.80×10^{18}	5.00×10^{15}	7.35×10^{-2}
1	1.3×10^{19}	1.00×10^{16}	7.69×10^{-2}

Table 6-1 Doping efficiency of F6TCNNQ in Spiro-TAD

Doping concentration [wt.%]	**Doping concentration [#molecules/cm^3]**	**Charge concentration due to doping in Spiro-OMeTAD [cm^{-3}]**	**Doping efficiency (in %)**
0.5	8.00×10^{18}	2.00×10^{17}	2.50
1	1.60×10^{19}	2.50×10^{17}	1.56
1.5	2.40×10^{19}	3.30×10^{17}	1.38
2	3.20×10^{19}	4.30×10^{17}	1.34

Table 6-2 Doping efficiency of F6TCNNQ in Spiro-OMeTADTable 6-1 and Table 6-2 provide an overview of calculated doping efficiencies for Spiro-TAD and Spiro-OMeTAD respectively. It is seen that Spiro-OMeTAD is found to be a better host matrix, despite the solution processing of the dopant rather than the thermally co-evaporated F6TCNNQ doped Spiro-TAD.

This observation agrees with theoretical studies by Thompson et. al., where dynamics for dopants in a 3D periodic cubic lattice were simulated by kinetic Monte Carlo (kMC) for a range of molar doping ratios from 0.01% - 10% [18]. In this study the role of morphology on the doping efficiency is investigated in α-NPD and Spiro-TAD both doped with F6TCNNQ. Both systems are configured to have identical electronic coupling, energetic disorder and

connectivity between the sites. The system is however parameterized to have different electrostatic disorder between sites and the interaction with the field is also different for the two systems. They observe that increasing the size of the molecules (from α-NPD to Spiro-TAD) by treating the carriers as point charges at molecule centres results in a largely increased charge transport. It is seen that extremely different charge dynamics and measured doping efficiency is seen by a small change in the molecule size. In conclusion they see that the escape probability responds more strongly to the applied field at large separations and for small lattice spacings.

In order to investigate the possible mechanisms for the doping and further probe the reduced efficiencies, spectroscopy measurements were performed both in solvent and of thin films. However there was no distinct signature observed in the measurement (see A.2, A.3) . In literature there is evidence for charge transfer complex formation upon doping 4T with F4TCNQ and similarly the corresponding polymer P3HT despite structurally similarity is found to have spectroscopic evidence for IPAs [19]. In the case of Spiro-TAD and Spiro-OMeTAD it should be noted at the very low dopant concentrations there is no clear indication if the spectral signature points to any species such as ionized CPXs being present

Hence within the current measurement techniques and the measured regime it is not possible to clearly attribute the behavior to either of the two doping mechanisms: Ion Pair Formation and Charge Transfer Complex Formation (see 2.8 for more details). Due to the nature of the electrical measurements obtained and the HOMO and LUMO levels of the hosts and dopants used (see 3.1 for more details), it can be speculated that the behavior points towards the Charge Transfer Complex mechanism in the systems investigated, in line with other reports [6]. This further indicates there is as yet an incomplete understanding of the process behind the doping in small molecules. Due to the presence of a large number of molecules of the dopant, only <1% of them release mobile holes in to the host. As discussed above, the potential reason for this discrepancy possibly arises from the case that there are holes which are trapped due to being Coulombically bound to the ionized dopant molecules, or the charge transfer complexes.

6.4 Conclusion

In summary, the charge transport in solution-processed Spiro-OMeTAD doped with the high electron affinity dopants F4-TCNQ or F6-TCNNQ was studied. The doping efficiency was found to be higher than for evaporated films of Spiro-TAD doped with F6TCNNQ. For example, for a doping concentration of 3.2×10^{19} molecules/cm^3 a charge concentration of 4.3×10^{17} cm^{-3} was obtained at low electric fields, corresponding to a doping efficiency of 1.34%, whereas the doping efficiency of F6TCNNQ in Spiro-TAD remains below 0.1%. At higher electric field, the doping efficiency was observed to increase due to field-assisted ionization of the dopants. In conclusion, it is seen that that solution processed, and doped hole transport layer (Spiro-OMeTAD) can achieve higher doping efficiency than thermally co-evaporated and doped hole transport layer (Spiro-TAD).

References

[1] Y. Shirota and H. Kageyama, Chem. Rev. **107**, 953 (2007).

[2] R. A. Belisle, P. Jain, R. Prasanna, T. Leijtens, and M. D. McGehee, ACS Energy Lett. **1**, 556 (2016).

[3] L. Calió, S. Kazim, M. Grätzel, and S. Ahmad, Angew. Chem. Int. Ed. **55**, 14522 (2016).

[4] D. K. Mangalore, P. W. M. Blom, and G.-J. A. H. Wetzelaer, "Hole-transport comparison between solution-processed and vacuum-deposited organic semiconductors", APL Mater. **7**, 011105 (2019).

[5] J. A. Röhr, X. Shi, S. A. Haque, T. Kirchartz, and J. Nelson, Phys.Rev. Applied **9**, 044017 (2018).

[6] F. Zhang and A. Kahn, Adv. Funct. Mater. **28**, 1703780 (2018).

[7] Y. Guo, W. Sato, K. Inoue, W. Zhang, G. Yu, and E. Nakamura, J. Mater.Chem. A **4**, 18852 (2016).

[8] J. Luo, C. Jia, Z. Wan, F. Han, B. Zhao, and R. Wang, J. Power Sources **342**, 886 (2017).

[9] M. Kröger, S. Hamwi, J. Meyer, T. Riedl, W. Kowalsky, and A. Kahn, Applied Physics Letters **95**, 123301 (2009).

[10] N. B. Kotadiya, H. Lu, A. Mondal, Y. Ie, D. Andrienko, P. W. Blom, and G.-J. A. Wetzelaer, Nat. Mater. **17**, 329 (2018).

[11] R. Rohloff, N. B. Kotadiya, N. Cr˘aciun, P. W. Blom, and G. Wetzelaer, Appl. Phys. Lett. **110**, 073301 (2017).

[12] W. Pasveer, J. Cottaar, C. Tanase, R. Coehoorn, P. Bobbert, P. Blom, D. De Leeuw, and M. Michels, Phys. Rev. Lett. **94**, 206601 (2005).

[13] G. A. H. Wetzelaer, AIP Advances **8**, 035320 (2018).

[14] R. Coehoorn and P. A. Bobbert, Phys. Status Solidi A **209**, 2354 (2012).

[15] A. Massé, P. Friederich, F. Symalla, F. Liu, R. Nitsche, R. Coehoorn, W. Wenzel, and P. A. Bobbert, Phys. Rev. B **93**, 195209 (2016).

[16] F. Zhang, A. Kahn, Adv. Funct. Mater. **28**, 1703780 (2018).

[17] Y. Zhang and P. W. Blom, Org. Electron. **11**, 1261 (2010).

[18] I. R. Thompson, A. B. Walker, W. R. Saunders, O. M. Roscion, M. Ricci, C. Zannoni, G. D'Avino, Y. Olivier, D. Beljonne, "Effect of long-range interactions on mesoscopic carrier dynamics and organic semiconductor doping efficiency", Unpublished work

[19] H. Méndez, G. Heimel, S. Winkler, J. Frisch, A. Opitz, K. Sauer, B. Wegner, M. Oehzelt, C. Röthel, S. Duhm, D. Többens, N. Koch, I. Salzmann, Nat. Commun. **6**, 8560 (2015).

Chapter 7

Conjugated polymer based integrated circuits

In this chapter[8] we solution process a difluorobenzothiadiazole-oligothiophene copolymer (PffBT4T-2DT) into a well-ordered monolayer and demonstrate an integrated circuit of hundreds of polymer monolayer field-effect transistors (PoM-FETs). We achieve a field-effect mobility of up to 3 $cm^2\ V^{-1}\ s^{-1}$ due to the pronounced organization of polymer chains which greatly facilitate the charge carrier transport within the monolayer. Making use of the improved FET fabrication process, high molecular order and contact engineering we are not only able to achieve high mobility but also large current modulation and high reproducibility of PffBT4T-2DT PoM-FETs. This reproducibility allows for combing the PoM-FETs into inverters to form unipolar gates, and the small parameter spread allows for the construction ofring oscillators from the individual inverters. In the next step, we successfully fabricate a state-of-the-art example of an organic integrated circuit (IC) by constructing a 15-bit code generator and thus demonstrating the potential of using bottom-up organic electronics.

7.1 Introduction

The fabrication of polymer based monolayer field-effect transistors has been challenging because of the crystallization and film formation properties of the conjugated polymers. The transport of the charge carriers in OFETs predominantly takes place the first few layers of the

[8] The contents of this chapter have been adapted from: M. Li and D. K. Mangalore et al., Nat. Commun. 9, 451 (2018)

semiconducting organic layer which is adjacent to the gate dielectric [1-2]. Therefore, OFETs based on a monolayer of organic semiconductor can be constructed, in which the charges are confined exclusively to the monolayer on top of the gate dielectric. Monolayer transistors provide a near-ideal platform for the investigation of fundamental transport mechanisms, due to the two-dimensional nature of the monolayer and therefore confinement of the charge carriers and their pathways in two dimensions [3]. Not only is the monolayer transistor important to understand the underlying physics in the charge transport properties of the conjugated polymers, but they also hold great potential in applications relevant to chemical and biological sensing as the transistor channel is accessible and more sensitive. This enhancement in sensitivity also leads to faster response and recovery rate and increased selectivity.

The monolayer deposition is critical to the performance of such devices. By thermal evaporation in high vacuum, thickness and deposition parameters have been shown to be effectively controlled leading to enhanced performance of transistors. Organic monolayer-based transistors have been fabricated in recent years using thermal evaporation in high vacuum and have demonstrated high mobilities. Devices fabricated using monolayers of pentacene [4], oligothiophene [5] and their derivatives [6] have demonstrated field-effect mobilities of around 10^{-2} cm^2 $V^{-1}s^{-1}$. In the case of solution processing, drop-casting has been used to deposit monolayer films or single crystals and devices fabricated with this method have demonstrate mobilities ranging from 10^{-2} to 1 cm^2 V^{-1} s^{-1} [7-10]. Alternatively, self-assembly has also been used as a method of bottom-up fabrication to downscale the semiconductor layer into a monolayer. This is done by chemically modifying the π–conjugated semiconducting core with an anchoring group which is capable of covalent binding to the dielectric surface. Devices using this technique are called self-assembled monolayer field-effect transistors (SAMFETs) and have been shown to reach mobilities of 0.01– 0.04 cm^2 V^{-1} s^{-1}, providing a route to realize functional integrated circuits [11-14]. While semiconducting conjugated polymers have been seen as interesting candidates due to their flexibility and solution processability, it has been found to be challenging to obtain high charge carrier mobilities in conjugated PoM-FETs [15-16].

Fabrication of conjugated PoM-FETs is a great challenge due to the intricate crystallization and film formation of conjugated polymers. In this chapter, the charge transport in PoM-FETs based on a single monolayer of a conjugated polymer is studied. The organic compound used in this work is a donor-acceptor conjugated polymer, PffBT4T-2DT (Figure 7-1), where 5,6-difluorobenzothiadiazole is the acceptor unit and quarterthiophene with long branched alkyl chains attached is the donor unit.

The PoM-FETs are found to be highly reproducible and achieve charge carrier mobilities of 3 $cm^2\ V^{-1}\ s^{-1}$. The high carrier mobilities arise from the strong interactions of the polymer chains which are already present in solution and lead to pronounced edge-on packing and well-defined monolayer microstructures [17].

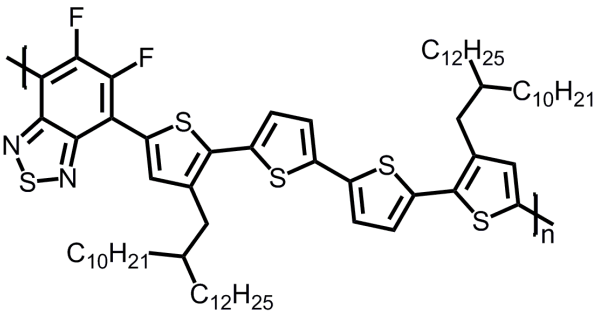

Figure 7-1: Chemical structure of PffBT4T-2DT

In the next step we used the unipolar PoM-FETs and configured it as inverters and ring oscillators to perform discrete logic operations. This was further extended to construct and demonstrate successfully a 15-bit code generator in which hundreds of self-assembled PoM-FETS are addressed simultaneously. This demonstration of logic functionality provides a state-of-the-art example of fabricating integrated circuits based on conjugated polymer monolayer demonstrating promising prospects for largescale application of bottom-up electronics.

7.2 Sample fabrication and characterization

The substrates used for the PoM-FETs were purchased from BASF and Philips Research Laboratories Eindhoven. The substrates were heavily n-doped silicon wafers as bottom gate electrode, with a 250 nm thick thermally grown silicon oxide layer as bottom insulator with a capacitance of 17 nF cm^2.

The purchased substrate had gold (Au) source and drain electrodes which were patterned on top of the oxide layer using conventional lithography. There was also a 10 nm layer of titanium below the Au, which was used as adhesion layer between Au and SiO2. Ring and interpenetrating finger FET structures with channel lengths (L) varying from 0.5 to 40 μm and a constant channel width, W= 20000 μm are patterned on the substrate. The two FET configurations are shown in Figure 7-6.

The pre-patterned substrates were first cleaned by 10 min ultrasonication in acetone and then followed with a further 10 min ultrasonication in isopropyl alcohol before being dried with nitrogen[9]. For the dip coating process, the substrate is first activated using argon plasma for 1 min and the Au electrodes are functionalized with self-assembled monolayers (SAMs) by immersing the cleaned substrates into a 10 mM 2,3,4,5,6-pentafluorothiophenol (PFBT, Aldrich) solution in ethanol for 6 hours. The substrates were then rinsed with ethanol and dried under nitrogen flow. The substrates were then dip coated to deposit polymer mono- and multilayers from a 0.5 mg mL^{-1} chloroform solution with the speeds ranging from 1000 to 50 μm s^{-1} in a chloroform evaporated environment. For this purpose, a chloroform solution of 8 mL at 0.5 mg mL^{-1} was prepared in a 10 mL vial. After the deposition, the polymer mono- and multilayers were annealed at 100 °C for 0.5 h in a glovebox under a nitrogen atmosphere to remove the residual chloroform. The electrical characterization was performed in an inert atmosphere by using a Keithley 4200-Semiconductor Characterization System at room temperature.

[9] The samples measured in this chapter were fabricated and processed by M. Li, Max Planck Institute for Polymer Research, Mainz

In Figure 7-2 a schematic representation of the layout of a FET is shown along with a typical measured transfer curve (see Section 2.4 for a detailed discussion on OFETs).

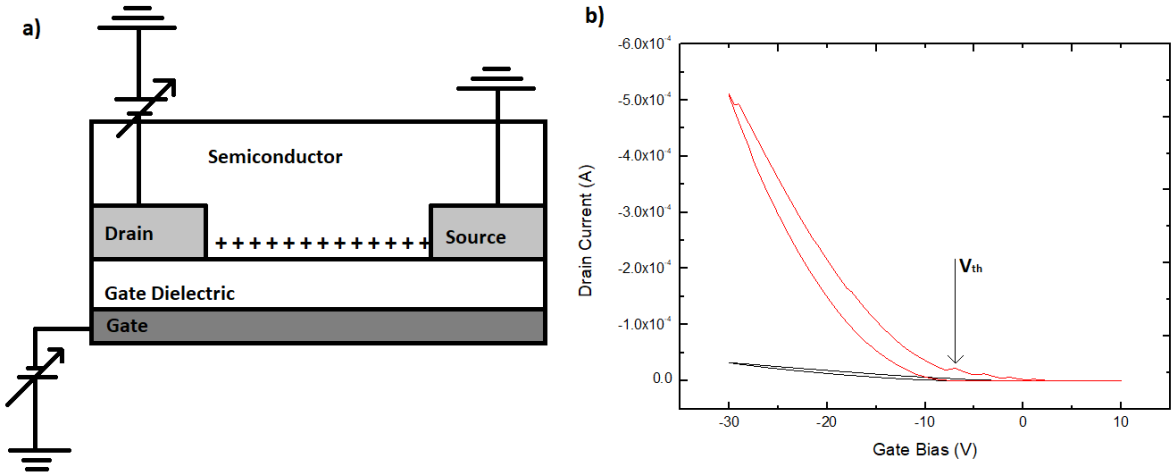

Figure 7-2: (a) Schematic of a field-effect transistor (side view) (b) Transfer curve of a unipolar OFET comprising a p-type semiconductor. At negative gate bias current flows and the current is depleted at positive gate bias.

The equations derived previously (see Section 2.4) are used to calculate the key device parameters such as the threshold voltage and the carrier mobility to compare the different devices. Figure 7-6 shows a micrograph of the device structure

7.3 Results and Discussion

In Figure 7-3 a)-b) the PoM-FET transfer and output characteristics of PffBT4T-2DT are displayed, which exhibits a typical linear/saturation behavior. At drain voltages (V_{DS}) of −2 V and −30 V of the transfer plots linear and saturation regimes are observed, respectively. From the PoM-FET transfer curves hole mobilities of μ_{lin} = 1.02 $cm^2\ V^{-1}\ s^{-1}$ and μ_{sat} = 2.08 $cm^2\ V^{-1}\ s^{-1}$ are extracted. The devices demonstrate thermal activation of the mobillty, and the activation energy is found to be 90 meV (Figure 7-4). To demonstrate that the mobility is independent of device geometry we fabricate and characterize transistors (greater than 80

discrete PoM-FETs) with different Source/Drain electrode geometries such as co-centric rings, interdigitated and linear devices of PffBT4T-2DT PoM-FETs.

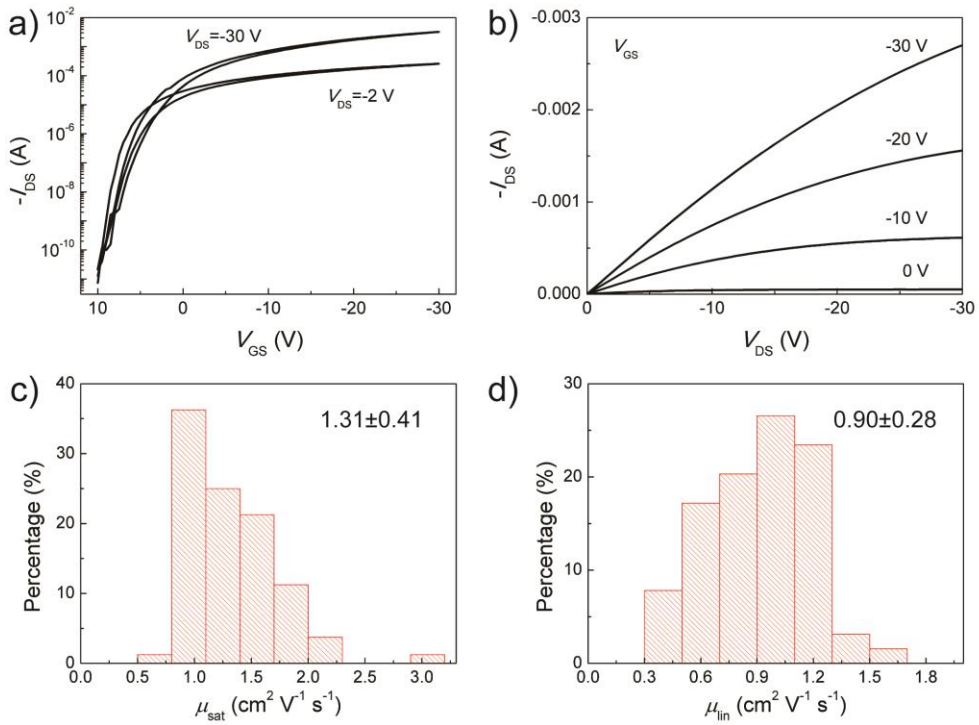

Figure 7-3: a)-b) Transfer and output characteristics of a PffBT4T-2DT monolayer ring transistor. The channel length and width are 10 µm and 2500 µm, respectively. The drain voltages used in a) are -2 V and -30 V for the measurement in the linear and saturation regimes, respectively. c-d) The distribution of saturation and linear mobility (μ_{sat} and μ_{lin}) of the polymer monolayer transistors. S/D electrodes are functionalized by 2,3,4,5,6-pentafluorothiophenol (PFBT) SAMs. Over 80 transistors were measured.

This reinforces the robustness and high reproducibility of the devices. Table 7-1 and Figure 7-3 c)-d). show the measurement results. We see that irrespective of the electrode geometries the threshold voltages (V_T) and on/off ratios (I_{on}/I_{off}) are similar. It is observed that nearly identical values of linear (μ_{lin}) and saturation mobility (μ_{sat}) of 0.90 ± 0.28 cm^2 V^{-1} s^{-1} and 1.31 ± 0.41 cm^2 V^{-1} s^{-1} respectively are obtained for all devices. This shows that the device geometry does not influence the charge carrier mobility. For the best device we measure a μ_{sat} of 3.02 cm^2 V^{-1} s^{-1}, which is a record for polymeric monolayers based FETs.

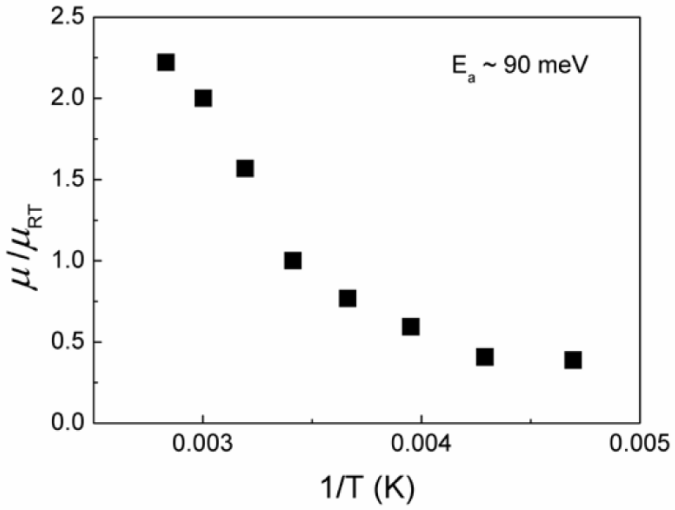

Figure 7-4: The saturation mobility of PffBT4T-2DT monolayer as a function of temperature. M is the saturation mobility measured at different temperatures, and μ_{RT} is the value measured at room temperature. The activation energy is around 90 meV

S/D patterns	μ_{sat} **(cm^2 V^{-1} s^{-1})**	μ_{lin} **(cm^2 V^{-1} s^{-1})**	V_T **(V)**	I_{on}/I_{off}
ring	1.39±0.48	0.99±0.32	8.7±2.5	10^7-10^8
interdigitate	1.17±0.32	0.88±0.20	8.6±2.3	10^7-10^8
linear	1.29±0.36	0.57±0.03	3.3±3.4	10^7-10^8
average[a)]	1.31±0.41	0.90±0.28	6.5±3.8	10^7-10^8

a)Over 80 devices were measured.

Table 7-1: Device performances of PffBT4T-2DT PoM-FETs with three different geometries of source/drain (S/D) patterns

In FETs, the accumulated charge carriers are confined near the semiconductor/dielectric interface and the charge accumulation layer thickness amounts to 2-3 nm [18]. This thickness is comparable to the thickness of the polymer monolayer and due to this the charge carriers

are confined to the existing physical monolayer. This results in two-dimensional electrical transport in the PoM-FETs. In Figure 7-5 we observe a higher on/off ratio, which can be interpreted to be a result of elimination of the bulk current.

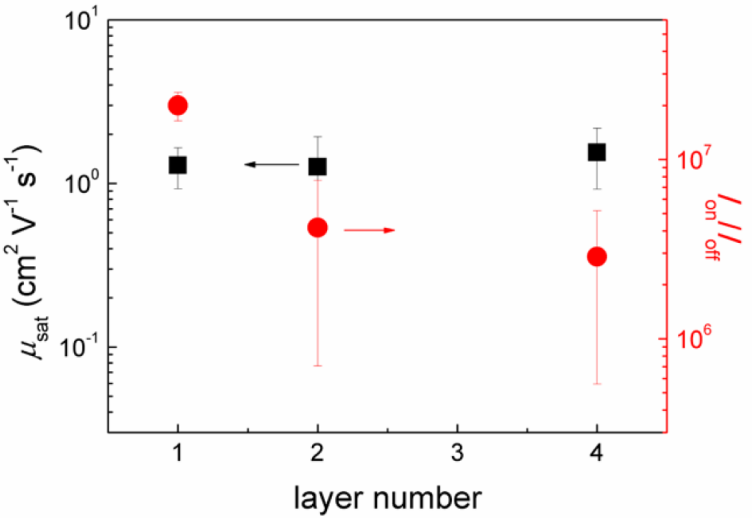

Figure 7-5: The saturation mobility and on/off ratio as a function of layer number forPffBT4T-2DT PoM-FET. It is evident that the charge carrier transport remains independent of layer number. The identical transistor performance of monolayer and multilayers provides further evidence that the first monolayer close to the dielectric is mainly responsible for the charge carrier transport.

In Figure 7-6 we show the channel length scaling for PoM-FETs. It is observed that, for long channels (10–40 μm), the mobility is independent of the channel length . In case of short channels (0.5–10.0 μm) it is observed that both linear and saturation mobilities are reduced with decreasing channel length.

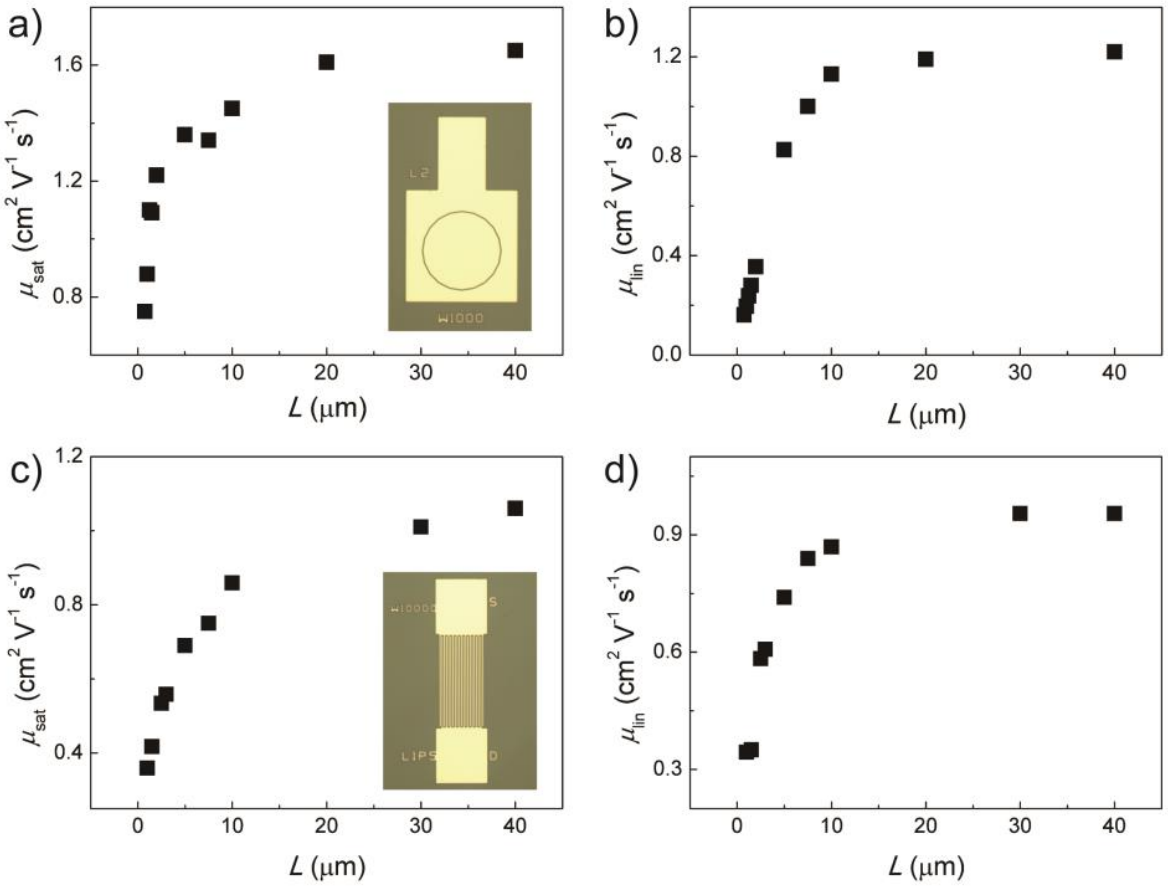

Figure 7-6: The influence of channel length on the saturation (a,c) and linear mobilities (b,d) of PffBT4T-2DT monolayer. Both ring (a,b) and interdigitate transistors (c,d) are analyzed. The channel width is 1000 μm and 10000 μm for ring and interdigitate transistor.

We evaluate the contact and channel resistance using the channel length scaling and this allows the estimation of effective field-effect mobility (μ_{eff}) by application of the gated circular transfer line method (CTLM) [19]. This is shown in Figure 7-7. We obtain effective mobilities of μ_{eff} = 1.3 cm^2 V^{-1} s^{-1} , which is in excellent agreement with the mobility derived from transfer characteristics (Figure 7-3 and Table 7-1).

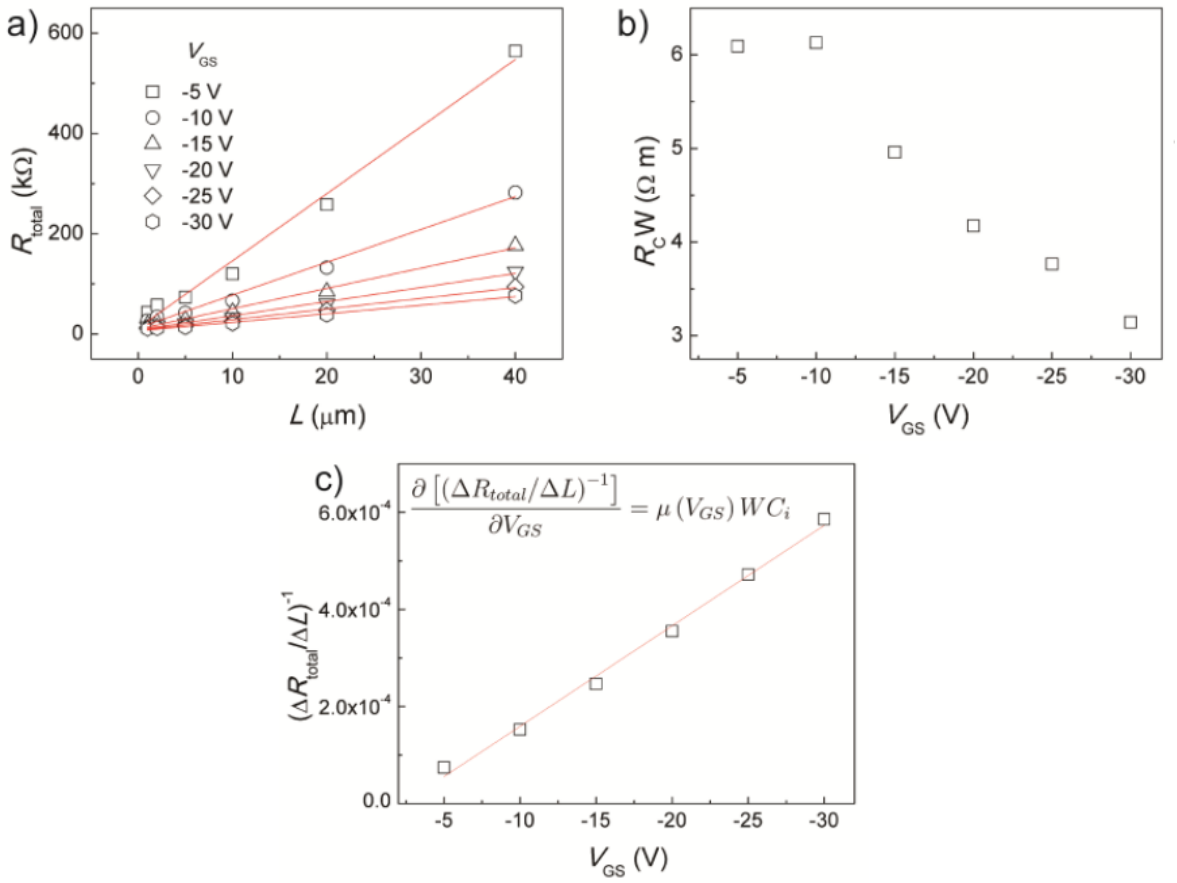

Figure 7-7: a) Total device resistance (R_{total}) as a function of the channel length (L) with various V_{GS} for PffBT4T-2DT monolayer transistor. The channel width is 1000 μm. B) Contact resistance times channel width (W) as a function of V_{GS}. C) The slopes of red lines in a), $(\Delta R_{total}/\Delta L)^{-1}$, as a function of V_{GS}. According to the inset equation, the mobility calculated by transfer-length-method is 1.3 $cm^2\ V^{-1}\ s^{-1}$, in an excellent agreement with the value extracted from the transfer characteristics.

In Table 7-1 we see that there is a very narrow spread visible in the mobility measured over 80 devices. This has allowed the realization of an integrated circuit based on a collection of individual PoM FETs. The integrated circuits and logic gates were adopted based on an earlier process for 150-mm development technology. The device was made by depositing PffBT4T-2DT monolayers on un-patterened substrates. The state of the discrete PoM-FETs are 'normally ON' i.e. they start conducting at 0-bias. This can be seen in Figure 7-3 a).

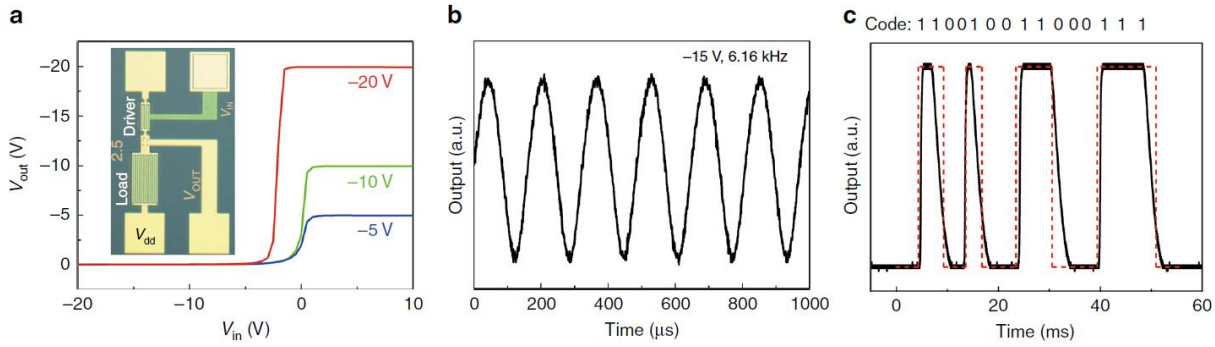

Figure 7-8: Integrated circuits based on PffBT4T-2DT PoM-FETs. A) Static input–output characteristics of a unipolar inverter based on PffBT4T-2DT monolayer with V_{GS} = 0 V. The supplied voltage, V_{dd}, is −5V, −10 V, and −20 V, respectively. The inverter layout is shown as an inset. B) A PoM-FET 7-stage ring oscillator operating at a frequency of 6.16 kHz with a supply voltage of −15 V. c A PoM-FET 15-bit code generator with a bit rate of about 330 bit s^{-1} at V_{dd} = −20 V

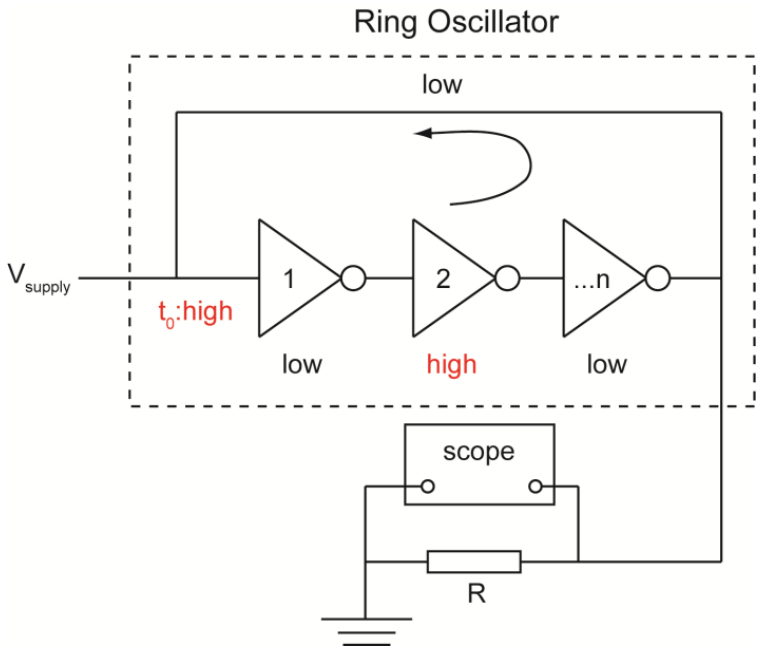

Figure 7-9: Schematic illustration of the measurement set-up for the ring oscillator.

Unipolar V_{GS}=0 logic inverters are used to create the digital circuit and logic gates in which the source electrode of the load transistor is connected to the gate. Figure 7-8 a). shows the

picture of the inverter in the inset. To control the output voltage V_{out}, the input voltage is adjusted through the resistance of the driver transistor [20]. Figure 7-8 a) shows the input-output characteristics of the inverter. There is a clear voltage amplification visible at the output of the inverter. The gain is dependent on the supply voltage V_{dd} and is found to 17.3 V when V_{dd} = 20V as shown in Figure 7-10. The reported record values for gain in polymer thin film transistors is found to be much higher than the gain reported here, however it is noteworthy that this was an initial report value for gain in PoM-FET based inverter devices.

In addition to an inverter logic, a seven-stage ring oscillator was also demonstrated.

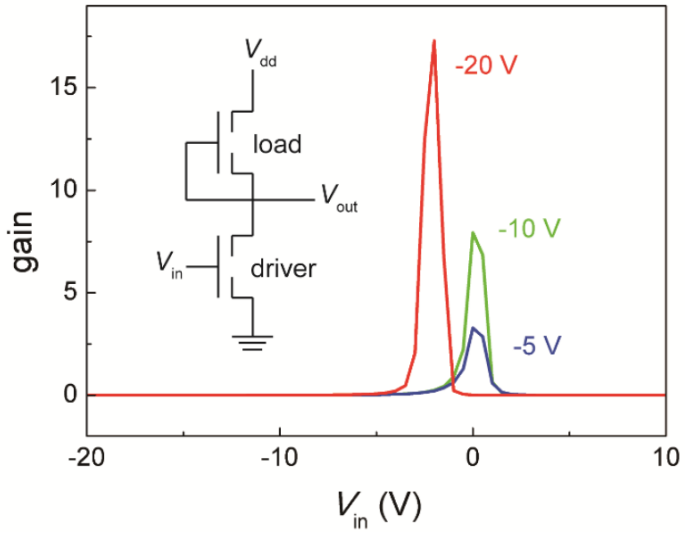

Figure 7-10: Plots of corresponding gain of polymer monolayer inverter (Figure 7-8 a)). V_{in}, input voltage; V_{out}, output voltage. The inset shows a diagram of the logic gate.

Figure 7-9 shows a schematic illustration of the measurement set-up for a ring oscillator. It was observed that at -5 V bias voltage, the output starts spontaneously oscillating. A maximum switching frequency of 6.16 kHz is observed at the supplied voltage of -15 V as shown in Figure 7-8 b) and Figure 7-11.

The delay time t = ½Nf where N is the number of stages and f is the switching frequency. The value of t obtained is 11.6µs and is found to be better than the reported value of carbon

nanotube based oscillator and the lowest reported value for PoM FET based ring oscillator [21-22].

We also demonstrated a 15-bit code generator consisting of over 300 PffBT4T-2DT PoM-FETs, an onboard clock generator, a hard-wired memory, a 4-bit counter, a decoder logic, and a load modulator (Figure 7-12). A bit rate of 330 bit s^{-1} is obtained at a supply voltage of -20 V. This is seen in Figure 7-8 c). The performance is comparable to reported integrated circuits [12, 22-24] which are based on bulk organic thin-films leading to a great potential for the application of PffBT4T-2DT based PoM-FETs in radio-frequency identification transponders.

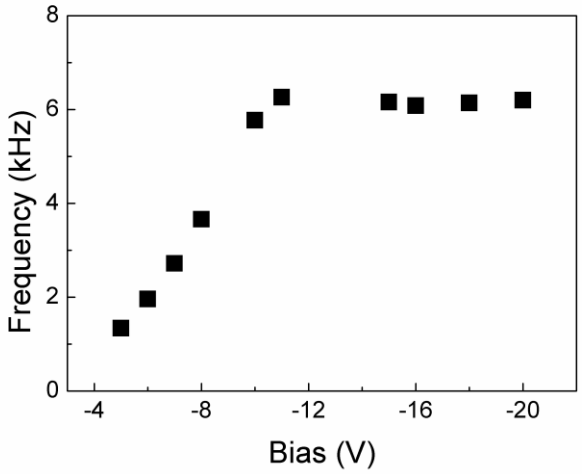

Figure 7-11: The frequency of polymer monolayer ring oscillator as a function of bias voltage.

7.4 Conclusion

In this chapter, we have shown applications of PffBT4T-2DT polymeric monolayer transistors. A strong edge-on orientation in the monolayers was obtained by tuning polymer pre-aggregation in solution. This molecular order and the contact engineering process was used to achieve high performance PoM-FETs resulting in a record mobility of 3.02 $cm^2 V^{-1} s^{-1}$ with reasonable operating conditions (V_T = 6.5 V and $I_{on}/I_{off} = 10^7$) which is one order of

magnitude (on average) higher than the state-of-the-art in literature. The device characteristics of the PoM FETs based on the monolayer were found to be comparable to that of the bulk devices. The integration of the PoM FETS into inverters and oscillators was also demonstrated and found to be dependent on the performance uniformity, large current

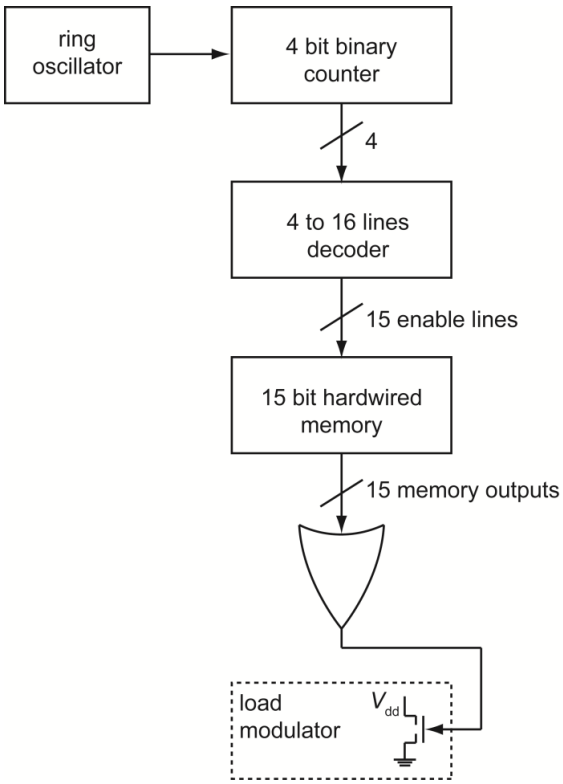

Figure 7-12: Block diagram of the 15-bit code generator.

modulation, and high reproducibility of the PffBT4T-2DT monolayer PoM-FETs. This work also shows the unipolar logic gate device and the ring oscillator function built from individual PoM-FET based inverters. The most important device demonstrated was the 15-bit code generator as this helps complete the device scale up to integrate circuits based on polymeric monolayer transistors and is a big leap in the application areas of bottom-up fabrication of polymeric devices.

References

[1] A. Dodabalapur, L. Torsi and H. E. Katz, , Science **268**, 270–271 (1995).

[2] F. Dinelli, et al., Phys. Rev. Lett. **92**, 116802 (2004).

[3] A. Sharma, F. W. A. van Oost, M. Kemerink and P. A. Bobbert, Phys. Rev. B **85**, 235302 (2012).

[4] R. Ruiz, A. Papadimitratos, A. C. Mayer, & G. G. Malliaras, Adv. Mater. **17**, 1795 (2005).

[5] E. M. Mannebach, et al. Adv. Funct. Mater. **23**, 554 (2013).

[6] J. Huang, J. Sun and H. E. Katz, Adv. Mater. **20**, 2567 (2008).

[7] M. Defaux, et al., Adv. Mater. **24**, 973 (2012).

[8] L. Shan, et al., Adv. Mater. **27**, 3418 (2015).

[9] L. Jiang, et al. Adv. Mater. **23**, 2059 (2011).

[10] M. Halik, A Hirsch Adv. Mater. **23**, 2689 (2011).

[11] E. C. P. Smits et al., Nature **455**, 956 (2008).

[12] S. G. J. Mathijssen, et al., Nat. Nanotechnol. **4**, 674 (2009).

[13] A. V. S. Parry et al., Adv. Funct. Mater. **24**, 6677 (2014).

[14] T. Schmaltz, et al. Adv. Mater. **25**, 4511 (2013).

[15] J. C. Scott, J. D. J. Samuel, J. H. Hou, C. T. Rettner, R. D. Miller, Nano Lett. **6**, 2916 (2006).

[16] S.-i. Watanabe et al., Appl. Phys. Lett. **96**, 173302 (2010).

[17] M. Li , D. K. Mangalore, J. Zhao, J. H. Carpenter, H. Yan, H. Ade, H. Yan, K. Müllen, P. W. M. Blom, W. Pisula, D. M. de Leeuw, K. Asadi, Nat. Commun. **9**, 451 (2018)

[18] J. J. Brondijk, et al., Phys. Rev. Lett. **109**, 056601 (2012).

[19] E. J. Meijer, et al. Appl. Phys. Lett. **82**, 4576 (2003).

[20] L. Kergoat, et al., Proc. Natl Acad. Sci. USA **109**, 8394 (2012).

[21] D.-m. Sun, et al., Nat. Nanotechnol. **6**, 156 (2011).

[22] C. Lu, et al. Sci. Bull. **61**, 1081 (2016).

[23] D. M. Taylor, Jpn. J. Appl. Phys. **55**, 02BA01 (2016).

[24] E. Cantatore, et al., IEEE J. Solid-State Circuits **42**, 84 (2007).

Chapter 8

Conclusion and Outlook

8.1 Summary

The work presented in this thesis aimed to contribute to a deeper understanding of the mechanisms and processes involved in the charge transport of various organic small molecules. For this different fabrication techniques such as thermal evaporation, wire-bar coating, dip coating and spin coating were employed to create thin films. To elucidate the structure of the thin films, AFM investigation was performed. Optical absorption and spectroscopy measurements were conducted with equal importance to identify the neutral and ionized species in mixed solutions as well as in doped films.(see A.2, A.3) The work horse measurements employed were the current-voltage (IV) measurements were conducted to track changes in conductivity upon doping. In addition, impedance spectroscopy was used to corroborate the dopant concentrations obtained after fitting the current-voltage characteristics. Using these experimental techniques, a wide variety of device structures were studied such as hole only devices, OLED, P-i-P devices and OFETs to investigate the following i) the question of which fabrication technique results in optimization of transport and extending it to understand a variety of hole transport materials ii) the p-doping using F4TCNQ and F6TCNNQ of α-NPD, Spiro-TAD and Spiro-OMETAD and finally, iii) the application of highly efficient monolayer based polymer OFET in logic gates, ring oscillators and integrated circuits.

In the first part, hole transport was studied in films of the small molecules of Spiro-TAD and α-NPD. The films were deposited using different techniques: solution processing and thermal evaporation. Although the molecules were originally designed to be used in vacuum

deposition and provide the optimized mobilities under this condition, it was demonstrated that by proper selection of the solvents and controlling the solvent removal itself, the obtained hole mobility can reach the same values when these materials are deposited from solution. In addition, the charge transport showed a similar temperature dependence for solution-processed devices. Numerical simulations of temperature-dependent hole transport of both the materials using the Extended Gaussian Disorder model were performed, which resulted in similar charge-transport parameters for both solution-processed and evaporated films. A width of the Gaussian density-of-states distribution of 0.09 eV for both materials irrespective of the deposition process used was extracted. Using AFM analysis, the films deposited from solution were uniform and smooth. Based on these results, we show that the solution processing technique can be tailored to be a viable alternative to obtain efficient charge-transport in HTL in optoelectronic devices.

In the second part, charge transport was investigated in evaporated films of α-NPD (host) doped with the high electron affinity dopant F6TCNNQ. The work shows that although charge transfer occurs from dopant to host, the achieved concentration of mobile charge carriers is only a fraction of the doping concentration, resulting in very low doping efficiencies in the order of 0.1-0.01%. With increasing bias voltage, i.e., increasing electric field, there are more mobile charges created and can be interpreted as the dissociation of Coulombically bound charge transfer states. Hence in comparison to the existing theoretical work which points that F6TCNNQ might be an ideal candidate for p-type doping of α-NPD, due to the efficient charge transfer, the generation of free charge carriers is not experimentally observed to be efficient and is severely limited by the Coulombic attraction of the counter charge on the dopant.

To further understand how this affects other HTLs that are solution processed, in the third part Spiro-OMeTAD was investigated. Firstly, the hole transport was studied in films of the of Spiro-OMeTAD, a molecule designed for solution processing. The hole mobility is comparable to the other HTL molecules Spiro-TAD and α-NPD. The energy values of HOMO and LUMO are also comparable which made it an ideal candidate to compare the transport properties in doped films and compare to the standard thermally co-evaporated

doped films obtained in the previous work. The charge transport in Spiro-OMeTAD doped with the high electron affinity dopants F4-TCNQ or F6-TCNNQ was studied, and it was found to be a better host matrix than Spiro-TAD. For a doping concentration of $3.20x10^{19}$molecules/cm^3 charge concentration of 4.30E+17 cm^{-3} was achieved. We also showed that a solution processed doped hole transport layer (Spiro-OMeTAD) can achieve higher doping efficiency than thermally co-evaporated doped hole transport layers of Spiro-TAD and α-NPD doped with the same dopant.

In the final part of this thesis, PffBT4T-2DT polymeric monolayer based logic devices were demonstrated. By tuning the molecular order and the contact engineering process a high-performance PoM-FET was created which resulted in a record mobility of 3.02 cm^2 V^{-1} s^{-1}. To demonstrate further applications of solution processed high performance devices, PoM FETs integrated into inverters and oscillators were also demonstrated. The performance uniformity, large current modulation, and high reproducibility of the PffBT4T-2DT monolayer PoM-FETs allowed their use in unipolar logic gate devices and ring oscillators built from individual PoM-FET based inverters. The most significant device demonstrated was the 15-bit code generator which indicated that the devices can be scaled up and it is indeed possible to achieve integrated circuits based on polymeric monolayer transistors.

Overall, this thesis examined topics which are of fundamental and applicational importance to the areas of charge transport in small molecular and polymeric monolayered based organic semiconductors. By using basic material parameters, the mobility and disorder was tuned to achieve high performance not only in pristine devices but also in doped devices. In addition, it was demonstrated that p-doping can be successfully demonstrated to achieve a solution processed doped HTL. And, finally, it was shown how organic FETs can be used in integrated circuit applications by achieving high performance in solution processed films. The results from this thesis may contribute to further understanding of transport and fabrication of organic molecular based devices.

8.2 Outlook

Optoelectronic devices using organic electronics are attractive because of the characteristics of the materials such as being light weight, lower in cost than inorganic semiconductors and capability of scaling up large areas of production and flexible device fabrication [1-2]. Devices such as OLEDs, OPVs and OFETs are based on efficient charge transport being the key for the operation process, which necessitates research focused on understanding charge transport in organic semiconductors. Although this work investigated some of the key materials, there are a range of other hole transport materials especially for use with perovskite solar cells that are critical for efficient device performance. The relationship between material morphologies and properties and device performance is still a subject of interest for further studies. Significant progress has been made on charge transport in amorphous molecular materials, however. the correlation between molecular structures and charge carrier drift mobilities still require further investigation.

There are still a large number of materials which are not commercially utilized, in which cases not only the device performance but also other factors such as synthesis, purifications, low cost, stability, toxicity, lifetimes and so forth have to be solved. A deeper understanding of materials chemistry, device physics, development of new devices and sensors, integration of multiple functions in a single device are still areas that need to be developed.

While electrical doping can improve charge transport and charge injection, resulting in the use of doped transport layer in commercial OLEDs, it is still not fully understood which dopant and host properties result in high doping efficiencies in organic semiconductors. This complicates the search for efficient host-dopant combinations to optimize the performance of organic-semiconductor devices in real-world applications. Therefore, further research is required in this area.

Flexible OLEDs also hold great promise for the optoelectronics industry and while flexible electronics products have already sprung up their progress is inseparable from the further development necessary for the technology such as flexible electrode fabrication, device

fabrication, light manipulation, and device architecture. The primary difficulties lie in making the materials highly flexible yet thermally stable and economically viable. Furthermore, there needs to be further investigation into the light extraction technologies, device degradation mechanisms and encapsulation techniques for OLEDs to derive efficient and stable performance. Therefore, the results of this work on investigation of device physics and optimization of charge transport by different deposition techniques in organic semiconductors is one of the many important steps in achieving efficient commercial devices.

References

[1] P. W. M. Blom, Adv. Mater. Technol. **5**, 2000144 (2020).

[2] M. L. Tietze, J. Benduhn, P. Pahner, B. Nell, M. Schwarze, H. Kleemann, M. Krammer, K. Zojer, K. Vandewal, and K. Leo, Nat. Commun. **9**, 1182 (2018).

Appendix A

A.1 Calculation of depletion width:

The depletion width w_d is given by[10],

$$w_d = \frac{\varepsilon_r \varepsilon_0 A}{C_d} \quad (A.1)$$

Where $\varepsilon_0\varepsilon_r$ is the permittivity, A is the geometric area, C_d is the depletion capacitance. Below are the indicative depletion widths extracted as function of dopant concentration for α- NPD.

Dopant conc. (wt%)	w_d (nm)
0.5	16
1	15
1.5	14
2	14
4	12

A 1 Depletion width calculated for α- NPD for various dopant concentrations

[10] M. L. Tietze, J. Benduhn, P. Pahner, B. Nell, M. Schwarze, H. Kleemann, M. Krammer, K. Zojer, K. Vandewal, and K. Leo, "Elementary steps in electrical doping of organic semiconductors", Nat. Commun. 9, 1182 (2018).

We notice that the depletion width decreases with increasing dopant concentration. This agrees with previous reports[11]. It should be noted that these measurements give a qualitative indication of the depletion width. A more accurate measurement taking into consideration the effects of the stray capacitance and interfaces can be done by using UPS techniques, where the temperature dependent depletion width is given by[11],

$$w_d(T) = \sqrt{\frac{2\varepsilon_r \varepsilon_0 V_{bi}(T)}{eN_{CT}^-}} \qquad (A.2)$$

where $V_{bi}(T)$ is the built-in potential and N_{CT}^- is the free carrier density.

[11] A) M. L. Tietze, J. Benduhn, P. Pahner, B. Nell, M. Schwarze, H. Kleemann, M. Krammer, K. Zojer, K. Vandewal, and K. Leo, "Elementary steps in electrical doping of organic semiconductors", Nat. Commun. 9, 1182 (2018).

B) F. Zhang and A. Kahn, "Investigation of the high electron affinity molecular dopant F6-TCNNQ for hole-transport materials", Adv. Funct. Mater. 28, 1703780 (2018).

A.2 UV-Vis Spectroscopy

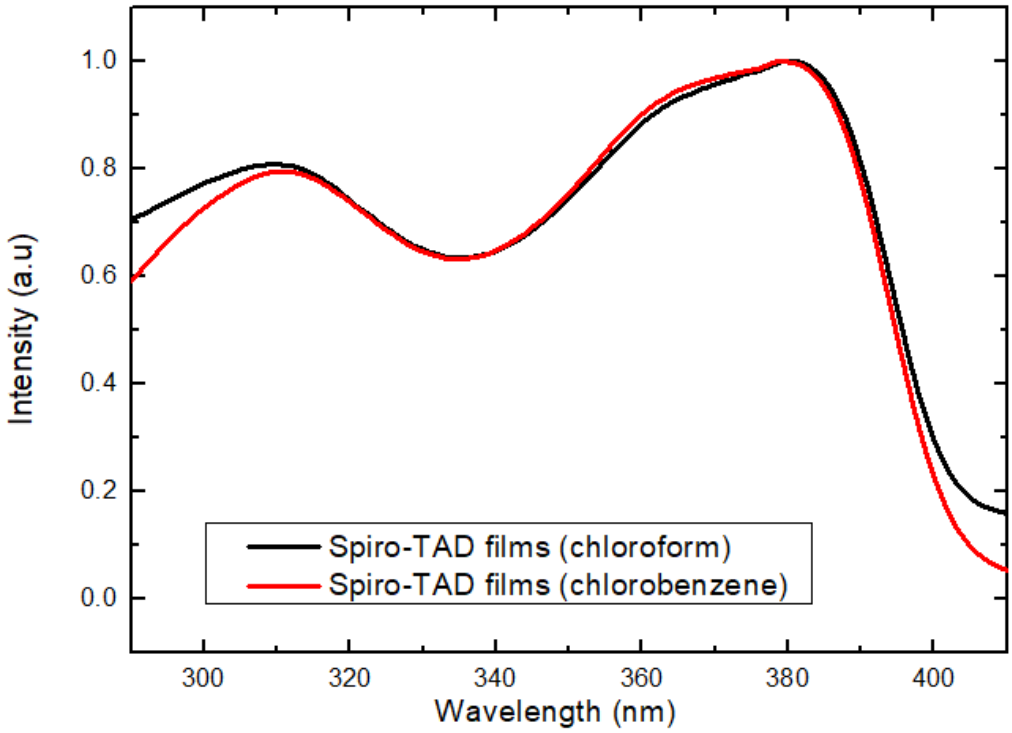

A 2 UV-Vis spectra of undoped solution processed Spiro-TAD films in chloroform (black) and chlorobenzene (red)

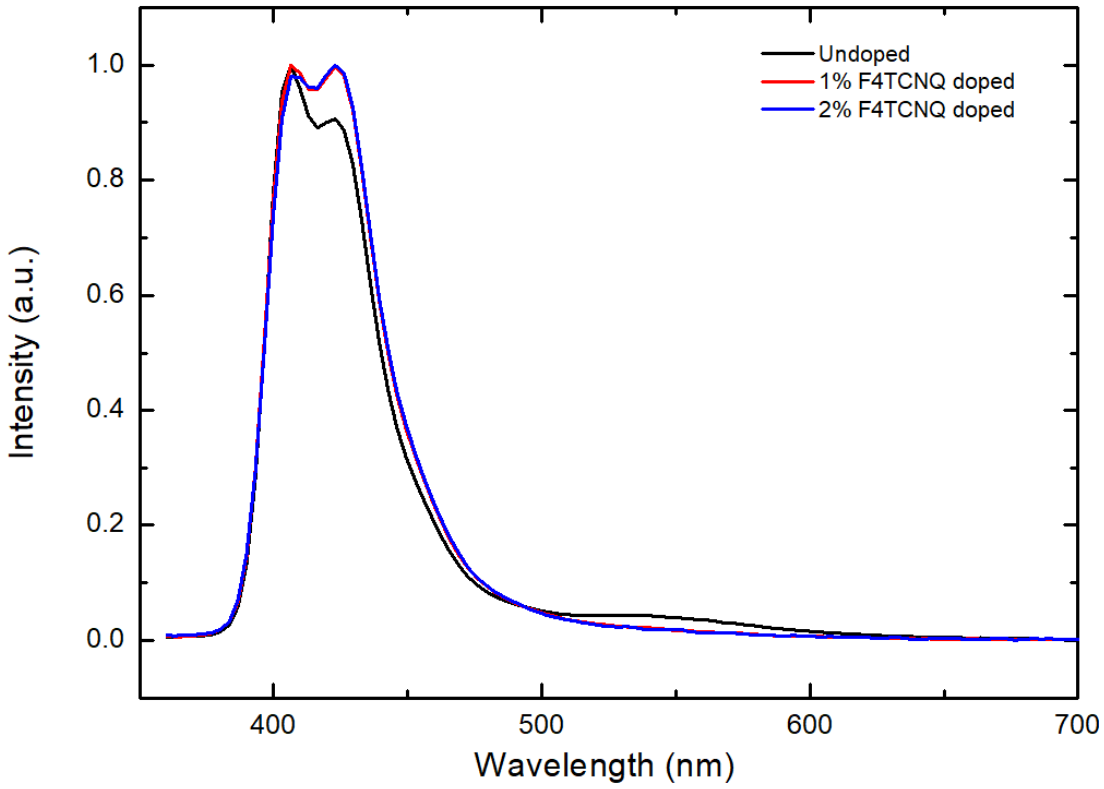

A 3 UV-Vis spectra of F4TCNQ doped solutions of Spiro-TAD in chlorobenzene for varying dopant concentrations (wt%, 0% (black), 1%(red), 2%(blue))

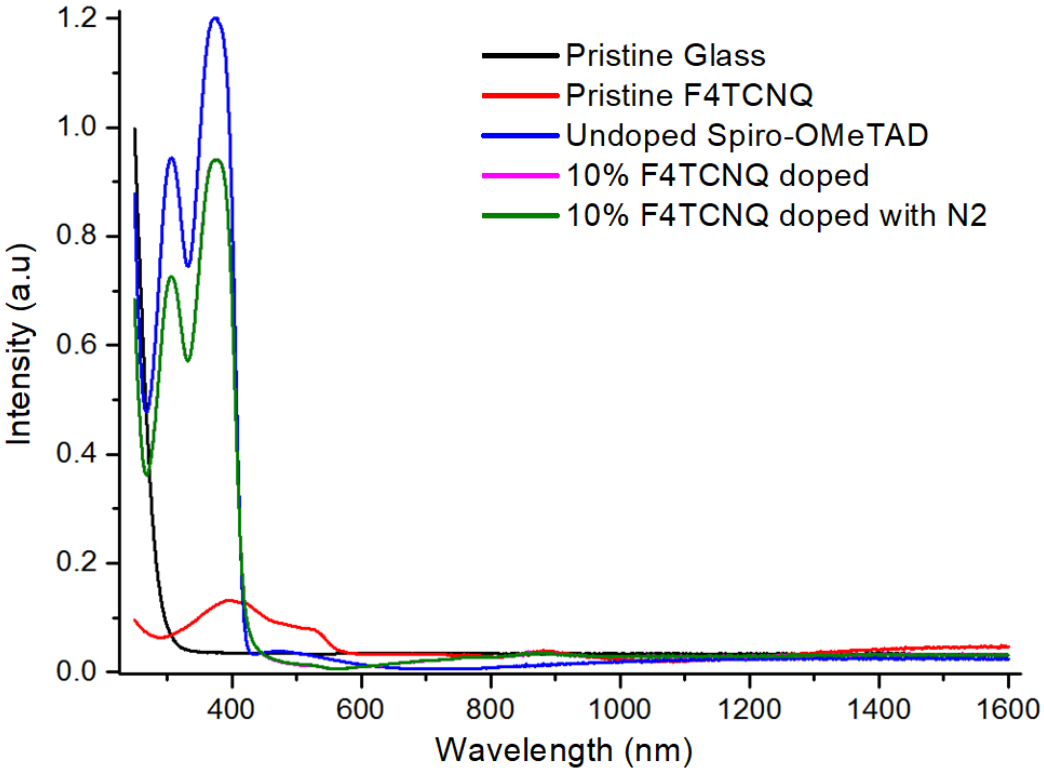

A 4 UV-Vis spectra of glass (black), F4TCNQ(red), Spiro-OMeTAD pristine (blue) and F4TCNQ doped solutions of Spiro-OMeTAD without (pink) and with nitrogen gas (green).

A.3 FTIR spectra

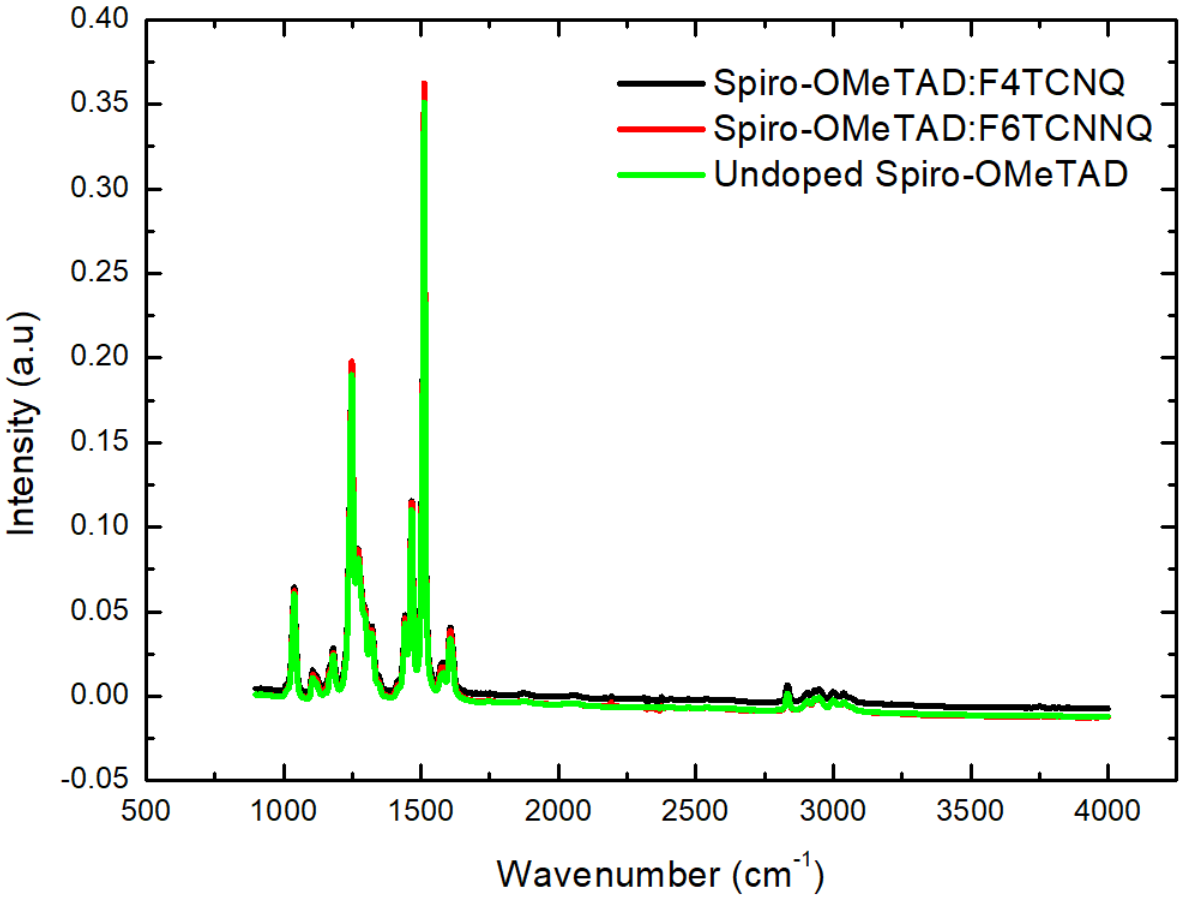

A 5 Complete FTIR spectra of Spiro-OMeTAD without (green) and with doping (black:F4TCNQ, red: F6TCNNQ)

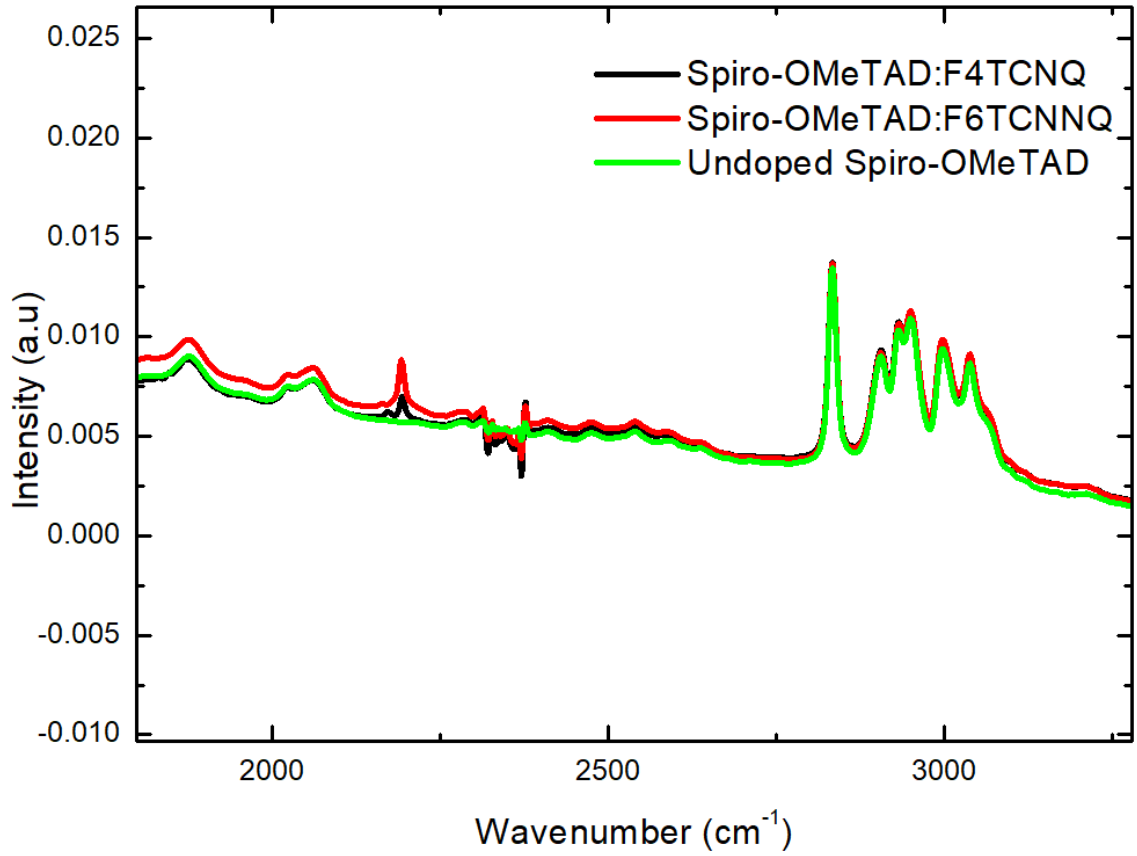

A 6 FTIR (zoomed in) spectra of Spiro-OMeTAD without (green) and with doping (black:F4TCNQ, red: F6TCNNQ)

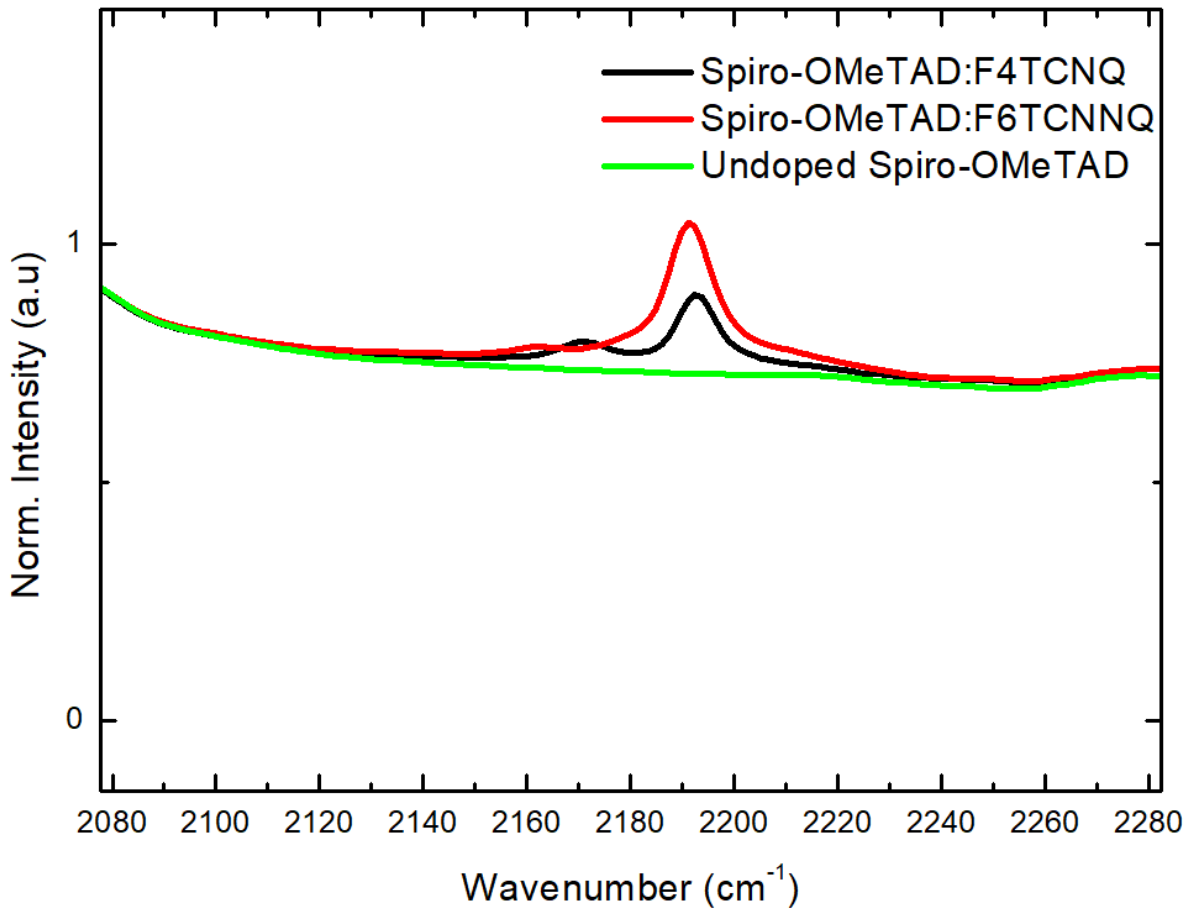

A 7 Normalized FTIR (zoomed in) spectra of Spiro-OMeTAD without (green) and with doping (black:F4TCNQ, red: F6TCNNQ)

The doped Spiro-OMeTAD shows no fingerprint of F6-TCNNQ and F4-TCNNQ, even for a 1:1 host:dopant mixture. It shows no evidence for intermolecular charge transfer in the FTIR spectra. The electronic structure of the Spiro-OMeTAD:F6-TCNNQ and Spiro-OMeTAD: F4-TCNNQ system could possibly be described in terms of the formation of hybrid orbitals in the charge transfer states. This however needs to be verified by further experimental investigation.

A.4 Effect of barrier on numerical simulation of J-V Characteristics

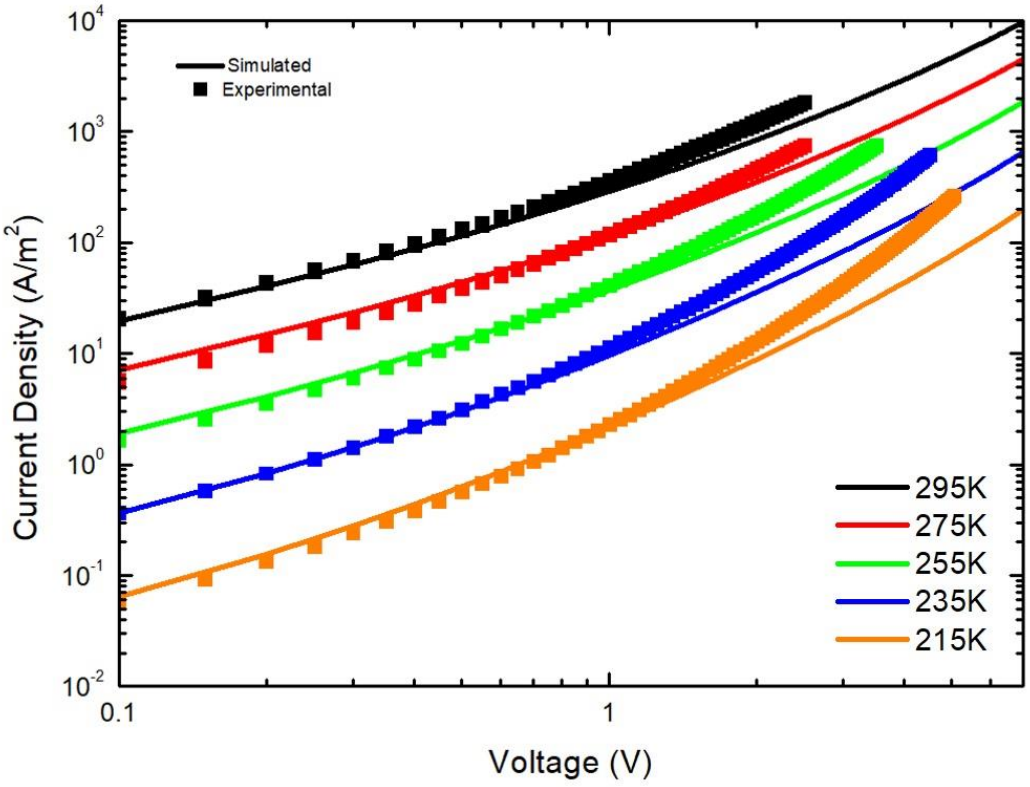

A 8 Temperature dependence of a 2% doped F6TCNNQ: α-NPD device. Dotted lines refer to experimental measurements. Solid lines refer to numerical simulations. A barrier of 0.1eV is additionally included in the numerical simulation.

We observe that inclusion of a barrier of 0.1 eV shows negligible change compared the numerical simulations without barrier (Figure 5-4 c))

Appendix B

List of publications:

1. M. Li*, **D. K. Mangalore***, J. Zhao, J. H. Carpenter, H. Yan, H. Ade, H. Yan, K. Müllen, P. W. M. Blom, W. Pisula, D. M. de Leeuw, K. Asadi, Integrated circuits based on conjugated polymer monolayer, Nat. Commun. 9, 451 (2018)
   *These authors contributed equally

2. I. Rörich, A-K. Schönbein, **D. K. Mangalore**, A. H. Ribeiro, C. Kasparek, C. Bauer, N. I. Crăciun, P. W. M. Blom, C. Ramanan, Temperature dependence of the photo- and electroluminescence of poly(p-phenylenevinylene) based polymers}, J. Mater. Chem. C 6, 10569 (2018)

3. **D. K. Mangalore**, P. W. M. Blom, G.-J. A. H. Wetzelaer, Hole-transport comparison between solution-processed and vacuum-deposited organic semiconductors, APL Mater. 7, 011105 (2019) - **Editor's pick**

4. **D. K. Mangalore**, P. W. M. Blom, G.-J. A. H. Wetzelaer, Study of charge transport in doped hole transport layers with the high electron affinity dopants, Under review